UiT The Arctic University of Norway

Department of Chemistry

Homogeneous Metal-Mediated Carboxylation with Carbon Dioxide

A computational study on Cs-, Cu- and Ni-mediated carboxylation reactions

Marc Ferry Obst

A dissertation for the degree of Philosophiae Doctor – June 2020

Abstract

CO_2 is a non-toxic, abundant and readily available gas, which has the potential to become an important carbon source in chemical synthesis. The clear advantage of CO_2 is its sustainability, in contrast to typical carbon sources such as oil, coal, or natural gas, which are in the process of depletion. However, the use of CO_2 also poses a big challenge as it features a high thermodynamic and kinetic stability. Therefore, the aim of this thesis is to help in overcoming the chemical inertness of CO_2 by computational investigation of CO_2-converting catalysts. Catalysts are generally an important tool in chemical synthesis, and their ability to decrease activation energies could help enabling a wider use of CO_2 as a carbon source. In this work we concentrated our enquiry on homogeneous catalysts, as they feature defined reactive species and large reactive surfaces. For the metal center, we concentrated on base transition metals, such as Cu or Ni, which are less understood and considerably less expensive than the more commonly used heavy transition metals. We were especially interested in C-C bond forming reactions with CO_2 as they constitute new reaction routes, giving access to chemicals such as carbonates or pharmaceuticals. By using computational chemistry and cooperating with experimental chemists, we where able to gain insight into CsF-, Cu- and Ni-mediated carboxylation reactions. The results of these investigations yielded several interesting findings: First, a reaction mechanism for Cs-mediated carboxylation of organoboranes was identified which was able to explain the observed substrate preference and predicts an organocaesium intermediate. Second, the reaction mechanism for Cu-IPr-catalyzed carboxylation of organoboranes was investigated showing the formation of an organocopper intermediate before the insertion of CO_2 and yielding different behaviours for the Cu-CO_2 interaction, depending on the electronic nature of the coordinating carbon atom. The calculation of IR spectra for Phen-Ni(I)-alkyl species helped identifying their thermally unstable carboxylation products and the calculation of the CO_2 insertion TSs support the conclusion of strong Ni-CO_2 interactions.

Contents

List of Papers

This thesis is based on the following scientific publications.

I A. Gevorgyan, **M. Obst**, Y. Guttormsen, K. H. Hopmann and A. Bayer,[1] "Caesium fluoride-mediated hydrocarboxylation of alkenes and allenes: scope and mechanistic insights", *Chem. Sci.*, **2019**, 10, 10072-10078, DOI: 10.1039/C9SC02467K

II M. Obst, A. Gevorgyan, A. Bayer, and K. H. Hopmann, "Mechanistic Insights into Copper-Catalyzed Carboxylations", *Organometallics*, **2020**, 39, 1545-1552, DOI: 10.1021/acs.organomet.9b00710

III R. Somerville, C. Odena, **M. Obst**, N. Hazari, K. H. Hopmann, and R. Martin,[2] "Ni(I)-Alkyl Complexes Bearing Phenanthroline Ligands: Experimental Evidence for CO_2 insertion at Ni(I) Centers" *J. Am. Chem. Soc.*, **2020**, accepted, DOI: 10.1021/jacs.0c04695

IV M. Obst, Lj. Pavlovic, and K. H. Hopmann,[3] "Carbon-carbon bonds with CO_2: Insights from computational studies" *J. Organomet. Chem*, **2018**, 864, 115-127, DOI:10.1016/j.jorganchem.2018.02.020

The following contributions were made to the papers. For **Paper I** and **III** my contributions were all computational results as well as the section on the computational methods and results for the manuscript draft. Similarly all computational results and the manuscript draft were contributed to **Paper II** by me. For the review **Paper IV** my contribution was the sections on the reactions utilizing Cu as catalyst.

---

[1]The first two authors contributed equally.
[2]Second and third author contributed equally.
[3]The first two authors contributed equally.

Acknowledgement

With my PhD and the work on this thesis coming to an end after countless spent work and CPU hours, I would like to thank all the people who helped me during this journey.

First and foremost, I want to thank Kathrin H. Hopmann. Amongst others things I am deeply grateful for the possibility to work and research in her group, the reliable support, the great degree of freedom for my work, and the helpful feedback without which the papers and this thesis could not have been possible in this form. In short, I am thankful for the excellent supervision during my PhD and the great working environment.

Furthermore, I would like to thank my co-supervisors Annette Bayer and Luca Frediani for supporting me during my PhD journey with their expertise and advises.

As I was part of Kathrin's and Annette's CHOCO group, I want to thank Anders M. Brakestad, Ashot Gevorgyan, Yngve Guttormsen, Ljiljana Pavlovic, Diego García López, and all other group members for their support. Especially, I want to express my gratitude to Ashot for his work, advise and the great and productive collaboration, as well as to Anders for his help with this thesis.

My work for this thesis was done in collaboration with external researchers and therefore I wish to thank Ruben Martin, Rosemarie Somerville, Nilay Hazari and Carlota Odena for their work and the successful cooperation.

I also want to express my gratitude towards the Tromsø Research Foundation, for financing my PhD position as well as to the Research Council of

Abbreviations

The following abbreviations have been used in this thesis:

9-BBN	9-Borabicyclo(3.3.1)nonane
9-F-9-BBN	9-Fluor-9-Borabicyclo(3.3.1)nonane
AFIR	Artificial Force-Induced Reaction
BJ	Becke-Johnson
CC	Coupled Cluster
DFT	Density Functional Theory
DLPNO	Domain-based Local Pair Natural Orbital
ECP	Effective Core Potential
ee	Enantiomeric Excess
GGA	Generalized Gradient Approximation
HF	Hartree-Fock
IPr	1,3-bis(2,6-diisopropylphenyl)imidazol-2-ylidene
IR	Infrared
IRC	Intrinsic Reaction Coordinate
KS	Kohn-Sham
LDA	Local-Density Approximation
LMO	Localized Molecular Orbital
MC	Monte Carlo
NHC	N-Heterocyclic Carbene
PAO	Projected Atomic Orbital
PCM	Polarizable Continuum Model
PES	Potential Energy Surface
Phen	Phenanthroline
PP	Pseudopotential

SCF	Self-Consistent Field
SP	Single Point
TS	Transition State
ZORA	Zeroth-Order Regular Approximation
ZPVE	Zero-Point Vibrational Energy

Notations and Conventions

The following naming conventions will be used for all mechanisms, substrates, intermediates and TSs in this thesis:

- All names are in bold for distinction.

- Mechanisms will be indicated via capitalized letters and are given in alphabetic order (**A**, **B**, etc.).

- Substrates will start with "sub" and be given a number in increasing order (**sub1**, **sub2**, etc.).

- Intermediates start with an "i" and the associated mechanism as subscript followed by the number (**i_A1**, **i_B3**, etc.).

- TSs start with "TS" followed by the two intermediates it connects in parenthesis (**TS(i_A1-i_A2)**)

- The reference states will be named **i0** and the products as **p0**.

In certain cases these names will be used together with longer names, if these alternative names help the understanding of the reader.

Chapter 1

Introduction

1.1   Use of CO$_2$ in Chemical Synthesis

Carbon dioxide (CO$_2$) is a colorless, odourless, non-flammable gas and the product of numerous natural and anthropogenic processes, such as burning of fossil fuel, production of concrete, fermentation, or respiration. Therefore, it is omnipresent but only as a trace gas as CO$_2$ is also constantly removed from the atmosphere.

Plants and algae are overwhelmingly responsible for this consumption as they utilize CO$_2$ as a carbon source during photosynthesis.[1,2] For this process, the CO$_2$ is captured from the atmosphere using the enzyme RuBisCo and together with water converted to C-3 species via the Calvin-cycle, shown in Fig 1.1.[3] This process is impelled by photon energy and constitutes the starting point for almost all organic molecules in nature.

Outside of nature, CO$_2$ has many uses such as inert gas, solvent, food additive or coolant.[5] Like in nature it is also utilized as a carbon source and
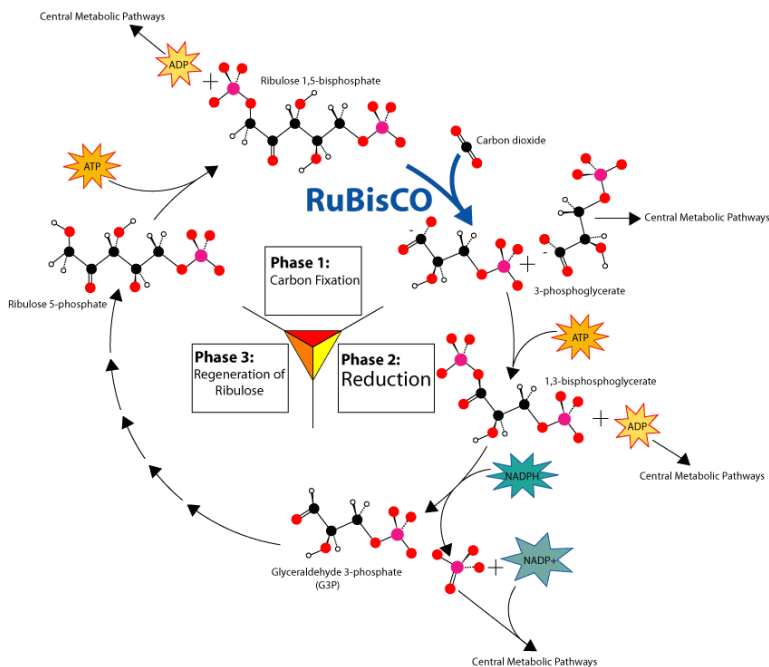
1

Figure 1.1: Calvin Cycle taken from [4].

typical chemical products partially formed from CO_2 are urea, carbonates, methanol or salicylic acid.[1,6,7] However, only around 0.1 % of the total CO_2 amount is converted in this way and the range of products is small when compared with the total amount of carbon-based chemicals.[8]

The reason for the limited use of CO_2 as a carbon source in industry is the relatively high inertness of CO_2, as it constitutes the most oxidized form of carbon and is kinetically inert as well as thermodynamically stable.[6,7] This means that when CO_2 is employed as a carbon source, either harsh reaction conditions (high pressures and temperatures), high-energy co-reactants, catalysts or a combination of those is necessary. Consequently the use of CO_2 is often less economically favourable than alternative carbon sources.

To overcome this problem of chemical inertness and to establish CO$_2$ as a competitive carbon source, new and better reaction protocols are necessary. Taking the use of CO$_2$ during photosynthesis as an example, it is evident that catalysts will be an integral part of solving the problem of inertness because they are capable of activating CO$_2$ and/or introducing selectivity.

Considering the problems of CO$_2$ as a carbon source, one might wonder why to invest into its use. The conventional carbon sources, crude oil, natural gas, and coal, are well established and many years of investigation and optimization of the synthetic routes means that competing against those will be difficult. However, the main disadvantage of these "classical" carbon sources is that they are finite and therefore ultimately will be depleted. This problem does not exist for CO$_2$ as all chemicals will eventually be converted back to CO$_2$ and would therefore be available again.[9] Furthermore, CO$_2$ is abundant and it is estimated that around 37.1 Gt of CO$_2$ are produced per year[10] as a result of anthropogenic activities, which is several times more than the approximately 300 Mt sufficient for a CO$_2$-based chemical industry.[11] Additionally to collecting it from exhaust gases, CO$_2$ is also part of the atmosphere, with 414 ppm (mole fraction),[12] making it practically everywhere available. Another advantage of CO$_2$ is that, in contrast to the use of biomass from plants, it does not require any farmable land and does therefore not compete with the production of food.[13]

One can generally differentiate two ways of utilizing CO$_2$ in chemical synthesis. The first is to reduce it with e.g. hydrogen to create simple products such as CO, formic acid, methanol or methane. These species can be utilized either as building blocks and/or solvents for the synthesis of larger molecules, or as fuels. The second is to incorporate CO$_2$ into other

molecules, via the formation of carbon-carbon (C-C) or carbon-heteroatom (C-X) bonds, resulting in carboxylic acids, carbonates or carbamates. Such chemicals are usable as starting materials, e.g. for polymers, or can constitute a final product.[6,7,14–16]

1.2   Focus of the Thesis

The focus of this thesis was the catalytic addition of CO_2 to other molecules specifically via carbon-carbon bond formation using homogeneous catalysts with base metal centres. Furthermore, the investigations were to be conducted via the usage of computational chemistry. The reasons for this focus were:

First, the insertion of CO_2 into molecules gives access to a number of valuable chemicals and pharmaceuticals, e.g. acetylsalicylic acid or butibufen. Producing such fine chemicals is more likely to justify using potentially expensive CO_2 insertion protocols and could thus be a starting point for the wider utilization of CO_2 in chemical synthesis.

Second, base (transition) metals, such as Fe, Co, Ni, or Cu, are considerably more abundant and less expensive than the typically employed heavier transition metals (Ru, Rh, Pt, etc.) and are also less understood. Because of these points base transition metal catalysts constitute an interesting subject for research, from a scientific and industrial standpoint.

Third, homogeneous catalysts feature large reactive surfaces and defined active species. The latter point makes the modelling of homogeneous reactions easier (compared to heterogeneous catalysts) and opens the possibility of fine-tuning the catalyst for selectivity, e.g. stereoselectivity and substrate

preference.

Fourth, the experimental investigation of reaction mechanisms can be difficult and time intensive because of the small size of molecules and the short time scale of chemical reactions. Using the methods of computational chemistry, which combine the principles of quantum mechanics with the ability of computers to find numerical solutions to complicated mathematical formulas, is a well-established way to gain insights into the elementary processes during a reaction. By combining computational and experimental results, one can gain a more comprehensive understanding of the important factors of chemical reactions.

1.3 Aims of the Thesis

This work was aimed at reactions that fixate CO_2 via C-C bond formation utilizing homogeneous base (transition) metals. The aims were threefold:

1. Investigation of possible reaction mechanisms and identification of the preferred pathways.

2. Investigation of the mode of CO_2 insertion and importance of metal-CO_2 interactions.

3. Testing of recent computational methods for the investigation of reaction mechanisms.

Chapter 2

Background

2.1 Catalysis

A catalyst is defined as any substance that accelerates a chemical reaction without being consumed in the process. This increase of the reaction rate is achieved because the catalyst gives access to alternative reaction mechanisms with lower activation energies, as it is schematically shown in Fig. 2.1. The lower activation energies mean that more molecules are capable of reacting in presence of a catalyst compared with the uncatalyzed system at the same temperature. During the reaction, the catalyst will usually form one or several intermediates with the substrate, but is regenerated at the end of the reaction. Therefore, each catalyst molecule can undergo several such reaction cycles and thus convert several substrate molecules, which means that often only small amounts of catalyst are necessary.[17]

It is difficult to overstate the importance of catalysts as they are part of numerous processes in nature and industry. In living organisms, catalysts
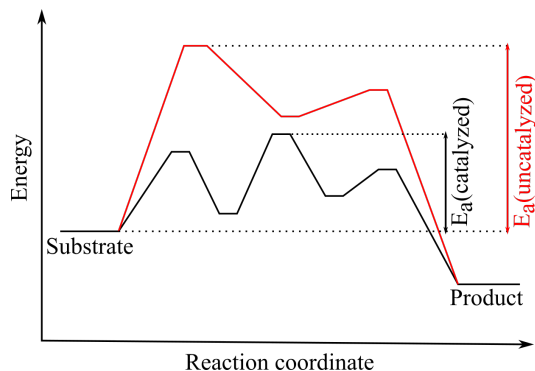
Figure 2.1: Schematical effect of a catalyst on the activation energy of a reaction.

can be found in the form of enzymes, which are highly selective, protein-based catalysts that are part of almost all metabolic processes in cells. For industrial usage, catalysts are equally important as there are hardly any chemicals which do not utilize catalysts during their synthesis.

Furthermore, some of these products are of enormous importance. The possibly most prominent example is ammonia, which is produced via the Haber-Bosch process utilizing an iron-based catalyst, and is the basis for the production of artificial fertilizer amongst many other uses.[18] Other examples for the use of catalysts in industry are the cracking of hydrocarbons,[19] the cleaning of exhaust gases[20,21] or the production of margarine,[22] indicating the wide range of applications for catalysts.

One general and important distinction is between homogeneous and heterogeneous catalysts, depending on if reactants and catalysts are in the same or different phases. This distinction is important as the two kinds of catalysts feature very distinctive properties. Heterogeneous catalysts feature a comparably easy separation of product and catalyst but lack well-defined active species and in some cases have problems with the reproducibility. These

factors make studying and modelling heterogeneous catalysts relatively challenging. Homogeneous catalysts in contrast have well-defined active species making their modelling less complicated and allowing systematic altering towards desired properties. Furthermore, homogeneous catalysts have a very large reactive surface as substrate and catalyst are in the same phase. However, being in the same phase also results in more difficulties of separating catalyst and product than in the case of heterogeneous catalysts.[17]

The focus in this thesis was homogeneous catalysis. This choice was made because of the straightforward modelling of the catalyst, and the potential to systematically alter the catalyst to provide the desired reactivity and selectivity.

2.2 Computational Models

Reactions can be studied by a number of experimental methods, such as measuring reaction rates, isotopic labelling or time-resolved spectroscopy. An additional approach is computational chemistry, whose methods are well suited to describe the atomic and molecular processes of a chemical reaction. For this purpose, the putative intermediates and transition states (TSs) of a reaction are optimized to obtain their associated energies. However, before these energies are calculated, the used models and assumptions of chemical reactions should be understood.

A central concept in the modelling of chemical reactions with computational chemistry is the Potential Energy Surface (PES). This is the energy of as system as a function of the coordinates of all its atoms. All local minima of this hyper surface are stable (ground-) states for a system and are

interpreted as intermediates, substrates or products. A chemical reaction is consequently a path along this surface from the minimum of the substrate to the minimum of the product. Additionally to the local minima, there are first-order saddle points found along these paths which are interpreted as TSs.

To reduce the complexity when describing these paths, a so-called reaction coordinate is defined which contains all changes along the reaction path. With this reaction coordinate the path on the PES can be simplified to one dimension and a chemical reaction can be described as a series of local minima (intermediates) and first-order saddle points (TSs) of the energy.

To relate the energies of these intermediates and TSs with experimentally observable reaction rates, the Eyring theory can be used:

$$k = \frac{\kappa k_{\mathrm{B}} T}{h} e^{-\frac{\Delta G^{\ddagger}}{RT}} \tag{2.1}$$

Where k is the reaction constant, κ is the transmission coefficient, k_{B} the Boltzmann constant, T the temperature, h the Planck constant, R the gas constant and $\Delta G^{\ddagger}$ the Gibbs energy of activation.

For this theory, the reaction is split into a number of elementary reaction steps, meaning the path from one local minimum to the next. It is now assumed that there is a dynamic equilibrium between molecules in each of these minima. For a molecule to react it has to overcome the (Gibbs) energy difference/barrier between its current minimum and the maximum (TS) separating the two minima. The Eyring equation (2.1) describes the rate constant of such an event, depending on the energy difference and temperature. With these rate constants it can be estimated if a certain

reaction mechanism can yield a measurable conversion of a substrate.

As will be discussed later, the energies obtained by quantum chemical calculations are typically only the electronic energies and the nuclei-nuclei repulsion. To obtained the needed Gibbs energies several contributions from other degrees of freedom are needed. These corrections are the thermal, vibrational and entropic energies based on the transitional, rotational, vibrational and electronic(usually neglected) motion.[23]

Without going into detail, the contributions from translation and rotation can be calculated by applying the ideal gas equation. For estimating the vibrational contribution the vibration modes of the molecules are needed. These can be calculated by assuming a harmonic potential between atoms and give access to the Zero-Point Vibrational Energy (ZPVE) and to calculate the vibrational energy by applying the Boltzmann statistic to the vibration states.[23]

$$p_i = \frac{e^{\frac{\epsilon_i}{k_B T}}}{\sum_{j=1}^{M} \frac{\epsilon_j}{k_B T}} \tag{2.2}$$

(2.2) gives the occupation number p_i for a vibrational state and thus the energetic contribution at a given temperature can be calculated.

With these models and assumptions the putative intermediates and TSs for a reaction mechanism can be optimized to obtain the associated Gibbs energies and estimate the reaction rates for each reaction step. Alternatively, it is often sufficiently accurate to only calculate the rate constant for a hypothetical reaction from the energetically lowest intermediate to the highest TS (rate-limiting barrier). The reaction rates can be used to make statements about the likelihood of a reaction mechanism at a given temperature.

The methods and approximations used to calculate the necessary energies will be the topic of the next section.

2.3 Computational Methods

2.3.1 Basics

Schrödinger Equation

It is known, that the motion of particles on an atomic size scale cannot be described by employing the principles of classical mechanics. Instead, a quantum mechanical description is necessary. The Schrödinger equation:

$$\hat{H} \left| \Psi \right\rangle = \mathrm{i}\hbar \frac{\partial}{\partial t} \left| \Psi \right\rangle \tag{2.3}$$

is capable of describing the movement and evolution in time of a quantum mechanical system (atoms and molecules for our purposes).

The wave function $\left| \Psi \right\rangle$ of any system must solve (2.3) to be valid and from this wave function all properties of the system can be obtained.[24] Eq. (2.3) is a differential eigenvalue equation for which the Hamiltonian $\hat{H}$ acts as the eigenoperator. $\hat{H}$ describes the energy of a system and can be

written as (in atomic units without an external field):

$$\hat{H} = -\underbrace{\sum_{a=1}^{N_\text{n}} \frac{1}{2m_a} \nabla_a^2}_{\hat{T}_\text{n}} - \underbrace{\sum_{i=1}^{N_\text{e}} \frac{1}{2} \nabla_i^2}_{\hat{T}_\text{e}} + \underbrace{\sum_{a=1}^{N_\text{n}} \sum_{b>a}^{N_\text{n}} \frac{Z_a Z_b}{|\vec{R}_a - \vec{R}_b|}}_{\hat{V}_\text{nn}}$$

$$+ \underbrace{\sum_{i=1}^{N_\text{e}} \sum_{j>i}^{N_\text{e}} \frac{1}{|\vec{r}_i - \vec{r}_j|}}_{\hat{V}_\text{ee}} - \underbrace{\sum_{a=1}^{N_\text{n}} \sum_{i=1}^{N_\text{e}} \frac{Z_a}{|\vec{R}_a - \vec{r}_i|}}_{\hat{V}_\text{ne}} \quad . \tag{2.4}$$

Where $\vec{R}$ and $\vec{r}$ are nuclei and electron coordinates, N the number of nuclei or electrons, Z the nuclei charge, m the nuclei mass, and ∇ the nabla operator. The Hamiltonian can be separated into the kinetic $\hat{T}$ and potential energy operator $\hat{V}$ for the electrons (indicated by e) and nuclei (indicated by n).[24]

As one is usually not interested in the development of a wave function over time one can assume a stationary solution to separate the time-dependency via $|\Psi(\vec{r}, \vec{p}, t)\rangle = |\Psi'(\vec{r}, \vec{p})\rangle e^{-\text{i}Et}$.[24] Using this on (2.3) one obtains the time-independent Schrödinger equation:

$$\hat{H} |\Psi'\rangle = E |\Psi'\rangle \tag{2.5}$$

However, except for the simplest systems (hydrogen and its analogues) (2.5) cannot be solved analytically and a number of approximations are necessary to simplify it.

The two possibly most important approximations are the Born-Oppenheimer and adiabatic approximation. In the Born-Oppenheimer approximation the movement of nuclei and electrons is separated, treating nuclei positions as parameters instead of variables for the electrons' motion

and thus having to only solve the electronic wave function.[24]

The adiabatic approximation limits the wave function to one electronic state and approximates the cross-interaction term between different electronic states as zero. With these approximations, one arrives at the electronic Schrödinger equation:

$$(\hat{T}_\mathrm{e} + \hat{V}_\mathrm{ee} + \hat{T}_\mathrm{ne}) \, |\Psi'_\mathrm{e}\rangle = E_\mathrm{e} \, |\Psi'_\mathrm{e}\rangle \tag{2.6}$$

$$\hat{H}_\mathrm{e} \, |\Psi'_\mathrm{e}\rangle = E_\mathrm{e} \, |\Psi'_\mathrm{e}\rangle$$

Eq. (2.6) describes the movement of the electrons in a set of nuclei positions. By solving (2.6) for a given system the electronic wave function $|\Psi'_\mathrm{e}\rangle$ is obtained from which the electronic energy E_e and electronic properties are calculated. Furthermore, by using the gradients of the electronic wave function the arrangement of nuclei can be optimized to yield molecular geometries with the lowest energies (ground state geometries).

The electronic Schrödinger equation (2.6) is the basis for most quantum chemical calculations and unless stated otherwise all mentions of the wave function $|\Psi\rangle$ or the Schrödinger equation will refer to the electronic wave function $|\Psi'_\mathrm{e}\rangle$ or the electronic Schrödinger equation (2.6).

Hartree-Fock Method

The challenge in solving eq. (2.6) is the $\hat{V}_\mathrm{ee}$ term describing electron-electron interaction. The reason is that for any system with more than one electron this results in a many-body system, which can only be solved approximately.

One important method to approximate the solution is Hartree-Fock (HF)

theory. HF requires two assumptions: *i)* that the wave function can be described by a single Slater-determinant, in which electrons and orbitals are arranged in the columns and rows to fulfill the antisymmetry conditions of the wave function, and *ii)* that each electron moves in the mean-field of all other electrons.[24]

Under these assumptions the Schrödinger equation (2.6) can be replaced by the HF equation:[24]

$$\hat{F}_j \left| \psi_j \right\rangle = \epsilon_j \left| \psi_j \right\rangle \tag{2.7}$$

where $\left| \psi_j \right\rangle$ is the orbital of electron j, ϵ_j energy of electron j and $\hat{F}_j$ the Fock operator for electron j. The Fock operator $\hat{F}_j$ is defined as:

$$\hat{F}_j = \hat{h}_j + \sum_j^{N_e} (\hat{J}_j + \hat{K}_j) \tag{2.8}$$

where $\hat{h}$ is the one-electron, $\hat{J}$ the Coulomb, and $\hat{K}$ the exchange operator. The latter two are known as the two-electron operators and describe the electron's interaction in the mean-field of all other electrons.

Accordingly, eq. (2.7) allows to calculate the energy of every electron and the variational principle can be applied to minimize the energy.

$$\frac{\langle \Psi_0 | \hat{H} | \Psi_0 \rangle}{\langle \Psi_0 | \Psi_0 \rangle} = E_0 \leq E = \frac{\langle \tilde{\Psi} | \hat{H} | \tilde{\Psi} \rangle}{\langle \tilde{\Psi} | \tilde{\Psi} \rangle} \tag{2.9}$$

The variational principle (2.9) states that the energy E_0 of the ground state wave function $\left| \Psi_0 \right\rangle$ is always lower than the energy E of any other approximated wave function $\left| \tilde{\Psi} \right\rangle$. By minimizing the energy ϵ and the orbital $\left| \psi \right\rangle$ for each electron iteratively until convergence, the ground state wave function $\left| \Psi_0 \right\rangle$ can be approximated. Because of this iterative approach the method

is often referred to as Self-Consistent Field (SCF).[24]

By using the HF method, the majority of the electronic energy can be described, but the results are not accurate enough for applications such as predicting reaction barriers. The reason for this is the mean-field approach to the electron-electron interaction which neglects parts of the electron-electron correlation. To solve this problem a number of methods, e.g. Density Functional Theory (DFT) or Coupled Cluster (CC), have been developed to describe the missing electron-electron correlation and obtain more accurate energies. However, the HF method is still useful because the HF wave function is often used as reference for high-level **ab initio** methods.

Basis Sets

As it is generally not known how the wave function of as system looks it has to be approximated. This is usually done by expanding the one-electron orbital $|\psi\rangle$ in a basis set. These basis sets consist of basis functions $|\chi\rangle$, which are comprised of a radial part, often based on Slater or Gaussian functions, and an angular part, based on the analytical solution of the hydrogen atoms.[24] In case of Gaussian-type basis functions they generally have the form of:

$$|\chi^{\text{GTO}}_{\zeta,n,l,m}\rangle = A \, Y_{l,m}(\theta,\phi) \, r^{2n-2-l} \, e^{-\zeta r^2} \tag{2.10}$$

with the normalisation coefficient A, the angular part Y, the quantum numbers l, n, and m.

Gaussian-type basis functions are most common because they and their products have easy integrals, resulting in a speed-up of calculations, while

Slater-type basis functions are more accurate for the same number of functions but feature much slower integral evaluation making them less viable. Consequently, the basis sets used in this work, such as the Pople and Ahlrichs basis sets, are of the Gaussian-type.

From the basis functions atomic orbitals $|\nu\rangle$ are constructed via linear combination.

$$|\nu\rangle = \sum_j c_j |\chi_j\rangle \tag{2.11}$$

In return, the molecular orbitals $|\psi\rangle$ are obtained by linear combination of the atomic orbitals $|\nu\rangle$.

The accuracy of a basis set is better the more basis functions are used per electron and as the chemical properties are overwhelmingly defined by the outermost electrons many basis sets add more basis functions to these electrons (split-valence basis sets). Generally one can differentiate between double-ζ, triple-ζ, quadruple-ζ, etc. basis sets depending on the number of basis functions per valence electron.

Often it is useful to add diffuse functions or functions of higher quantum numbers to a basis set as this can improve the description of loosely bound electrons or polar bonds. These basis sets are called augmented or polarizable and this is indicated by the use of "+" or "aug-" for augmented basis sets and "*" or "P" for polarizable basis sets.

2.3.2   Density Functional Theory

DFT Ansatz

One of the most widely used approaches to calculate the electron-electron correlation missing in the HF method is Density Functional Theory. The original ansatz of DFT is to not utilize the wave function of a system but the electron density ρ. The significant advantage of this approach is the reduction of the degrees of freedom. While the wave function is a function of $3N_e$ variables the electron density is only dependent on three.

However, while the connection between wave function and energy is well known via (2.6) the connection between electron density ρ and energy E is not. This connection was made by the first Hohenberg-Kohn theorem that proves an explicit relation between density and energy of an electronic state.[25]

$$E = E[\rho] \tag{2.12}$$

Furthermore, the second Hohenberg-Kohn theorem states that the electron density with the lowest energy E_0 belongs to the ground state density ρ_0.[25]

$$E[\rho] > E_0 = E[\rho_0] \tag{2.13}$$

With these two theorems in place, the variational principle (2.9) can be used to optimize a guessed electron density and obtain the energy and electron density of the ground state.

The energy functional E can be separated into three components:

$$E[\rho] = E_{\text{kin}}[\rho] + E_{\text{ee}}[\rho] + E_{\text{ne}}[\rho] \tag{2.14}$$

where E_{kin} is the kinetic energy, E_{ee} the electron-electron interaction and E_{ne} the nuclei-electron interaction.

The calculation of the nuclei-electron interaction E_{ne} is straightforward as the Coulomb law can be used and the resulting equation is very similar to $\hat{V}_{\text{ne}}$ in (2.4).

$$E_{\text{ne}}[\rho] = \sum_{a=1}^{N_{\text{n}}} \int \frac{\rho \, Z_a}{|\vec{r} - \vec{R}_a|} \, \mathrm{d}\vec{r} \tag{2.15}$$

Kohn-Sham Orbitals

The connection between electron density and the kinetic energy E_{kin} is far more complicated, as it is only known exactly for a free electron gas. However, except for valence electrons in metals this treatment leads to large errors as electrons in molecules and atoms behave very differently. To solve this problem of inaccurate kinetic energies Kohn and Sham proposed to reintroduce orbitals into the DFT formalism. These so-called Kohn-Sham (KS) orbitals $|\psi^{\text{KS}}\rangle$ are defined to not interact with each other and to have the same electron density as interacting orbitals.[26]

$$\rho = \sum_{i}^{N_{\text{e}}} \rho_i^{\text{KS}} = \sum_{i}^{N_{\text{e}}} |\,|\psi_i^{\text{KS}}\rangle\,|^2 \tag{2.16}$$

This ansatz increases the number or degrees of freedom to N_{e} again, but allows to calculate the kinetic energies of the electrons as:

$$E_{\text{kin}}[\rho] = \sum_{i=1}^{N_{\text{e}}} \langle \psi_i^{\text{KS}} | \hat{T}_{\text{e}} | \psi_i^{\text{KS}} \rangle \tag{2.17}$$

Electron-Electron Interaction

The second term $E_{ee}[\rho]$ in (2.14) describes the electron-electron interaction
and can be further separated into three terms: the Coulomb repulsion $J[\rho]$,
the electron-electron correlation energy $E_C[\rho]$ and the electron-electron ex-
change energy $E_X[\rho]$. The Coulomb repulsion $J[\rho]$ can be calculated ana-
logues to $E_{ne}[\rho]$ in (2.15) using the Coloumb equation.

$$J[\rho] = \frac{1}{2} \iint \frac{\rho(\vec{r})\,\rho(\vec{r'})}{|\vec{r} - \vec{r'}|} \, \mathrm{d}\vec{r}\mathrm{d}\vec{r'} \tag{2.18}$$

For the electron-electron correlation $E_C[\rho]$ and electron-electron ex-
change $E_X[\rho]$ no equation, such as (2.18) is known. Instead these terms
have to be parametrized, by employing either high quality *ab initio* calcula-
tions or experimental results.

XC Functionals

The functionals parametrised for this purpose are called DFT exchange-
correlation (XC) functionals. They usually also correct the error of the
kinetic energy and can be divided into different groups, depending on the
variables used to calculated the exchange-correlation energy $E_{XC}[\rho]$. These
groups are:

- Local-Density Approximation (LDA) functionals. These functionals
  are only a function of the local electron density ρ.

- Generalized Gradient Approximation (GGA) functionals, for which
  E_{XC} is dependent on the density ρ and its gradient $\nabla\rho$ making them
  slightly slower but more accurate than LDA functinals.

- Meta-GGA functionals, which include the second derivatives of the electrons density $\nabla^2 \rho$ into the calculation of the energy.

- Hybrid GGA functionals that mix density-based exchange with Hartree-Fock-based exchange. These functionals are considerably slower than LDA or GGA functionals due to the calculation of the HF exchange integrals.

- Double-hybrid GGA, the most accurate and most expensive functionals mixing HF exchange and PT2 (2nd order perturbation theory) into the energy calculation.

Going down the list above, accuracy and cost are generally increasing (often referred to as Jacob's Ladder of DFT functionals). For applications, such as geometry optimizations or calculation of vibrational modes, pure functionals (LDA, GGA and Meta-GGA) are usually sufficiently accurate. DFT functionals with HF exchange are usually better for electronic properties such as excitation energies or polarizabilities than those functionals without but considerably slower.

There are two approaches to the development of DFT functionals, universality or accuracy for a certain kind of system/property, and to find a suitable function, it is recommendable to either compare results with experiment or to consult/perform benchmark studies.

A weakness of many DFT functionals is their lack of long-range interactions, which can lead to qualitatively false results for systems were long-range interactions play a major role. To correct this weakness dispersion corrections were invented.[24] A widely used one was developed by Grimme and co-workers[27] and adds a dispersion energy as a function of the nu-

clei positions, resulting in a fast and easy dispersion correction for many functionals. Alternatively, a number of functionals have been developed to describe long-range interactions natively.

Despite or because of the large number of functionals, DFT is the work horse of electronic structure methods. The computational costs of DFT are similar to HF but results are qualitatively better. It is a robust and widely used method to obtain chemical accuracy for most systems. However, as the quality is dependent on the choice of functional and kind of system it is not suited as a "gold standard method". For this more accurate *ab initio* methods, like Coupled Cluster, are used.

2.3.3   Coupled Cluster

Coupled Cluster Theory

As mentioned earlier, HF only takes the averaged interaction between electrons into account and can therefore describe 99 % of the total energy. To recover the remaining 1 %, the precise electron correlation energy is needed. The starting point for the inclusion of the electron correlation is switching from a single-determinant $|\Psi\rangle$ wave function to a multi-determinant wave function $|\Phi\rangle$. The determinants are obtained as excited states of a reference (usually HF) wave function $|\Psi^0\rangle$.[24]

Coupled Cluster theory is a widely used *ab initio* method that acquires these excited determinants by action of the excitation operator $\hat{T}$.

$$\hat{T} = \hat{T}_1 + \hat{T}_2 + \hat{T}_3 + \cdots + \hat{T}_{N_\mathrm{e}} \tag{2.19}$$

T_a is generating the ath excited determinant and the CC wave function $|\Phi_{\text{CC}}\rangle$ is defined via:

$$|\Phi_{\text{CC}}\rangle = e^{\hat{T}} |\Psi_{\text{HF}}\rangle \qquad (2.20)$$

$$\text{with:} \quad e^{\hat{T}} = \sum_{i=0}^{\infty} \frac{1}{i!} \hat{T}_i \qquad (2.21)$$

Combining (2.19) with (2.21) and ordering via the order of excitations one obtains:

$$e^{\hat{T}} = 1 + \hat{T}_1 + (\hat{T}_2 + \frac{1}{2}\hat{T}_1^2) + (\hat{T}_3 + \hat{T}_2\hat{T}_1 + \frac{1}{6}\hat{T}_1^3) + \dots \qquad (2.22)$$

Accordingly, $|\Phi_{\text{CC}}\rangle$ is obtained as a sum of excitation operators and their products acting on the reference wave function $|\Psi^0\rangle$.

As a variational approach (2.9) is not feasible for most systems, the CC equation is solved via projection on the reference wave function by multiplication from the left with $\langle\Psi_0|$:

$$E_{\text{CC}} \langle\Psi_0|e^{\hat{T}}|\Psi_0\rangle = \langle\Psi_0|\hat{H}|e^{\hat{T}}\Psi_0\rangle \qquad (2.23)$$

$$E_{\text{CC}} = E_0 + \langle\Psi_0|\hat{H}|\hat{T}_1\Psi_0\rangle + \langle\Psi_0|\hat{H}|\hat{T}_2\Psi_0\rangle +$$
$$\frac{1}{2} \langle\Psi_0|\hat{H}|\hat{T}_1^2\Psi_0\rangle + \dots \qquad (2.24)$$

Like in Configuration Interaction the full CC equation (2.24) can practically only be solved for very small systems (like the H_2O molecule) as the number of non-zero contributions grows exponentially. Therefore, the number of excitations in (2.19) has to be truncated to keep the number of contributions at a manageable level. This is usually indicated by adding

the included excitations after the method name, e.g. CCSD for single and double excitations. As the contributions become increasingly smaller for higher excitations, a CCSDT approach is in most cases sufficiently accurate. Additionally, excitations can be included in a perturbative manner on the CC calculation, which is indicated by writing the perturbatively treated excitations in parenthesis, e.g. CCSD(T).[24]

DLPNO-CC

Despite the use of truncation and perturbation theory, CC remains an expensive method with scaling factors as high as N^6 (CCSD) or N^7 (CCSD(T)). This results in a rather hard limit for the maximum system size and there is consequently a great interest in improving the scaling of CC methods.

A solution to this is the use of localized electron correlation methods as pioneered by Pulay and Sæbø[28,29]. It is know that distant correlation pairs contribute considerably less than spatially close correlation pairs and it is therefore desirable to either calculate distant pairs at a lower level of theory or not at all.

The commonly used canonical orbitals are not suited for the calculation of correlation energies as they are strongly delocalized, which results in a steep increase in the number of contributions with the number of electrons. To take advantage of the localized nature of correlation one can use localized orbitals.

One method using localized orbitals for calculating electron correlation is Domain-based Local Pair Natural Orbitals-CC (DLPNO-CC). DLPNO-CC was developed by Neese, Hansen, Sandhoefer and Riplinger[30,31] as they

redesigned their earlier LPNO-CC (Local Pair Natural Orbital CC) method and is based on combining Paired Natural Orbitals (PNOs) and Projected Atomic Orbitals (PAOs).

PNOs are highly compact and fast converging orbitals pioneered by Meyer[32,33], Ahlrichs[34], and Taylor[35] which consist of approximated natural orbitals and are different for each electron pair. The PAOs are obtained by expansion of the PNOs and span the virtual space, but based in their definition remain local. This allows to assign a correlation subspace/domain of PAOs to each occupied orbital and several of such domains are united to describe higher excitations. The domains are defined based on spatial proximity, which results in an near-linear scaling CC method which recovers approximatly 99.9 % of the electron correlation.[30]

DLPNO-CC (specifically DLPNO-CCSD(T)) was used in this thesis as a means to obtain accurate electronic energies (approx. CCSD(T) level). Calculating electronic energies with "normal" CCSD(T) would have been difficult considering the size of the investigated systems (up to 400 electrons) and DLPNO offered the possibility of, only slightly less accurate, CC-based energies. A downside of DLPNO-CC is that at the time of writing this thesis, gradients were not available in the employed software (ORCA 4.2.0[36,37]) and only SP calculations were possible.

2.3.4   Relativistic Effects

Dirac Equation

The Schrödinger equation becomes increasingly inaccurate for heavier atoms. This is a result of increasing core charges which leads to such high kinetic

energies of core electrons that the effects of relativity can no longer be neglected. Some of the important relativistic effects are contraction of the *s* orbital, expansion of the *d* and *f* orbitals and spin-orbit coupling.[24]

Special relativity requires any formula to be invariant under Lorentz transformation and that spatial and time coordinates are treated equally. A successful approach to a quantum mechanical equation including relativistic effects is the Dirac equation. For a free electron the Dirac equation is (in atomic units):

$$[c\,\alpha \cdot \hat{p} + \beta c^2]\,|\Psi^{\mathrm{D}}\rangle = \mathbb{i}\frac{\partial}{\partial t}\,|\Psi^{\mathrm{D}}\rangle \tag{2.25}$$

where α and β are the Dirac matrices, c the speed of light, $\hat{p}$ the kinetic energy operator, and $|\Psi^{\mathrm{D}}\rangle$ the so-called Dirac spinor, a wave function with 4-components in contrast to the Schrödinger 1-component wave function.[24]

Eq. (2.25) yields two sets of solutions, the electronic and positronic energy states, separated energetically by $\approx 2c^2$. Commonly the energies are shifted by c^2 (the resting energy of an electron in atomic units) which is done by replacing β with β' . By doing this the obtained energies are similar to non-relativistic energies.

Analogue to (2.5) the Dirac equation (2.25) can be written in a time-independent form for an electron in an electric field $\boldsymbol{V}$

$$[c\alpha \cdot \hat{p} + \beta'c^2 + V]\,|\Psi^{\mathrm{D}}\rangle = E\,|\Psi^{\mathrm{D}}\rangle \tag{2.26}$$

Solving (2.26) for a system is not more complicated than solving the time-independent Schrödinger equation (2.5) but far more time intensive. However, $|\Psi^{\mathrm{D}}\rangle$ contains large $|\Psi^{\mathrm{L}}\rangle$ and small $|\Psi^{\mathrm{S}}\rangle$ components. Both are 2-component wave functions but the small components $|\Psi^{\mathrm{S}}\rangle$ usually account

for only a minor portion of the wave function and can thus be neglected.

$$|\Psi^{\mathrm{D}}\rangle = \begin{pmatrix} |\Psi^{\mathrm{L}}\rangle \\ |\Psi^{\mathrm{S}}\rangle \end{pmatrix} \tag{2.27}$$

Therefore, it is of interest to only obtain the large components $|\Psi^{\mathrm{L}}\rangle$ to recover most of the relativistic effects without the need of calculating the small components $|\Psi^{\mathrm{S}}\rangle$.

One method to solve the 2-component instead of the 4-component wave function is the Zeroth-Order Regular Approximation (ZORA).[38,39] For this purpose (2.26) can be written as:

$$c(\hat{\sigma} \cdot \hat{p}) |\Psi^{\mathrm{S}}\rangle + V |\Psi^{\mathrm{L}}\rangle = E |\Psi^{\mathrm{L}}\rangle \tag{2.28}$$

$$c(\hat{\sigma} \cdot \hat{p}) |\Psi^{\mathrm{L}}\rangle + (V - c^2) |\Psi^{\mathrm{S}}\rangle = E |\Psi^{\mathrm{S}}\rangle \tag{2.29}$$

where $\hat{\sigma}$ is the spin operator. Setting (2.28) into (2.29) one obtains:

$$\left[\frac{1}{2}(\hat{\sigma} \cdot \hat{p}) K (\hat{\sigma} \cdot \hat{p}) + V - E \right] |\Psi^{\mathrm{L}}\rangle = 0 \tag{2.30}$$

$$\text{with :} \quad K = \left(1 + \frac{E - V}{2c^2} \right)^{-1}$$

Eq. (2.30) is difficult to solve as K is dependent on the energy E. This can be solved approximately by expanding K in the power of $\frac{E}{2c^2 - V}$ and only using the zeroth order of this approximation. This is referred to as the ZORA method and yields:

$$\left[(\hat{\sigma} \cdot \hat{p}) \frac{c^2}{2c^2 - V} (\hat{\sigma} \cdot \hat{p}) + V \right] |\Psi^{\mathrm{L}}_{\mathrm{ZORA}}\rangle = E |\Psi^{\mathrm{L}}_{\mathrm{ZORA}}\rangle \tag{2.31}$$

With the expression (2.31) the scalar relativistic effects and the spin-orbit coupling can be introduced without the necessity to solve the 4-component Dirac equation (2.26).

Effective Core Potential

Another method to include relativistic effects is the use of Effective Core Potentials (ECPs) or Pseudopotentials (PPs). As the name suggests these are potentials replacing core electrons of atoms and are usually fitted to results of fully relativistic calculations or physical properties of heavy elements.

This approximation is justified as core electrons are virtually unaffected by the chemical surrounding for heavy atoms, and it has two advantages: First, it can introduce relativistic effects into non-relativistic calculations without solving the Dirac (2.25) or ZORA equation (2.31). Second, replacing electrons with potentials reduces the number of orbitals and results in a speed-up of calculations.

2.3.5 AFIR

Ansatz

A problem usually encountered when investigating reaction mechanisms is the large number of potentially important intermediates and TSs. This results in a large number of necessary calculations, especially for TSs as they require more accurate geometry guesses than ground state geometries. It is therefore of interest to automatize the process of identifying TSs (and to a lesser degree intermediates).

One method able to help with this task is AFIR (Artificial Force-Induced Reaction).[40,41] This method is part of the GRRM software[42] and can be used to automate the TS search.

The AFIR method is based on applying and stepwise increasing an artificial linear potential to approximated TS geometries. To use AFIR the reacting atoms (or atom groups) need to be defined and a linear potential is applied between these two on top of the PES. This potential can be attractive or repulsive depending on the reaction. The geometry is optimized with the modified PES and upon convergence the potential is increased. This cycle is repeated until either the artificial potential reaches a maximum predefined height or the potential "pushes" the structure above an approximated TS geometry. If successful, an approximated TS geometry is obtained from the AFIR path which can be used as guess for identifying the TS.

MC-AFIR

The AFIR method can be combined with the Monte Carlo method to yield MC-AFIR.[42,43] In this method several fragments are defined and will be placed randomly at the start of an AFIR run. This is useful when a reaction has different possible attack angles and with a high number of runs it is likely to obtain all possible TSs. In this thesis this method was used to control if TSs were overlooked by the "manual" TS search and if the method can reproduce the ones identified.

2.3.6   Solvation Effects

Many chemical reactions take place in some kind of liquid medium and the interaction of the medium with the solvated molecules can have a significant effect on their reactivity. It is therefore important to include these solvation effects into calculations to obtain useful results.

Explicit Solvation

The most straight forward approach is to explicitly include solvent molecules into the calculations. The advantages of this explicit solvation is that the solvent-solute interaction is accurately described (within the limit of the used method). The disadvantages, however, are the high computational costs and the need of extensive conformational sampling to obtain an average of the solvent-solute interaction, which further increases the computational costs. These computational costs can somewhat be reduced by combining different levels of theory for solvent and solute, resulting in the ONIOM or QM/MM method.[24]

Polarizable Continuum Model

An alternative and more commonly used approach to model solvation effects is implicit solvation such as Polarizable Continuum Model (PCM).[44,45] These models treat the solvent as a uniform medium interacting with the solute purely via polarization effects.

To apply an implicit solvent the molecule is placed in a cavity. The shape of this cavity can be defined by Van-der-Waals radii, solvent accessible, or solvent exclusive surface and can have influence on the results. The

solvation effect is obtained via the molecule and the polarizable continuum alternatingly polarizing each other until convergence is achieved.

This approach is fast and usually gives sufficiently good accuracy. Larger errors occur when solvent and solute have interactions not based on polarization such as hydrogen bonds, ligand-metal interactions, or π-π interactions. This problem can somewhat be circumvented by using explicit solvent molecules at positions where such interactions are to be expected and describing all other solvent molecules with an implicit solvation model. As implicit solvation models are parametrized to account for first and second solvation shell effects one should not employ too many of such explicit solvent molecules.

Chapter 3

Results and Discussion

3.1 Caesium Fluoride-Mediated Hydrocarboxylation of Alkenes and Allenes: Scope and Mechanistic Insights (Paper I)

Introduction

In 2017, Skrydstrup, Nielsen and co-workers published a protocol capable of converting alkenes and alkynes into carboxylic acids with CO_2 and a Cu(I)-NHC (*N*-Heterocyclic Carbene)-based catalyst.[46] While investigating this system in our group, we discovered that certain substrates (*trans*-stilbenes, β-substituted styrenes, and allenes) could be carboxylated without the Cu(I)-NHC catalyst. Instead, the presence of CsF, a reaction additive, alone was sufficient to facilitate the carboxylation reaction. We developed a reaction protocol from this finding which is shown in Fig. 3.1, and consisted of a hydroboration with (9-BBN)$_2$ (9-BBN = 9-Borabicyclo(3.3.1)nonane)

and an *in situ* carboxylation with CO_2 and CsF.
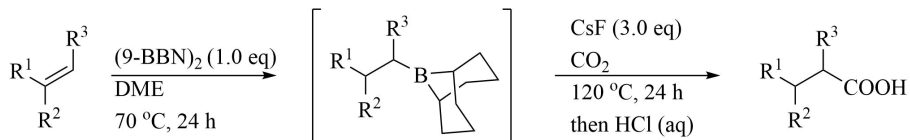
Figure 3.1: Reaction protocol for the CsF-mediated carboxylation of stilbenes and styrenes with CO_2 (**Paper I**).

In this project we set out to investigate this finding in a combined computational and experimental study. My personal contributions to this project were all computations, as well as the draft for the computational methods and results for the resulting **Paper I**. Consequently, the following text will mostly be concerned with the computational methods and results of the computational investigation. Experimental findings will only be included for comparisons or for supporting computational results.

Computational Methods

To study the CsF-mediated carboxylation, two computational methods were used. The long-range corrected DFT functional ωB97XD[47] was employed for all optimizations and frequency calculations. This functional was choosen because it had shown good accuracy in benchmark studies conducted by Goerigk, Grimme and co-workers[48] as well as by Mardirossian and Head-Gordon.[49] To obtain more accurat *ab initio* electronic energies, the DLPNO-CCSD(T) method in combination with the ZORA operator[38,39,50] was used for single point (SP) calculations with the resulting energies corrected for thermal, entropic and vibrational energies based on the DFT results.

Geometries were obtained with the 6-31+G* basis set[51–60] and SP energies with def2-TZVP (DFT) or ZORA-def2-QZVPP (DLPNO-CCSD(T)).[61] For Cs either the SDD ECP and basis set[62] (DFT) or the SARC-ZORA-TZVPP basis set[63] (DLPNO-CCSD(T)) were utilized. Energies in the text will be DLPNO-CCSD(T)-based unless stated otherwise. The employed software was Gaussian 16 Rev. B.01[64] for all DFT calculations and ORCA[36,37] 4.1.1 for all DLPNO-CCSD(T) calculations.

In addition to the "manual" search for TS conformations, the MC-AFIR[42,43,65,66] method was utilized to identify TSs. This was done in parallel to the other calculations to control if TSs were overlooked and if MC-AFIR could reproduce all "manually" found TSs. The software used for the MC-AFIR calculation was GRRM14[41] which was interfaced with Gaussian 09 Revision D.01[67] using DFT as described above.

Solvation effects were included in the DFT calculations as a PCM of dioxane. However, the DLPNO-CCSD(T) calculations had no solvation corrections and to control if this would introduce any significant errors, a solvation correction based on the difference of DFT-based electronic energies with and without PCM was calculated. These PCM-corrected DLPNO-CCSD(T) energies will not be used in the text but are listed in Table 3.1 for comparison. Furthermore, in a later project (related to **Paper II**) we investigated the effect of coordinating one explicit solvent molecule to the caesium atom.

Investigated Substrates and Mechanisms

Our focus for the computational investigation was the carboxylation, and the enquiry therefore started from the *in situ* formed organoboranes of *trans-*

stilbene (**sub1**), *trans*-β-methylstyrene (**sub2**) and cyclohexene (**sub3**), which are shown in Fig. 3.2. The first two substrates, **sub1** and **sub2**, can be carboxylated in presence of CsF, while the last one, **sub3**, is unreactive. In this way, computational results could be validated by predicting correct reactivity in agreement with experimental findings.
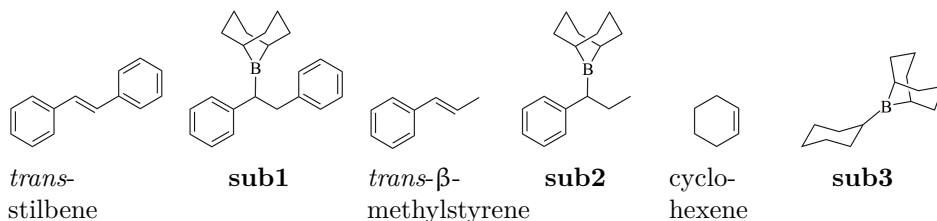
Figure 3.2: Formulas of the investigated organoboranes **sub1-3** and their precursors.

Three possible reaction paths were tested, which are shown in Fig. 3.3 and will be referred to as mechanism **A**, **B**, and **C**.

Mechanism A

Mechanism **A** has two steps (Fig. 3.3): first, the nucleophilic attack of the substrate's reactive carbon atom (carbon involved in the C-B bond) at the carbon of a CO_2 molecule, creating the boronic ester i_A1. The TS of this step, **TS(i0-i_A1)**, is stabilized by an interaction between one of the CO_2's oxygen atoms and the boron atom. This carboxylation step is followed by **TS(i_A1-p0)**, a transmetalation of the boronic ester i_A1 with CsF, resulting in the fluoroborane 9-F-9-BBN and the product **p0** (Cs salt of the carboxylic acid). This mechanism could be ruled out as it features very high reaction barriers of above 50 kcal/mol, which would result in negligible reaction rates at the reaction temperature of 393 K.
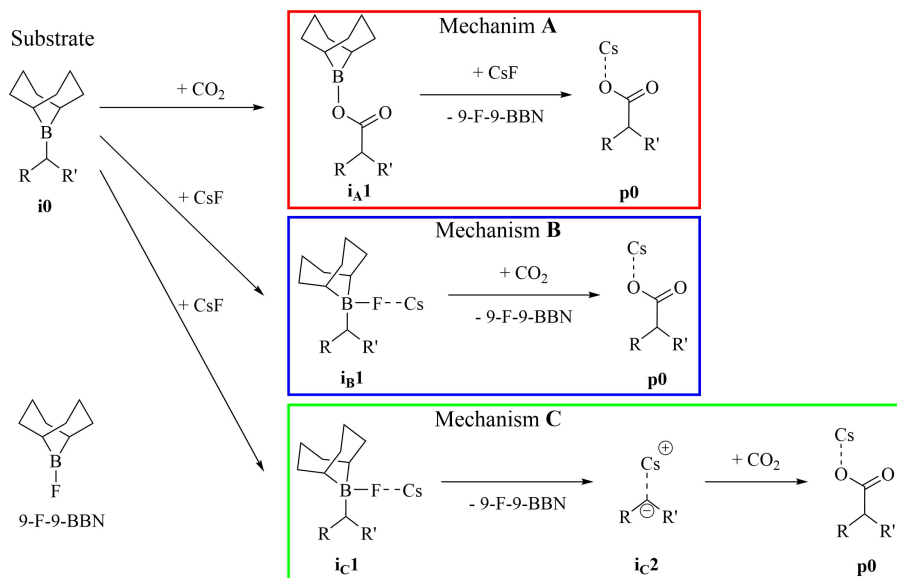
Figure 3.3: Investigated reaction mechanisms **A**, **B**, and **C** for the CsF-mediated carboxylation of organoboranes.

Mechanism B

Mechanism **B** starts with the nucleophilic attack of the fluoride ion of CsF at the boron atom of the substrate, forming a substrate-CsF adduct i_B1. This adduct can undergo a nucleophilic attack of the reactive carbon (C-B bond carbon) at a CO_2 molecule to form 9-F-9-BBN and the product **p0**, which is the rate-limiting step of mechanism **B**. This mechanism has high activation barriers of above $50\,\text{kcal/mol}$ for **sub1** (derived from *trans*-stilbene) and **sub2** (derived from *trans*-β-methylstyrene). For **sub3** (derived from cyclohexene) the barrier is $44.4\,\text{kcal/mol}$ (see Fig. 3.4) and this is the lowest barrier for this substrate and the investigated mechanisms. The Gibbs energy profile for **sub3** and mechanism **B** is therefore shown in Fig. 3.4. However, with mechanism **B** the rate-limiting barriers for all substrates are too high for reactivity.

Mechanism C

In contrast to mechanism **A** and **B**, the third investigated mechanism **C** is capable of explaining the experimentally observed reactivity. Accordingly, the Gibbs energy profile for **sub1** and mechanism **C** is shown in Fig. 3.4, with **sub2** not added as it is very similar to **sub1**. Mechanism **C** shares the first step with mechanism **B**, which is the formation of the CsF-substrate adduct **i_C1** (= **i_B1**). Intermediate **i_C1** is the resting state (intermediate with the lowest energy) of the reaction for **sub1** (-14.6 kcal/mol) and **sub2** (-15.5 kcal/mol). In the following step, the C-B bond is broken, cleaving of a 9-F-9-BBN molecule and forming an organocaesium intermediate **i_C2** via **TS(i_C1-i_C2)**. This organocaesium intermediate **i_C2** is shown in Fig. 3.5 and its formation is the rate-limiting step for **sub1** (18.6 kcal/mol relative to **i0**) and **sub2** (22.1 kcal/mol relative to **i0**).
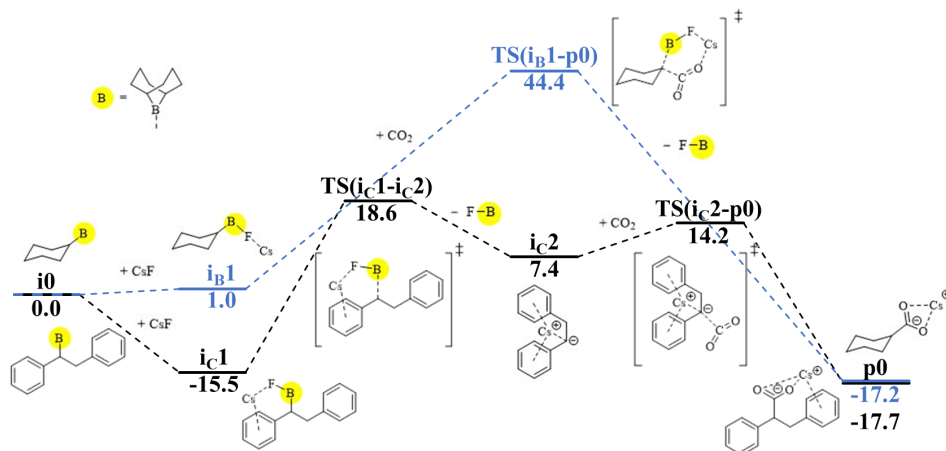
Figure 3.4: Computed Gibbs energy profile (in kcal/mol, at 393 K) for **sub1** with mechanism **C** (black) and **sub3** with mechanism **B** (blue).

In connection with **TS(i_C1-i_C2)**, two things should be mentioned. First, this TS could only be optimized with ωB97XD (or DFT functionals of the

same family), as several optimization attempts with different DFT functionals (amongst others PBE-D3BJ and B3LYP-D3BJ) failed, and second, the imaginary mode of the TS is very small ($< 40i$ cm^{-1}). Relaxed scans showed that the PES is rather flat around **TS(i$_C$1-i$_C$2)** and the long bond distances during the bond breaking (> 3 Å) make dispersion interactions important, which could explain the difficulties in trying to optimize with "regular" (not long-range-corrected) DFT functionals. Additional intrinsic reaction coordinate (IRC) calculations supported **TS(i$_C$1-i$_C$2)** and it is possible that the small imaginary frequency is an intrinsic feature of this TS. This can be explained as vibrational frequencies are proportional to the square root of the force constant divided by the reduced mass, resulting in low frequencies in case of a weak bond and heavy atoms involved.

The last step of mechanism **C** is the carboxylation **TS(i$_C$2-p0)** of the organocaesium intermediate (**i$_C$2**) via a nucleophilic attack of the reactive carbon (carbon with the formal negative charge) at a CO_2 resulting in the product. This step is rate-limiting for **sub3**, but not for **sub1** and **sub2**.

The calculations yielded the following rate-limiting barriers for mechanism **C**: 34.0 kcal/mol for **sub1**, 36.7 kcal/mol for **sub2**, and 51.1 kcal/mol for **sub3**. For **sub1** and **sub3** these barriers are higher than the energy of the rate-limiting step **TS(i$_C$1-i$_C$2)**, as the intermediate **i$_C$1** has a lower energy than **i0** for these two substrate.

Based on the discussion of Baik and co-workers[23], a rate-limiting barrier of 33.2 kcal/mol is the upper limit for reactivity at 393 K. The barriers for **sub1** and **sub2** are higher than this limit, but considering possible errors from e.g. not having equilibrium structures in respect to DLPNO-CCSD(T), we argue that mechanism **C** is capable to explain the experimentally ob-

served reactivity of **sub1** and **sub2**.

Overview of all Barriers

In Table 3.1 the rate-limiting barriers for all substrates, mechanisms, and methods are listed.   For **sub3**, the barriers for all investigated mechanisms are very high and considerably higher than the maximum barrier of 33.2 kcal/mol at 393 K, based on the discussion of Baik and co-workers.[23] This is in agreement with the experimentally observed lack of reactivity of **sub3** for the given reaction condition (**Paper I**).

The substrates **sub1** and **sub2** similarly yield far too high barrier with the exception of mechanism **C**. The barriers for mechanism **C** are still too high by 0.8 (**sub1**) and 3.5 kcal/mol (**sub2**). However, it can be argued that based on the findings of Reiher and co-workers[68], the error of DLPNO-CCSD(T) can be up to 7 kcal/mol for certain reactions, meaning that mechanism **C** is capable of explaining the observed reactivity. Additional possible error sources such as non-equilibrium structures with respect to DLPNO-CCSD(T) or the CsF reference state, might further explain the slightly too high barriers.

The trend of reactivity with mechanism **C** for **sub1** and **sub2** is consistent for all employed methods (see Table 3.1) and in good agreement with the observed reactivities, as experiments performed by Ashot Gevorgyan (see **Paper I**), showed reactivity only for **sub1** and **sub2**.

Table 3.1: All computed rate-limiting barriers for the investigated substrates, mechanisms and used methods. DLPNO-CCSD(T)$_{nosolv}$ are the energies as used in the text and DLPNO-CCSD(T)$_{solv}$ include PCM corrections from the DFT calculations. All Gibbs energies are at $393\,$K and in kcal/mol.

Method	Mechanism	sub1	sub2	sub3
	A	72.9	67.5	57.7
DLPNO-CCSD(T)$_{nosolv}$	B	51.9	52.3	44.4
	C	34.0	36.7	51.1
	A	68.4	63.0	58.2
DLPNO-CCSD(T)$_{solv}$	B	49.9	50.1	47.6
	C	34.7	36.9	52.3
	A	75.4	68.5	62.1
ωB97XD	B	43.7	48.3	47.6
	C	32.5	34.0	57.1

Organocaesium Intermediate i$_C$2

The calculations suggest the existence of the organocaesium intermediate **i$_C$2** (shown in Fig. 3.5) and it can be concluded that the stability of this intermediate is crucial for the reactivity of a substrate. From the structures for **sub1** and **sub2** one can conclude three things: First, a bond between the caesium and the formally negative charged carbon does not exist, second, the negative charge is delocalized over the phenyl group and third, Cs is interacting with the delocalized negative charge and the π-electrons of the phenyl groups. Similar results were previous reported suggesting that this Cs-π-electron interaction can be crucial for the reactivity of a reactant.[69]

For **sub3** there is no delocalization of the negative charge or Cs-π-electron interactions, which could explain its relatively high energy.

sub1 (7.4 kcal/mol)   **sub2** (12.7 kcal/mol)   **sub3** (37.2 kcal/mol)
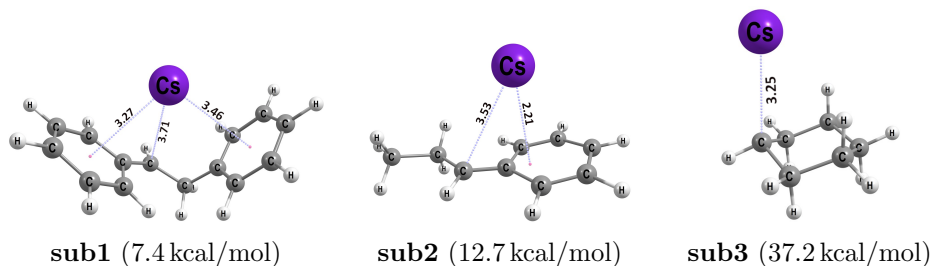
Figure 3.5: Structure and Gibbs energy (relative to **i0**) of the organocaesium intermediate **i$_C$2** for **sub1-3**. Bond lengths are given in Å.

Using a rough estimate, one can conclude that the Cs-π-interaction with one phenyl group accounts for approximately 6 kcal/mol by comparing the energies of **i$_C$2** for **sub1** and **sub2**. Using this number and making a similar rough estimate for **sub2** and **sub3**, one can predict the energy change due to electron delocalization with a phenyl group to account for approximately 20 kcal/mol.

This is a rough approach, but it would support the conclusion that the electron delocalization might be the dominant factor in determining the stability of **i$_C$2** and consequently for the reactivity of a substrate. However, to answer the question of the precise origin of the stability, more substrates would need to be investigated.

Considering the possible interest of creating a stereoselective carboxylation using CsF-mediated reactions, it is very unlikely that this will succeed as the organocaesium intermediate **i$_C$2** is very flexible and can, as the caesium ion is not strongly bound, change fast between conformations. This is supported by experimental findings by Ashot Gevorgyan, who could show

stereoselectivity for the hydroboration step (36 % ee (Enantiomeric excess) using (−)-Isopinocampheylborane TMEDA complex) but observed the formation of a racemic mixture during the carboxylation reaction (see **Paper I**).

Cs-CO$_2$ Interaction

As we are generally interested in the activation of CO_2 during the CO_2 insertion, we calculated several TSs with Cs-CO$_2$ interactions (inner sphere TS) and without (outer sphere TS) to estimate their importance. The structures and energies of these TSs are shown in Fig 3.6 for **sub1** and in Fig 3.7 for **sub2**.

Inner sphere TS (14.9 kcal/mol)   Outer sphere TS (14.2 kcal/mol)
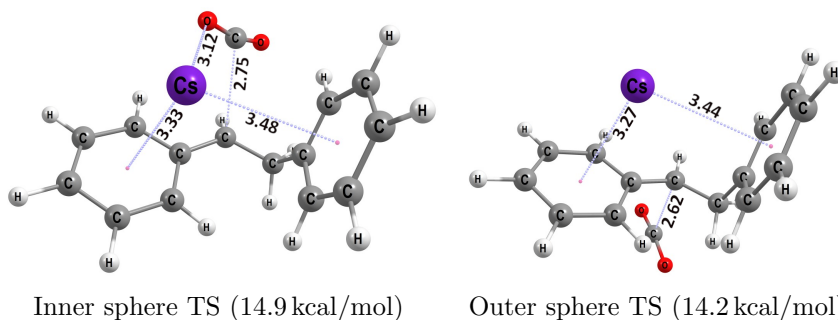
Figure 3.6: Structures of **TS(i$_C$2-p0)** for **sub1**. All bond lengths are given in Å.

For **sub1** the Cs-CO$_2$ interaction seems to be negligible as the inner sphere TS is higher in energy than the outer sphere TS, but by only 0.4 kcal/mol. This is likely due to the CO_2 molecule interfering with the Cs-π-electron interaction during the insertion.

For **sub2** the inner sphere TS is preferred over the outer sphere TS by 1.6 kcal/mol. This shows that steric effects are less important compared

Inner sphere TS (19.9 kcal/mol)   Outer sphere TS (21.5 kcal/mol)
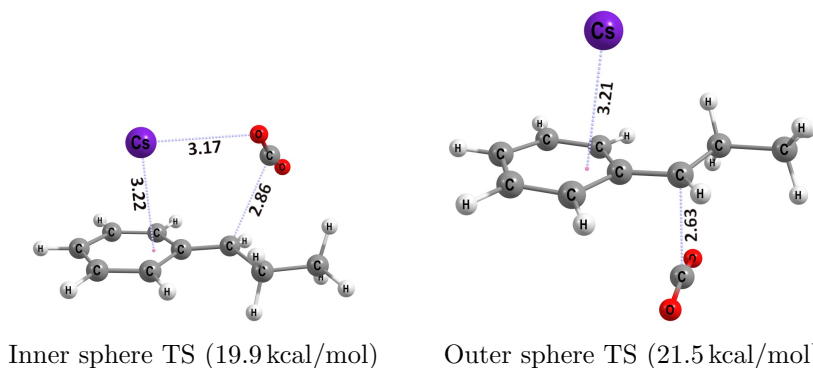
Figure 3.7: Structures of the **TS(i$_C$2-p0)** for **sub2**. All bond lengths are given in Å.

with **sub1** and that caesium ions can activate CO_2 during the insertion. This is in line with experimental findings of Hazari and co-workers[70,71] that observed increased reaction rates for hydrogenation reaction of CO_2 in presence of alkali ions.

Use of AFIR

As mentioned, (MC-)AFIR was used, parallel to the "manual" search, to identify CO_2 insertion TSs. For these AFIR calculations the attacking intermediate, depending on the mechanism (**i$_B$1**, **i$_C$2**, or **i0**), and a CO_2 molecule were defined as independent fragments. It was defined that an artificial attractive potential should be added between the attacking carbon of the intermediate and the carbon of CO_2. Two modes were used, either the program was set to stop after 50 attempts or after the last 10 attempts, if no new approximated TSs were found. With these settings, AFIR was capable of identifying several approximated TSs and for several substrates and mechanisms the final geometries from these approximated TSs could be shown to be lower in energy than any of the "manual" identified TSs. This

makes AFIR a useful tool for, at least, controlling if energetically lower TSs can be found. In summary, I regard it as a useful tool for investigation of reaction mechanisms with the downside of the license model which currently makes installation on computer clusters difficult.

CsF Reference State

A challenging part of the investigation was the modelling of CsF, as the structure of CsF dissolved in 1,4-dioxane is not known. In this project, a CsF dimer $(CsF)_2$ (see Fig. 3.8) was used as a reference to approximate the average energy, with half the energy of one $(CsF)_2$ used as energy of one CsF unit. With the $(CsF)_2$ reference state, the energy of one CsF is reduced by 7.0 kcal/mol relative to the "free" CsF.

$(CsF)_2$ $(CsF)_4$
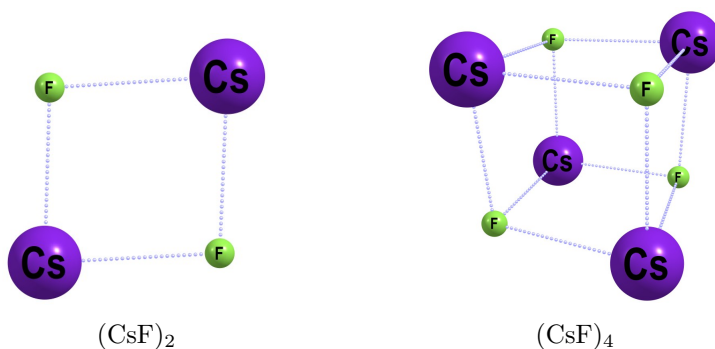
Figure 3.8: Structures of the CsF reference structures $(CsF)_2$ and $(CsF)_4$.

For the second project, related to **Paper II**, a CsF-tetramer $(CsF)_4$ (see Fig. 3.8) was additionally used as a reference state for **sub2** and **sub3**. The energy of CsF is reduced by 8.9 kcal/mol relative to the "free" CsF, when the $(CsF)_4$ reference state is used. The rate-limiting barriers with the $(CsF)_4$ reference are listed in Table 3.3 (Section 3.2). As a different computational

protocol was used for the second project, the barriers in Table 3.3 should be compared with the barriers in Table 3.2 (Section 3.2).

When taking only the CsF-mediated carboxylations with **sub1** and **sub2** into account, the choice of CsF reference state is not important because the change in energy for a CsF unit equally affects the resting state ($\mathbf{i_C1}$ or $\mathbf{i_B1}$) and the energetically highest TS ($\mathbf{TS(i_C1\text{-}i_C2)}$ or $\mathbf{TS(i_B1\text{-}i_B2)}$), resulting in no change of the rate-limiting barriers.

This is different for **sub3** as it has a different resting state from **sub1** and **sub2**. Therefore, changing from the $(CsF)_2$ to the $(CsF)_4$ reference state results in an increase of the rate-limiting barrier by 2.7 kcal/mol. However, **sub3** has too high barriers independently of the utilized CsF reference state and thus this choice does not affect any mechanistic conclusions. When comparing the CsF-mediated mechanism **C** with the later introduced Cu-catalyzed mechanism (**D**) this choice is important and therefore will be discussed again for the second project (**Paper II**).

Solvation of the Cs Ion

As the solvation of the caesium ion could be important for reaction energies, calculations were also performed with one explicit dioxane molecule stabilizing the caesium ion in addition to PCM. These calculations were performed on mechanism **C** with **sub2** and **sub3** as part of the second project (**Paper II**). A slightly different computational protocol was used for the second project and therefore the calculated barriers will be slightly different. The results of "pure PCM" and "PCM + one explicit dioxane" solvation are given in Table 3.2 (Section 3.2) and show that for mechanism **C** the explicit solvent molecule increases the rate-limiting barrier for **sub2**

by 1.8 kcal/mol and decreases the barriers for **sub3** by 5.6 kcal/mol. These differences are not negligible but do not affect any mechanistic conclusions.

Additionally, more than one explicit dioxane moelcule was tested but it was found than one explicit molecule already accounts for the majority of the solvation effects. Therefore adding more explicit solvent would result in a large number of possible conformations without adding any benefits.

Conclusion

In this project we presented a reaction mechanism capable of reproducing the experimentally observed substrate preference of the CsF-mediated carboxylation by studying three different substrates and reaction mechanisms. Only the reaction mechanism **C** showed reasonable rate-limiting barriers, but only for the substrates **sub1** and **sub2**. This is in agreement with experimental findings showing reactivity only for **sub1** and **sub2** at 393 K. Furthermore, mechanism **C** predicts the formation of an organocaesium intermediate and the stability of this intermediate might be crucial for the reactivity of a substrate, with delocalization of negative charges and Cs-π-electron interactions being likely the decisive factors.

We investigated the activation of CO_2 by interaction with Cs and the results suggest that these interactions play a minor role as the calculations showed energy differences of 1.6 kcal/mol or less.

For future research it might be of interest to test more substrates, or bases/additives to better understand the factors influencing the activation energies of the mechanisms.

3.2   Mechanistic Insights into Copper-Catalyzed Carboxylations (Paper II)

Introduction

In this project, we investigated the Cu(I)-IPr (IPr = 1,3-bis(2,6-diisopropylphenyl)imidazol-2-ylidene)-catalyzed hydrocarboxylation of alkenes with CO_2 as published by Skrydstrup, Nielsen and co-workers[46] in 2017 (see Fig. 3.9). Skrydstrups protocol was derived from previous systems independently published by Hou and co-workers[72] as well as Ohmiya, Sawamura and co-workers[73] in 2011. It is a two-step procedure of a hydroboration with (9-BBN)$_2$ and an *in situ* carboxylation with a Cu(I)-IPr catalyst and CO_2. Skrydstrup, Nielsen and co-workers were able to expand the scope of the reaction by replacing the strong alkoxides, used by Hou, Ohmiya and Sawamura, with the milder CsF.[46] In the previous project we investigated the CsF-mediated carboxylation of the *in situ* organoboranes and we will here compare it with the Cu-catalyzed carboxylation as both mechanisms are possible to occur because the reaction mixture contains Cu-IPr as well as CsF.
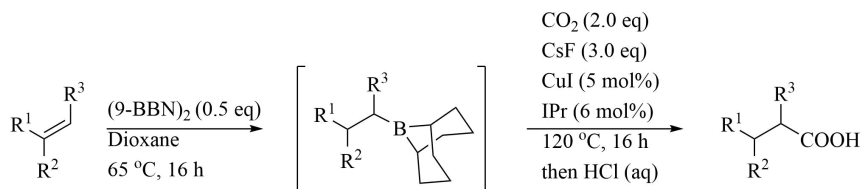
Figure 3.9: Reaction protocol for the carboxylation of alkenes with CO_2 as published by Skrydstrup, Nielsen and co-workers.[46]

Like the previous project, this work was done in a cooperation of ex-

perimental and computational work. My personal contributions were all computations and the draft for the article.

Computational Methods

To investigate the reaction mechanism of Cu-IPr-catalyzed carboxylation DFT and DLPNO-CCSD(T)[30,31] were used. Three DFT functionals were employed, ωB97XD[47], B3LYP[74], and PBE[75]; the latter two in combination with the Grimme dispersion correction D3[27] including the Becke-Johnson (BJ) damping.[76] Ground state and TS geometries as well as vibrations were obtained for each DFT functional at a 6-31+G* basis set level,[51–60] with the SDD ECP and basis set employed for Cu and Cs.[62,77,78]

To gain *ab initio* electronic energies, DLPNO-CCSD(T) together with ZORA[38,39,50] was used on the ωB97XD-based geometries. The final DLPNO-CCSD(T) energies were calculated by adding the DFT-based energy (thermal, vibrational, and entropic) and solvation effect corrections to the electronic energy.

SP electronic energies for DFT were obtained at the def2-TZVP[61] basis set level, while for DLPNO-CCSD(T) the basis sets ma-ZORA-def2-TZVPP[61] (for non-Cs elements) and SARC-ZORA-TZVPP[63] (for Cs) were employed. Gaussian 16 Rev. B.01[64] was used for all DFT calculations and ORCA[36,37] 4.2.0 was used for the DLPNO-CCSD(T) calculations.

Like in the previous work (**Paper I**), the CsF was modelled using a CsF-dimer as reference state for the energy. The usage of other reference states CsF-tetramer $(CsF)_4$ and the effect of this change will be discussed. Unless stated otherwise, given energies are based on DLPNO-CCSD(T) and

geometries are based on ωB97XD.

Investigated Substrates

We concentrated the investigation on alkenes and the second step of the reaction, the carboxylation of the *in situ* organobranes with CO_2. For this purpose we employed the organoborane derivatives of *trans*-β-methylstyrene and cyclohexene in our calculations. These two substrates were used in the first project and therefore the same names, **sub2** and **sub3**, will be used here. No truncations were made and all substrates as well as the ligand IPr are shown in Fig. 3.10.

trans-β-   **sub2**   cyclohex-   **sub3**   IPr
methylstyrene   ene
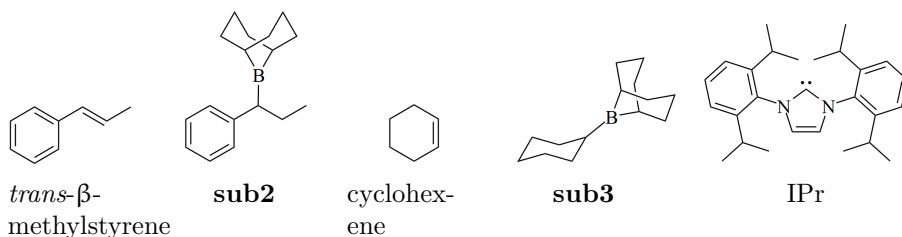
Figure 3.10: Formulas of the investigated substrates (**sub2-3**), their precursors, and the ligand IPr.

Cu-Catalyzed Mechanism

The investigation was started from the mechanism proposed by Skrydstrup, Nielsen and co-workers[46] in Fig. 3.11, which suggested F-Cu-IPr as reactive species of the catalyst and the formation of an organocopper intermediate before the carboxylation. This mechanism will be called **D** or Cu-catalyzed mechanism.

The Gibbs energies and schematic structures of all intermedates and
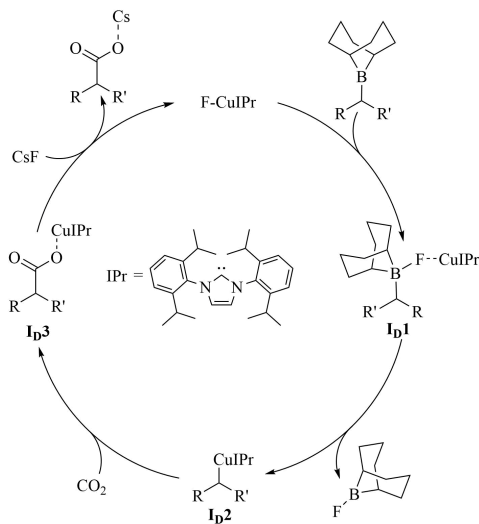
Figure 3.11: Reaction mechanism for the Cu-IPr-catalyzed carboxylation of organoboranes based on Skrydstrup, Nielsen and co-workers' proposal[46].

TSs for mechanism **D** are shown in Fig. 3.12. The calculations show the formation of a substrate-catalyst adduct **i$_D$1** via the partial transfer of the fluoride ion from the active species (F-Cu-IPr) to the boron of the substrate, as first step of the catalytic cycle. This adduct can undergo a transmetalation **TS(i$_D$1-i$_D$2)** between the boron and the copper, breaking the C-B and Cu-F bond and forming a new Cu-C bond. This coincides with the release of a 9-F-9-BBN and results in the organocopper intermediate **i$_D$2** and the structures for this TS are shown in Fig. 3.13.

This organocopper intermediate is reminiscent of the organocaesium intermdiate **i$_C$2** presented in the previous project, as both are formed before the CO_2 insertion step. However, there are two important differences: First, in contrast to organocaesium intermediate **i$_C$2**, the organocopper intermediate **i$_D$2** features a strong metal-carbon bond and second, **i$_D$2** shows no metal-π-electron interactions. These two differences are likely resulting in
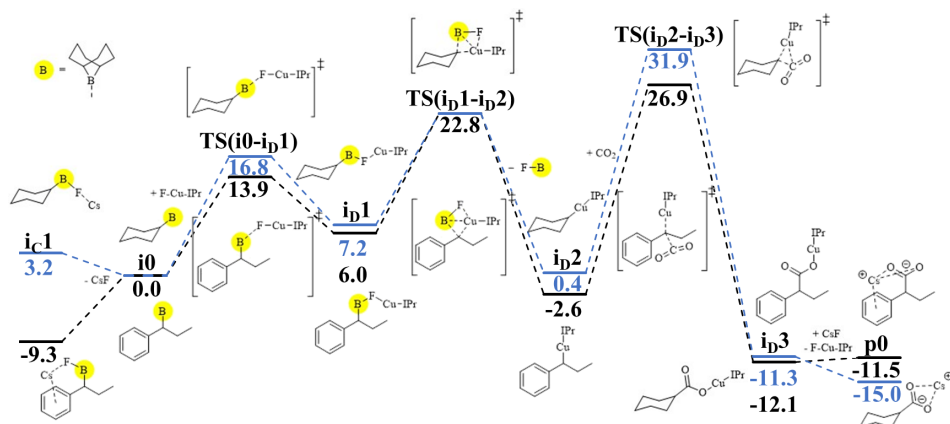
Figure 3.12: Computed Gibbs energy profile for the Cu-IPr-catalyzed carboxylation of **sub2** (black) and **sub3** (blue) at 393 K. Energies are based on DLPNO-CCSD(T) and given in kcal/mol. It should be noted that the CsF-substrate intermediate i_C1 is an off-cycle species but important for determining the rate-limiting barrier and therefore part of the profile.

the organocopper intermediate i_D2 being relatively stable independently of the substrate, as no negative charges require stabilization from delocalization or additional metal-π-electron interactions.

The next step in the reaction mechanism is a nucleophilic attack of i_D2 at a CO_2 molecule. This attack **TS(i_D2-i_D3)** is the rate-limiting step of the reaction, with energies of 26.9 kcal/mol for **sub2** and 31.9 kcal/mol for **sub3**.

To determine the rate-limiting barriers for mechanism **D** it is important to include the off-cycle reactant i_C1 presented in the previous project (**Paper I**), as it constitutes the resting state for **sub2** with -9.3 kcal/mol. The resulting rate-limiting barriers are therefore 36.2 kcal/mol for **sub2** and 31.9 kcal/mol for **sub3**. Considering the dicussion by Baik and co-workers[23] a rate-limiting barrier of 33.2 kcal/mol is the maximum for 393 K. This means that **sub3** should be reactive, while the barrier for **sub2** is too
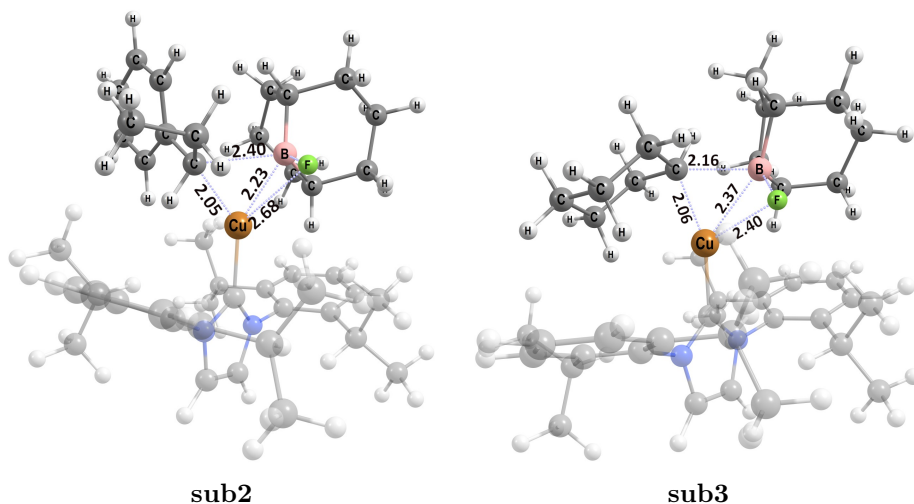
Figure 3.13: Structures of the transmetalation **TS(i$_D$1-i$_D$2)** for **sub2** and **sub3**. The IPr ligand is transparent for clarity and bond lengths are given in Å.

high. However, considering that the error of DLPNO-CCSD(T) can be up to 7 kcal/mol for some reactions, as well as other possible errror sources this barrier is not unreasonably high.[68] Therefore, we argue that mechanism **D** is capable to explain the observed reactivity of both investigated substrates.

Alternative Cu-Catalyzed Mechanism

Additionally to mechanism **D**, we investigated a modified version of it which is called **E** and is shown in Fig. 3.14. This modified mechanism **E** is very similar to mechanism **D** but the difference is that the active species (F-Cu-IPr) reacts with the **i$_C$1** intermediate instead of the substrate **i0** as first step of the reaction. Not all intermediates and TSs of this mechanism could be optimized but the preliminary results suggest rate-limiting barriers of at least 47.7 kcal/mol for **sub2** and 38.0 kcal/mol for **sub3**. For **sub2** this
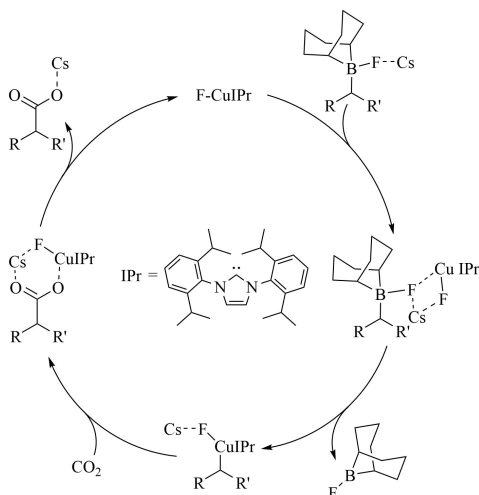
Figure 3.14: Reaction mechanism for the Cu-IPr-catalyzed mechanism **E**.

barrier is much higher than for mechanism **D** and for **sub3** the barrier is similar. However, the TS expected to be rate-limiting based on the **sub2** results, could not be optimized for **sub3** and it is likely for the barrier to increase significantly if the mechanism **E** could have been fully optimized.

Cu-CO$_2$ Interactions

For **TS(i$_D$2-i$_D$3)** several TSs constituting different modes of CO$_2$ insertion were identified. The mode of CO$_2$ insertion is interesting for two reasons: first, as CO$_2$ is an inert molecule it is important to know if the metal center stabilizes the TS (inner sphere) or if not (outer sphere).[79] It could be shown that Lewis acid additives enhance the reaction rates of CO$_2$ hydrogenation reactions, which is likely the result of CO$_2$ activation during an outer sphere TS.[70,71] Knowing the metal-CO$_2$ interaction therefore helps the design of catalysts and additives. Second, if the attacking nucleophile is prochiral or chiral the mode of insertion defines the stereocenter with inner and outer

sphere TSs yielding different enantiomers. Inner sphere TSs result in a retention, while outer sphere TSs may cause an inversion of configuration of the chiral center, if the attack occurs via a S_E2(back) mode.

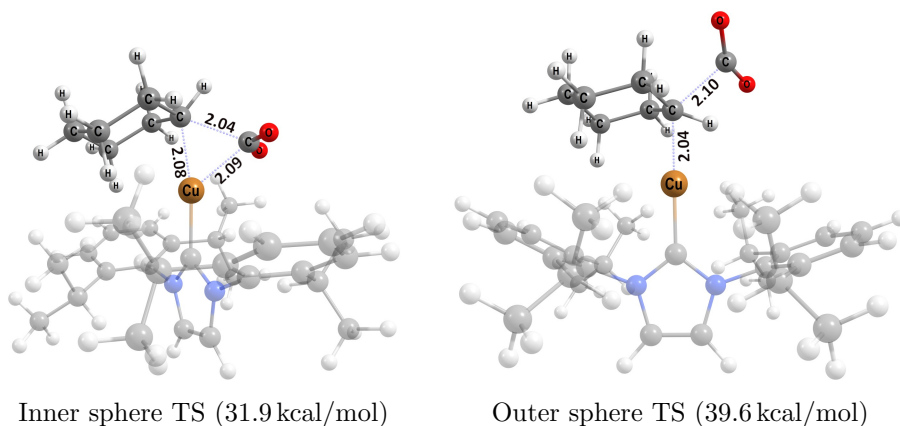Inner sphere TS (27.2 kcal/mol)   Outer sphere TS (26.9 kcal/mol)
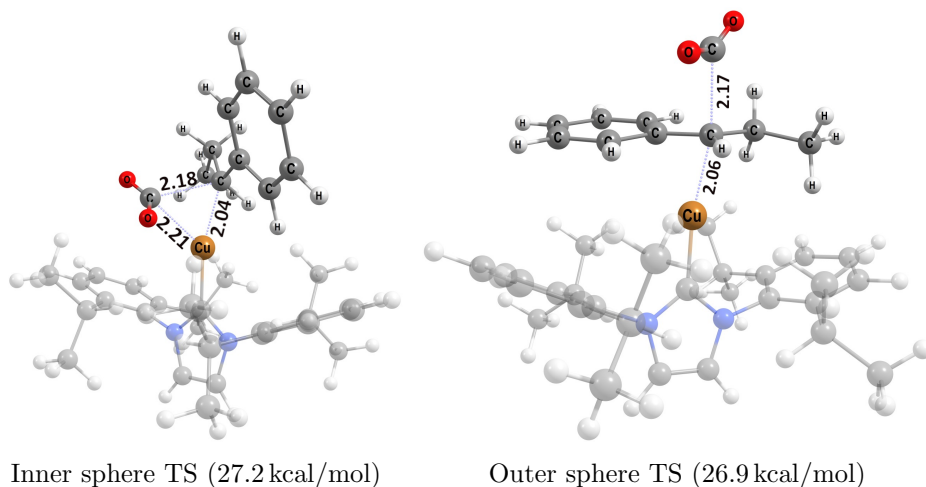
Figure 3.15: Structures of the CO_2 insertion TSs (**TS(i_D2-i_D3)**) for **sub2**. The IPr ligand is transparent for clarity and bond lengths are in Å.

For **sub2** (Fig. 3.15) the inner and outer TS geometries have very similar energies, with differences ranging from 0.3 (DLPNO-CCSD(T) and B3LYP-D3BJ) to 1.8 kcal/mol (ωB97XD) in favour of the outer sphere TS. These small energy differences indicate that the Cu-CO_2 interaction is weak and of a similar size to the energy increase due to steric effects. This is in contrast to the findings of Lu and co-workers who published an inner sphere mechanism for a similar system.[80] However, it is unclear if the outer sphere TS for their system was calculated. These small energy differences indicate that, for a chiral version of this reaction, a poor selectivity can be expected for the carboxylation of **sub2** at the given reaction temperature.

To improve the reactivity and selectivity of the carboxylation reaction for benzylic substrates (like **sub2**) it might be of interest to use additives

to stabilize the CO_2 during the outer sphere TS and thus also increase the energy difference with the inner sphere TS. Utilizing e.g. Lewis acid additives might be beneficial as they have been shown to increase the reaction rates for hydrogenation of CO_2 and it is hypothesised that this is a result of CO_2 activation.[70,71] Alternatively the use of bulkier substituents at the NHC ligand might increase the energy of the inner sphere TS resulting in an increased energy difference between inner and outer sphere TSs, but at the risk of also increasing the barrier of the transmetalation **TS(i_D1-i_D2)**.

Inner sphere TS (31.9 kcal/mol)   Outer sphere TS (39.6 kcal/mol)

Figure 3.16: Structures of the CO_2 insertion TSs (**TS(i_D2-i_D3)**) for **sub3**. The IPr ligand is transparent for clarity and bond lengths are in Å.

The behaviour of **sub3** (Fig. 3.16) is rather different from **sub2**, as the inner sphere TS is considerably lower in energy than the outer sphere TS for all employed methods, with differences ranging from 4.5 (PBE-D3BJ) to 7.7 kcal/mol (DLPNO-CCSD(T)). These results indicate that a Cu-CO_2 interaction is important for the CO_2 insertion into non-benzylic substrates and would translate to good stereoselectivity.

The selectivity could further be improved by using less bulky NHC ligands, or employing substituents at the ligand capable of further stabilizing

the CO_2 during the insertion and increasing the energy difference between inner and outer TS.

We previously summarized computational studies of carbon-carbon bond formation with CO_2 in **Paper IV** and we concluded that the type of nucleophile seem to be important for the CO_2 insertion mode. The computational studies suggest that C_{sp} carbons have a preference for outer sphere TSs, while for C_{sp^2} and C_{sp^3} nucleophiles an inner sphere TS seems to be preferred. However, we also noted in **Paper IV** that it is often unclear if outer sphere TSs were investigated for C_{sp^3} carbons and we suggest to include such TSs in computational studies. Our results on the Cu-catalyzed carboxylation suggest that for benzylic substrates (**sub2**) inner and outer sphere TSs have comparable barriers and we observed a similar behaviour in a related study from our group on Cu-catalyzed boracarboxylation of benzylic substrates.[81] For non-benzylic C_{sp^3} nucleophiles on the other hand a general preference for inner sphere mechanisms is observed for both Cu-catalyzed (**Paper II**) as well as Ni(I)-catalyzed carboxylations (**Paper III**, discussed in Section 3.3).

With stereoselective synthesis in mind, the calculations suggest that for non-benzylic substrates (**sub3**) good ee's may be possible with a chiral Cu-NHC complex while for benzylic substrates (**sub2**) only poor ee's can be expected, as inner and outer sphere TS would compete. To improve the selectivity for one pathway of the Cu-catalyzed carboxylation it might be of interest to either add Lewis acids for CO_2 activation[70,71] or to increase the bulkiness of the NHC-substituents[81], as both strategies may increase the preference for outer sphere TSs.

Comparison with CsF-Mediated Carboxylation

From the reaction conditions shown in Fig. 3.9 it can be seen that the reaction mixture contains the Cu-IPr catalyst as well as CsF. In the previous project (**Paper I**) we could show that CsF mediates the carboxylation of benzylic organoboranes (**sub1** and **sub2**) with CO_2 and this implies that it is relevant to evaluate which carboxylation agent is the preferred one for **sub2** and **sub3**. In Table 3.2 we compared the rate-limiting barriers for the Cu-catalyzed mechanism **D** and the CsF-mediated mechanism **C** for the organoboranes **sub2** and **sub3** to uncover if only one or both mechanisms are responsible for the reactivity.

For **sub2**, no clear conclusion can be made as the employed methods yield different results. PBE-D3BJ predicts a preference for the Cu-catalyzed (**D**), ωB97XD predicts a preference of the CsF-mediated mechanism (**C**), while for DLNPO-CCSD(T) and B3LYP-D3BJ, both are very similar in energy.

The calculations give no clear preference for any of the two mechanisms **C** or **D** and it is thus possible that both mechanisms are competing with each other for **sub2**. As mechanism **C** leads to racemic mixtures, as discussed in the previous project, this is detrimental for any attempts of a stereoselective CO_2 insertion.

In the previous project (**Paper I**) it was shown that **sub3** is not reactive under the conditions of the CsF-mediated carboxylation, but it reacts in presence of Cu-IPr. This is reflected by the fact that only the Cu-catalyzed mechanism **D** gives accessible barriers at 393 K, while the CsF-mediated mechanism gives far too high barriers. Accordingly, for **sub3** the energy differences are large ranging from 15.0 (ωB97XD with expl. solvent) to

Table 3.2: Rate-limiting barriers for the Cu-catalyzed (**D**) and CsF-mediated (**C**) carboxylation of **sub2** and **sub3**. All energies are Gibbs energies at 393 K and given in kcal/mol. PCM+Expl. indicates the use of an implicit 1,4-dioxane molecule on the Cs ion in addition to PCM. The PBE-D3BJ and B3LYP-D3BJ barriers are based on SP calculations as **TS(i$_C$1-i$_C$2)** could only be optimized with ωB97XD.

Substrate	Method	Solvation	**D**	**C**	$\Delta(\Delta G_{\text{D-C}})$
	DLPNO-CCSD(T)	PCM	36.2	37.0	-0.8
	DLPNO-CCSD(T)	PCM+Expl.	39.2	38.6	0.6
	ωB97XD	PCM	40.4	36.4	4.0
sub2	ωB97XD	PCM+Expl.	40.6	35.6	5.0
	PBE-D3BJ	PCM	25.6	29.6	-4.0
	B3LYP-D3BJ	PCM	29.8	28.9	0.9
	DLPNO-CCSD(T)	PCM	31.9	53.3	-21.4
	DLPNO-CCSD(T)	PCM+Expl.	31.9	47.7	-15.8
	ωB97XD	PCM	33.6	53.9	-20.3
sub3	ωB97XD	PCM+Expl.	33.6	48.6	-15.0
	PBE-D3BJ	PCM	26.4	49.6	-23.2
	B3LYP-D3BJ	PCM	29.9	50.5	-20.6

23.2 kcal/mol (PBE-D3BJ) in favour of mechanism **D**.

The results predict that mechanism **C** plays no role in the carboxylation of **sub3** and the additive CsF should therefore not affect the reaction via any competing mechanisms.

Effect of CsF Reference State

In the previous project (**Paper I**) the reference state for CsF was discussed (Fig. 3.8). As it was mentioned, the structure of dissolved CsF is not known

and a CsF-dimer $(CsF)_2$ was used as reference state for the average energy of one CsF unit. While the exact choice of CsF reference state has little influence when focusing solely on the CsF-mediated mechanism, it is important when comparing the CsF-mediated **C** and Cu-catalyzed mechanism **D**.

An alternative CsF reference state, a CsF-tetramer $(CsF)_4$, shown along $(CsF)_2$ in Fig. 3.8, was utilized for this project and the rate-limiting barriers with this CsF reference state are listed in Table 3.3. When using this $(CsF)_4$

Table 3.3: Rate-limiting barriers for the Cu-catalyzed (**D**) and CsF-mediated (**C**) carboxylation of **sub2** and **sub3** when using the CsF-tetramer $(CsF)_4$. All energies are given in kcal/mol and at $393\,K$. The PBE-D3BJ and B3LYP-D3BJ barriers are based on SP calculations as $\mathbf{TS(i_C1\text{-}i_C2)}$ could only be optimized with ωB97XD.

Substrate	Method	D	C	$\Delta(\Delta G_{\mathbf{D\text{-}C}})$
	DLPNO-CCSD(T)	33.5	37.0	-3.5
sub2	ωB97XD	29.9	36.4	-6.5
	PBE-D3BJ	25.6	29.6	-4.0
	B3LYP-D3BJ	29.8	28.9	0.9
	DLPNO-CCSD(T)	31.9	56.0	-24.1
sub3	ωB97XD	33.6	64.4	-30.8
	PBE-D3BJ	26.4	52.9	-26.5
	B3LYP-D3BJ	29.9	54.2	-24.3

as a reference state, the results for **sub2** suggest that the Cu-catalyzed carboxylation **D** is energetically preferred over the CsF-mediated carboxylation **C** as all methods (except for B3LYP-D3BJ) predict differences in the rate-limiting barriers of 3.5 to $6.5\,kcal/mol$ in favour of **D**. These energy

differences suggest that mechanism **D** is likely much faster than mechanism **C** to the point that mechanism **C** could be neglected in presence of the Cu-IPr catalyst.

For **sub3** the change of CsF reference state has no effect on the conclusions as it only increases the already large difference in the preference for the Cu-catalyzed carboxylation mechanism (**D**).

Conclusion

In conclusion, we used DFT and DLPNO-CCSD(T) to investigate the Cu(I)-IPr-catalyzed carboxylation of *in situ* formed organoboranes, based on the reaction protocol of Skrydstrup, Nielsen and co-workers[46]. Our results support the following conclusion: The Cu(I)-catalyzed carboxylation (**D**) is feasible for both investigated substrates at 393 K and can therefore explain the experimentally observed reactivity. For non-benzylic substrates (**sub3**) the Cu-CO_2 interaction is crucial during CO_2 insertion, while for benzylic substrates (**sub2**) it is of minor importance. Non-benzylic substrates (**sub3**) react only via the Cu-catalyzed mechanism **D**, while for benzylic substrates (**sub2**) the Cu-catalyzed mechanism **D** may have similar reaction rates to a CsF-mediated carboxylation **C**, discussed in **Paper I**.

As non-benzylic substrates (**sub3**) have a clear preference for an inner sphere TS, a stereoselective carboxylation may be possible without large modification of the reaction protocol. For stereoselective carboxylation of benzylic substrates (**sub2**) it might be of interest to modify the reaction protocol by either additives for CO_2 activation, bulkier NHC substituents or by replacing CsF with other bases, to avoid competing CsF-mediated carboxylation.

In future investigations it might be of interest to take a closer look at the reference state of CsF. This is important for the comparison of the Cu-catalyzed (**D**) and CsF-mediated (**C**) carboxylation of benzylic (**sub2**) substrates because with the currently available results it is difficult to arrive at a clear conclusion.

3.3 Carboxylation of Ni(I)-Complexes (Paper III)

Introduction

Ni-catalyzed carboxylation reactions have received considerable attention and a wide variety of chemical protocols has been developed by various groups including Rovis,[82] Tsuji,[83,84] Martin[85] and their respective co-workers. Some of these reactions are proposed to proceed through Ni(I) species before the CO_2 insertion[86], however, with limited experimental evidence. This is likely the consequence of the low stability of these species.[87] However, in 2019 Diao and co-workers[88] reported experimental evidence for the existence of Ni(I)-alkyl species and their reaction with CO_2.

Recently, Martin and co-workers (ICIQ, Spain), as well as Hazari and co-workers (Yale, USA) set out to synthesise and isolate well-defined Ni(I)-alkyl species using phenanthroline (Phen)-based ligands. Furthermore, Martin, Hazari, and co-workers were interested in proving the reaction of these species with CO_2 and we contributed to this work through computational analysis.

The developed protocol of Martin and co-workers is schematically shown in Fig. 3.17 for the L1 ligand with bromide and consists of a comproportionation reaction to create the L1-Ni(I)-Br species $\mathbf{i_F2}$ followed by using a Grignard reactant to obtain the L1-Ni(I)-alkyl species $\mathbf{i_F3}$. My contribution to this project were the computations of the infrared (IR) spectra, spin density, and CO_2 insertion TSs, as well as sections on the computational results for the manuscript draft.
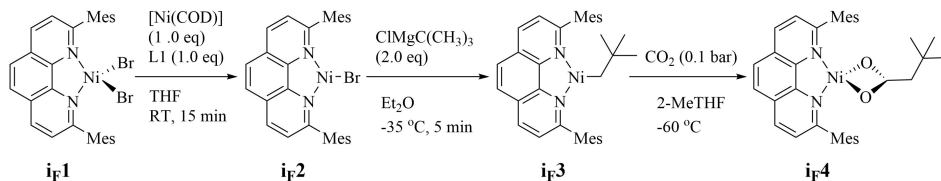
Figure 3.17: Reaction protocol of Martin and co-workers (**Paper III**) for synthesis and carboxylation of L1-Ni-neopentyl **i$_F$3**.

Computational Methods

The method of choice was DFT using the GGA functional PBE[75] and the hybrid functional B3LYP[74], both with the D3 dispersion correction[27] and the BJ damping.[76] All calculations were performed using the def2-TZVP[61] basis set with the SDD ECP for Ni.[78] Solvation effects were included using a PCM of THF.

Errors introduced by employing the harmonic approximation for vibrational mode calculations were reduced by using scaling factors for the wave numbers according to CCCBDB.[89] The scaling factors, 0.986 for PBE-D3BJ and 0.960 for B3LYP-D3BJ, were taken from the 6-31G* basis set as numbers were not available for the used basis set.

IR Spectra

For the characterisation of the L1-Ni-Br **i$_F$1** and L1-Ni-neopentyl **i$_F$3** the crystal structures were obtained by our collaborators proving the successful synthesis of these reactants. However, the thermal instability prevented the crystallization and identification for the expected carboxylation product **i$_F$4**. To help identifying if the reaction product was the desired carboxylation product **i$_F$4**, IR spectra were calculated to compare with the two available

experimental IR spectra (with and without ^{13}C-labelled CO_2) of the reaction product. The calculated and experimental IR spectra are shown in Fig. 3.18.
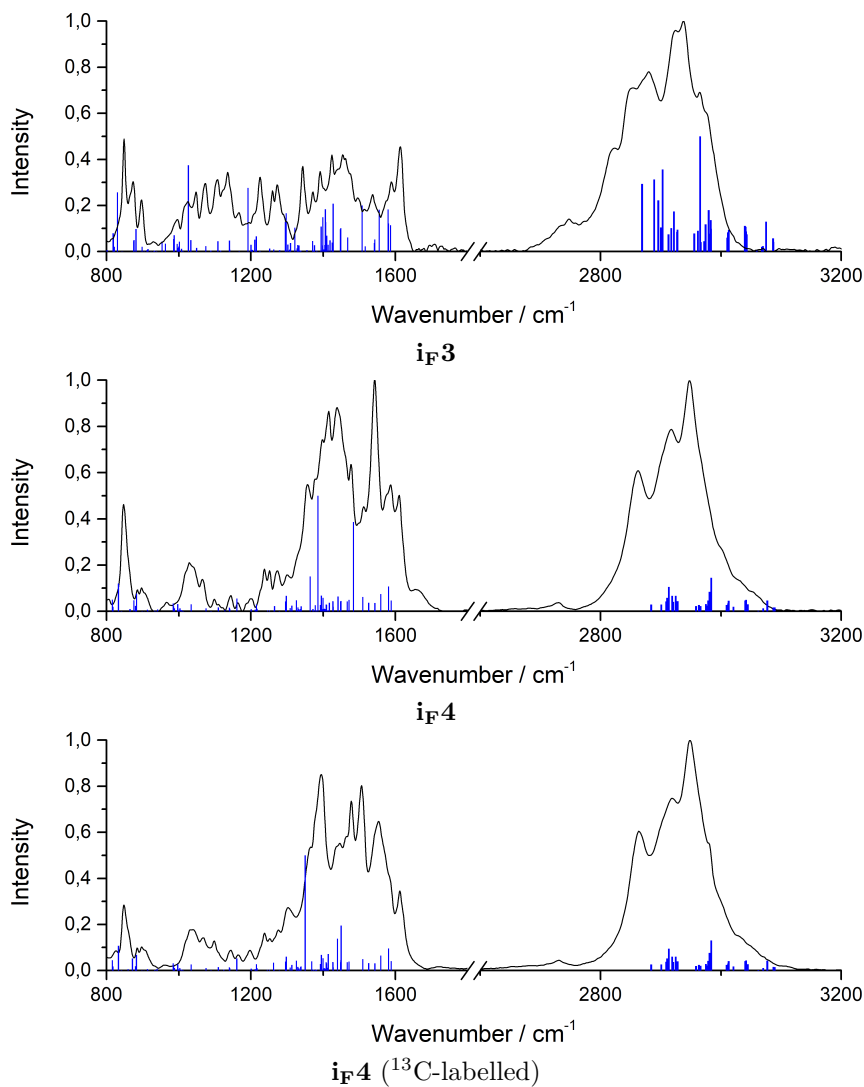
Figure 3.18: Calculated (blue) and experimental (black) IR spectra of $\mathbf{i_F 3}$ and $\mathbf{i_F 4}$, with and without ^{13}C-labelling.

In experiment without labelled CO_2, the formation of a strong band at $1543\,\mathrm{cm}^{-1}$ is observed which suggests an asymmetric C-O stretch vibration.

The calculations show a similar strong band at $1484\,cm^{-1}$ (PBE-D3BJ) and $1503\,cm^{-1}$ (B3LYP-D3BJ) and the vibrations associated with these bands are also asymmetric C-O stretches. Considering the error from the harmonic approximation and comparing the calculated spectra with the experimental ones, these results suggest that the reaction product is the desired carboxylation product **i_F4**.

This is further supported by the IR spectra with ^{13}C-labelled CO_2. In experiment, the labelling resulted in a shift of the C-O band by $38\,cm^{-1}$ towards lower wave numbers, compared with the unlabelled CO_2. Calculation predicted a very similar shift of 34 (PBE-D3BJ) and $36\,cm^{-1}$ (B3LYP-D3BJ) and thus further support the conclusion that the carboxylation of **i_F3** to synthesise **i_F4** was successful.

These results suggest that the reaction protocol is not only capable of synthesising Ni(I)-alkyl species but that these species also can be carboxylated with CO_2.

CO_2 Insertion

Additionally to calculating the IR spectra for the L1-Ni(I)-alkyl species **i_F3** and the carboxylation product **i_F4**, we investigated the CO_2 insertion mode for the carboxylation TS **TS(i_F3-i_F4)**. The inner sphere TS (with Ni-CO_2 interaction) and the outer sphere TS (without Ni-CO_2 interaction) are shown in Fig. 3.19 with their respective relative energies. The numbers suggest a strong preference for the inner sphere TS by 15.0 (PBE-D3BJ) and $13.8\,kcal/mol$ (B3LYP-D3BJ), which suggests that Ni-CO_2 interactions are crucial for carboxylation of Phen-Ni(I)-alkyl species.

Inner sphere TS (7.7 kcal/mol)   Outer sphere TS (22.7 kcal/mol)
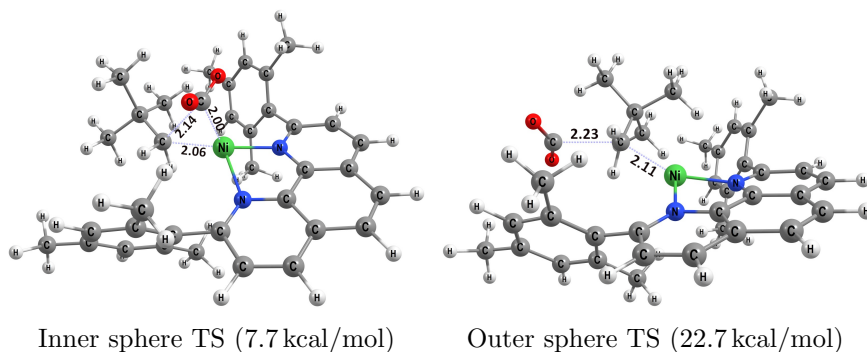
Figure 3.19: Structures and energies (relative to i_F3 and free CO_2) of the CO_2 insertion TSs based on the PBE-D3BJ calculations. Bond lengths are in Å.

Similar results were obtained by computing the CO_2 insertion TSs of a modified i_F3 which has a methyl group instead of the neopentyl group. The structures and energies for these TSs are shown in Fig. 3.20 and the results again indicate a strong preference for the inner sphere TS by 6.6 kcal/mol (PBE-D3BJ).

Inner sphere TS (8.5 kcal/mol)   Outer sphere TS (15.1 kcal/mol)
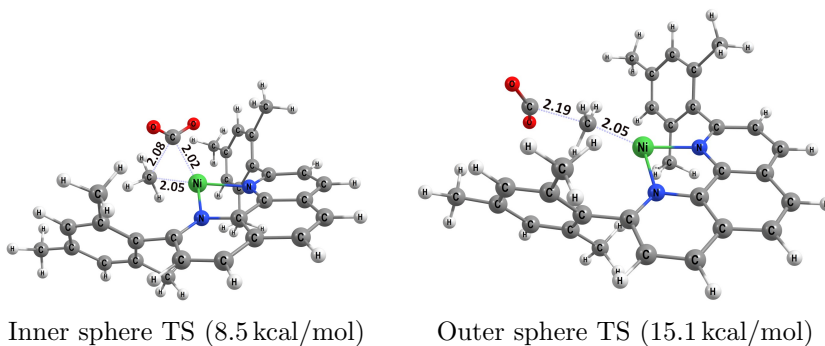
Figure 3.20: Structures and energies (relative to L1-Ni-Me and free CO_2) of the CO_2 insertion TSs based on the PBE-D3BJ calculations. Bond lengths are in Å.

The calculated energies of the CO_2 insertion into Phen-Ni(I)-alkyl species suggest strong Ni-CO_2 interactions, which indicates Phen-Ni(I) complexes

are capable of activating CO_2.

Comparison with Xantphos Ligands

As part of the work currently performed in our group we compared the CO_2 insertion of the L1-Ni(I)-alkyl complex by Martin and co-workers (**Paper III**) with the *t*Bu-Xantphos-Ni(I)-alkyl complex by Diao and co-workers.[88] This comparison is of interest as both ligand are very different and possible give more insight into the effect of ligands.

These calculations were performed with the ωB97XD and B3LYP-D3BJ functionals, with the 6-31++g(d,p) basis set,[51–60] the SDD ECP for Ni[78] and a PCM for THF. The resulting energies for the inner and outer sphere TSs for L1-Ni(I)-Me and *t*Bu-Xantphos-Ni(I)-Me complex are listed in Table 3.4.

Table 3.4: All computed energies for the inner and outer sphere TSs for the L1-Ni(I)-Me and *t*Bu-Xantphos-Ni(I)-Me complexes. Energies are relative to the Ni(I)-Me complex and a free CO_2 molecule.

Ni(I) complex	B3LYP-D3BJ		ωB97XD	
	Inner sph.	Outer sph.	Inner sph.	Outer sph.
L1-Ni(I)-Me	7.1	16.3	8.9	18.2
Xantphos-Ni(I)-Me	0.0*	1.5*	18.4	19.3

*Energies relative to inner sphere TS

For *t*Bu-Xantphos-Ni(I)-Me, the inner sphere TSs are only 1.5 (B3LYP-D3BJ) and 0.9 kcal/mol (ωB97XD) lower than the outer sphere TSs. This is a significant difference from L1-Ni(I)-Me with a preference of 9.3 kcal/mol (B3LYP-D3BJ and ωB97XD) for the inner sphere TSs. Thus, the comparison shows an interesting trend where the preference for inner sphere CO_2

insertion over outer sphere insertion remains but the barrier differences significantly decrease.

These numbers are preliminary results but suggest that Xantphos ligands leads to much weaker CO_2 activation to the point where inner and outer sphere CO_2 insertion mechanisms become equally likely.

Conclusion

From the computations of the IR spectra and the CO_2 insertion TSs for L1-Ni(I)-alkyl species, two conclusions can be drawn: First, the product of the carboxylation reaction is very likely the desired product, as can be concluded from the position and shift of the C-O bands. Second, a Ni-CO_2 interaction is crucial for the carboxylation step for Phen-Ni(I)-alkyl species based on the strong preferences for inner sphere TSs.

Preliminary results for the carboxylation of a Xantphos-Ni(I)-Me species suggest that the use of Xantphos ligands significantly reduces the activation of CO_2 by Ni(I). More calculations are needed to confirm this trend but it might indicate that Xantphos ligands are not an optimal choice for CO_2 insertion reactions.

Chapter 4

Conclusion and Future Work

In this thesis the findings of **Paper I-IV** were presented and discussed. The results were obtained using the methods of computational chemistry and working in cooperation with experimental chemists to validate computational findings by comparing them with the experimental results. The goal of this combined approach was to achieve a more comprehensive understanding of reaction mechanisms and the factors influencing them.

A total of six reaction mechanisms were, in part or in their entirety, optimized employing a total of five different substrates. The investigated reactions were carboxylations with CO_2 employing the metals caesium, copper, or nickel and we were especially interested in the importance of metal-CO_2 interactions during the formation of a new C-C bond.

Homogeneous Catalysis with DFT

These computational investigations employed DFT with the ωB97XD, PBE-D3BJ, and B3LYP-D3BJ functionals for energies and geometries, as well as

the DLPNO-CCSD(T) method for *ab initio* electronic energies. Additional new methods such as MC-AFIR, which could be used to automate the TS search, were tested.

The calculations showed that different DFT functionals yielded somewhat different results. For example, ωB97XD was the only employed functional capable of identifying **TS(i_C1-i_C2)**, the TS of breaking the C-B bond for the CsF-mediated carboxylation. It is not evident if this an error of the ωB97 family or of the other used functionals, but it should be considered that many DFT functionals tend to have problems with the description of loosely bound electrons and long-range interactions, which could explain this behaviour.[24] Furthermore, the ωB97XD (and DLPNO-CCSD(T))-based rate-limiting barriers are considerably higher than those based on PBE-D3BJ or B3LYP-D3BJ, however, it is known that "classical" functionals often overestimate the stability of TSs, leading to a underestimation of the reaction barriers.[24] However, the DFT and the DLPNO-CCSD(T) results were able to predict the correct reactivity trends for Cu and CsF-mediated reactions. Similarly, the DFT-based IR spectra of Ni-alkyl species could reasonably reproduce the experimental spectra within the error of the harmonic approximation.

The solvation of CsF in dioxane was a major concern for the work, as the structure of CsF in 1,4-dioxane is not known. Therefore, we had to make assumptions and used two different CsF reference states. The choice of CsF reference state has influence on the comparison of the competing Cu- and CsF-mediated carboxylation and was discussed. Furthermore, the effect of one explicit solvent molecule at the caesium ion was calculated and it was found that this has no influence on the mechanistic conclusions.

Cs-, Cu-, and Ni-Mediated Carboxylation

For CsF-mediated carboxylations, we could identify a reaction mechanism capable to reproduce the experimentally observed substrate preference (**Paper I**). The calculations indicate that the ability of a substrate to stabilize a negative charge via delocalization, and the formation of Cs-π-electron interactions are crucial parts of this selectivity.

The results for the Cu-catalyzed carboxylation based on the protocol of Skrydstrup, Nielsen and co-workers[46], presented in **Paper II**, suggest that alkylic and benzylic organoboranes can be carboxylated by a Cu-IPr complex and that for benzylic organoboranes the Cu-catalyzed carboxylation is either much faster or at least as fast as the CsF-mediated carboxylation. The exact barrier differences between the Cu-catalyzed and the CsF-mediated carboxylation is dependent on the used computational method but also on how the solvation and the reference state for CsF are chosen.

Calculation on Phen-Ni(I)-alkyl species and their carboxylation products (**Paper III**) indicate that Ni(I) is capable of activating CO_2 during CO_2 insertion for alkylic substrates (methyl and neopentyl). Furthermore, calculated IR spectra were used for the characterisation of the carboxylation product and helped to identify these thermally unstable species. These conclusions were based on the relative position and intensity of a C-O band as well as the shift of this band if ^{13}C-labelled CO_2 was used.

Stability of Organometallic Intermediates

Before the CO_2 insertion via C-C bond formation, organometallic intermediates are formed and these show significant differences between the in-

vestigated metals. The organometallic intermediates of Cu and Ni feature strong metal-carbon bonds, while for Cs, these bonds are weak. This has two consequences: *i)* For Cu and Ni, the intermediates are conformationally more stable, and *ii)* they do not need additional stabilizing effects such as charge delocalization or metal-π-electron interactions to be stable. This stability allows Cu- and Ni-based organometallic intermediates to better preserve steric informations such as the stereochemical conformation at the nucleophilic center. In the case of CsF, the relatively low stability of the organocaesium intermediate is likely the reason for the non-reactivity of non-benzylic substrates.

Metal-CO_2 Interactions

For the metal-CO_2 interactions during the CO_2 insertion, we observed that for organocaesium species (CsF-mediated carboxylations) these interactions are of minor importance. Energy differences between inner and outer sphere TSs were relatively small and steric effects can be more important in comparison.

For Cu-IPr and Ni(I)-Phen-catalyzed carboxylations with alkyl substrates, the metal-CO_2 interactions are crucial, as it is shown by the inner sphere TSs being much lower in energy than the outer sphere TSs. This indicates that for C-C bond formation with non-benzylic C_{sp^3} carbons the CO_2 experiences a strong activation from the metal center. However, preliminary results suggest that in the case of Ni this trend can be changed if Xantphos ligands are used instead of Phen ligands, which greatly weakens the Ni-CO_2 interactions.

Substrates with benzylic C_{sp^3} carbons showed only minor metal-CO_2

interactions compared with non-benzylic substrates as indicated by the small energy differences between inner and outer sphere TSs, for the CsF-mediated and Cu-catalyzed carboxylation reactions. Therefore, the results suggest that C-C bond formations with benzylic C_{sp^3} carbons are much less dependent on an activation of CO_2 by the metal center. Consequently, the inclusion of Lewis acids for CO_2 activation might be a promising approach to increase reaction rates for benzylic substrates.

Evaluation of the Performed Work Relative to the Aims

The thesis has three explicit aims: *i)* Investigation of possible reaction mechanisms and identification of the preferred pathways, *ii)* Investigation of the mode of CO_2 insertion and importance of metal-CO_2 interactions, and *iii)* Testing of recent computational methods for the investigation of reaction mechanisms.

Concerning *i)*, five full reaction mechanisms for CsF-mediated and Cu-catalyzed carboxylation of organoboranes were investigated and amongst these two mechanism (**C** and **D**) were found to give accessible barriers at the reaction temperature of 393 K. For *ii)* the CO_2 insertion TSs for three organocaesium, two organocopper and three organonickel species were optimized and compared in this thesis with the results being summed up above in the previous section. Aim *iii)* was tackled by testing the AFIR method, which was used to automate the search of TSs, and the relatively new DLPNO(-CCSD(T)) method, used to calculate *ab initio* electronic energies and which will hopefully become a standard method in our group.

Future Work

For future work several topics are of interest to obtain a better understanding of carboxylation reactions. First, for Cu(I) complexes the effect of different ligands (such as diphosphine ligands) or substituents could help to understand their influence on Cu-CO_2 interactions or rate-limiting barriers for electronically different substrates. Furthermore, the use of chiral ligands is an interesting prospect for the development of enantioselective protocols. Second, as the preliminary results indicate, the choice of ligand for Ni(I)-catalyzed carboxylation is important and a promising subject considering its effect on the activation of CO_2 during the reaction. Third, it might be fruitful to investigate possible reactions with additives similar to CsF, with their carboxylation mechanisms. This is important to test additives for the design of potentially enantioselective reactions.

Bibliography

[1] M. Mikkelsen, M. Jørgensen, F. C. Krebs, *Energy Environ. Sci.* **2010**, *3*, 43–81.

[2] J. A. Raven, P. G. Falkowski, *Plant Cell Environ.* **1999**, *22*, 741–755.

[3] I. Andersson, A. Backlund, *Plant Physiol. Biochem.* **2008**, *46*, 275–91.

[4] M. Jones, Wikipedia Commons, `https://commons.wikimedia.org/wiki/File:Calvin-cycle3.png` (visited on 06/23/2020).

[5] C.-H. Huang, C.-S. Tan, *Aerosol Air Qual. Res.* **2014**, *14*, 480–499.

[6] Q. Liu, L. Wu, R. Jackstell, M. Beller, *Nat. Commun.* **2015**, *6*, 5933.

[7] M. D. Burkart, N. Hazari, C. L. Tway, E. L. Zeitler, *ACS Catal.* **2019**, *9*, 7937–7956.

[8] M. Cokoja, C. Bruckmeier, B. Rieger, W. A. Herrmann, F. E. Kuhn, *Angew. Chem. Int. Ed. Engl.* **2011**, *50*, 8510–37.

[9] G. A. Olah, G. K. S. Prakash, A. Goeppert, *J. Am. Chem. Soc.* **2011**, *133*, PMID: 21612273, 12881–12898.

[10] M. Muntean, D. Guizzardi, E. Schaaf, M. Crippa, E. Solazzo, et al., Fossil CO2 emissions of all world countries - 2018 Report, Report, Publications Office of the European Union, **2018**.

[11] A. Scott, *C&EN* **2015**, *93*, 10–16.

[12] "Trends in Atmospheric Carbon Dioxide", Earth System Research Laboratory (NOAA), `https://www.esrl.noaa.gov/gmd/ccgg/trends/global.html#global` (visited on 06/29/2020).

[13] D. S. Strebkov, *Front. Agr. Sci. Eng.* **2015**, *2*.

[14] M. Aresta, A. Dibenedetto, A. Angelini, *Chem. Rev.* **2014**, *114*, 1709–42.

[15] M. Aresta, A. Dibenedetto, E. Quaranta, *J. Catal.* **2016**, *343*, 2–45.

[16] A. Tortajada, F. Julia-Hernandez, M. Borjesson, T. Moragas, R. Martin, *Angew. Chem. Int. Ed. Engl.* **2018**, *57*, 15948–15982.

[17] P. Atkins, J. de Paula, *Atkins' Physical Chemistry*, OUP Oxford, **2010**.

[18] T. Kandemir, M. E. Schuster, A. Senyshyn, M. Behrens, R. Schlogl, *Angew. Chem. Int. Ed. Engl.* **2013**, *52*, 12723–6.

[19] A. P. H. Wilhelm, Process of catalytic cracking of petroleum hydrocarbons, US Patent 2,423,674, **1947**.

[20] H. Yamada, T. Ueoka, A. Takami, N. Sakatani, Hydrocarbon adsorbent for exhaust gas cleaning, exhaust gas cleaning catalyst and exhaust gas cleaning device, US Patent 5,744,103, **1998**.

[21] J. Fujii, K. Suzuki, K. Kimura, Catalyst for cleaning exhaust gas with alumina, ceria, zirconia, nickel oxide, alkaline earth oxide, and noble metal catalyst, and method for preparing, US Patent 5,492,878, **1996**.

[22] V. Savchenko, I. Makaryan, *Platin. Met. Rev.* **1999**, *43*, 74–82.

[23] H. Ryu, J. Park, H. K. Kim, J. Y. Park, S.-T. Kim, et al., *Organometallics* **2018**, *37*, 3228–3239.

[24] F. Jensen, *Introduction to Computational Chemistry*, John Wiley & Sons Ltd, **2007**.

[25] P. Hohenberg, W. Kohn, *Phys. Rev.* **1964**, *136*, B864–B871.

[26] W. Kohn, L. J. Sham, *Phys. Rev.* **1965**, *140*, A1133–A1138.

[27] S. Grimme, J. Antony, S. Ehrlich, H. Krieg, *J. Chem. Phys.* **2010**, *132*, 154104.

[28] P. Pulay, *Chem. Phys. Lett.* **1983**, *100*, 151–154.

[29] S. Sæbø, P. Pulay, *Chem. Phys. Lett.* **1985**, *113*, 13–18.

[30] C. Riplinger, F. Neese, *J. Chem. Phys.* **2013**, *138*, 034106.

[31] C. Riplinger, B. Sandhoefer, A. Hansen, F. Neese, *J. Chem. Phys.* **2013**, *139*, 134101.

[32] P. Rosmus, W. Meyer, *J. Chem. Phys.* **1978**, *69*.

[33] W. Meyer, *Int. J. Quantum Chem.* **2009**, *5*, 341–348.

[34] R. Ahlrichs, F. Driessler, H. Lischka, V. Staemmler, W. Kutzelnigg, *J. Chem. Phys.* **1975**, *62*, 1235–1247.

[35] P. R. Taylor, G. B. Bacskay, N. S. Hush, A. C. Hurley, *Chem. Phys. Lett.* **1976**, *41*, 444–449.

[36] F. Neese, *WIREs Comput. Mol. Sci.* **2012**, *2*, 73–78.

[37] F. Neese, *WIREs Comput. Mol. Sci.* **2017**, *8*.

[38] E. v. Lenthe, E. J. Baerends, J. G. Snijders, *J. Chem. Phys.* **1993**, *99*, 4597–4610.

[39] E. van Lenthe, E. J. Baerends, J. G. Snijders, *J. Chem. Phys.* **1994**, *101*, 9783–9792.

[40]   S. Maeda, K. Morokuma, *J. Chem. Theory Comput.* **2011**, *7*, 2335–45.

[41]   S. Maeda, K. Ohno, K. Morokuma, *Phys. Chem. Chem. Phys.* **2013**, *15*, 3683–701.

[42]   S. Maeda, Y. Harabuchi, M. Takagi, K. Saita, K. Suzuki, et al., *J. Comput. Chem.* **2018**, *39*, 233–251.

[43]   S. Maeda, Y. Harabuchi, M. Takagi, T. Taketsugu, K. Morokuma, *Chem. Rec.* **2016**, *16*, 2232–2248.

[44]   S. Miertuš, E. Scrocco, J. Tomasi, *Chem. Phys.* **1981**, *55*, 117–129.

[45]   S. Miertuš, J. Tomasi, *Chem. Phys.* **1982**, *65*, 239–245.

[46]   M. Juhl, S. L. R. Laursen, Y. Huang, D. U. Nielsen, K. Daasbjerg, et al., *ACS Catal.* **2017**, *7*, 1392–1396.

[47]   J. D. Chai, M. Head-Gordon, *Phys. Chem. Chem. Phys.* **2008**, *10*, 6615–6620.

[48]   L. Goerigk, A. Hansen, C. Bauer, S. Ehrlich, A. Najibi, et al., *Phys. Chem. Chem. Phys.* **2017**, *19*, 32184–32215.

[49]   N. Mardirossian, M. Head-Gordon, *Mol. Phys.* **2017**, *115*, 2315–2372.

[50]   C. van Wüllen, *J. Chem. Phys.* **1998**, *109*, 392–399.

[51]   R. C. Binning, L. A. Curtiss, *J. Comp. Chem.* **1990**, *11*, 1206–1216.

[52]   J.-P. Blaudeau, M. P. McGrath, L. A. Curtiss, L. Radom, *J. Chem. Phys.* **1997**, *107*, 5016–5021.

[53]   R. Ditchfield, W. J. Hehre, J. A. Pople, *J. Chem. Phys.* **1971**, *54*, 724–728.

[54] M. M. Francl, W. J. Pietro, W. J. Hehre, J. S. Binkley, M. S. Gordon, et al., *J. Chem. Phys.* **1982**, *77*, 3654–3665.

[55] M. S. Gordon, *Chem. Phys. Lett.* **1980**, *76*, 163–168.

[56] P. C. Hariharan, J. A. Pople, *Theor. Chem. Acc.* **1973**, *28*, 213–222.

[57] P. C. Hariharan, J. A. Pople, *Mol. Phys.* **2006**, *27*, 209–214.

[58] W. J. Hehre, R. Ditchfield, J. A. Pople, *J. Chem. Phys.* **1972**, *56*, 2257–2261.

[59] T. Clark, J. Chandrasekhar, G. W. Spitznagel, P. V. R. Schleyer, *J. Comp. Chem.* **1983**, *4*, 294–301.

[60] M. J. Frisch, J. A. Pople, J. S. Binkley, *J. Chem. Phys.* **1984**, *80*, 3265–3269.

[61] F. Weigend, R. Ahlrichs, *Phys. Chem. Chem. Phys.* **2005**, *7*, 3297–305.

[62] L. von Szentpály, P. Fuentealba, H. Preuss, H. Stoll, *Chem. Phys. Lett.* **1982**, *93*, 555–559.

[63] D. A. Pantazis, X. Y. Chen, C. R. Landis, F. Neese, *J. Chem. Theory Comput.* **2008**, *4*, 908–19.

[64] M. J. Frisch, G. W. Trucks, H. B. Schlegel, G. E. Scuseria, M. A. Robb, et al., Gaussian 16 Revision B.01, Gaussian Inc. Wallingford CT 2016.

[65] S. Maeda, K. Morokuma, *J. Chem. Phys.* **2010**, *132*, 241102.

[66] S. Maeda, K. Morokuma, *J. Chem. Theory Comput.* **2011**, *7*, 2335–45.

[67] M. J. Frisch, G. W. Trucks, H. B. Schlegel, G. E. Scuseria, M. A. Robb, et al., Gaussian 09 Revision D.01, Gaussian Inc. Wallingford CT 2009.

[68]   T. Husch, L. Freitag, M. Reiher, *J. Chem. Theory Comput.* **2018**, *14*, 2456–2468.

[69]   R. Kuniyil, F. Maseras, *Theor. Chem. Acc.* **2017**, *136*.

[70]   J. E. Heimann, W. H. Bernskoetter, N. Hazari, *J. Am. Chem. Soc.* **2019**, *141*, 10520–10529.

[71]   J. E. Heimann, W. H. Bernskoetter, N. Hazari, J. M. Mayer, *Chem. Sci.* **2018**, *9*, 6629–6638.

[72]   T. Ohishi, L. Zhang, M. Nishiura, Z. Hou, *Angew. Chem. Int. Ed. Engl.* **2011**, *50*, 8114–7.

[73]   H. Ohmiya, M. Tanabe, M. Sawamura, *Org. Lett.* **2011**, *13*, 1086–8.

[74]   A. D. Becke, *J. Chem. Phys.* **1993**, *98*, 5648–5652.

[75]   J. P. Perdew, K. Burke, M. Ernzerhof, *Phys. Rev. Lett.* **1996**, *77*, 3865–3868.

[76]   S. Grimme, S. Ehrlich, L. Goerigk, *J. Comput. Chem.* **2011**, *32*, 1456–65.

[77]   H. Stoll, P. Fuentealba, P. Schwerdtfeger, J. Flad, L. v. Szentpály, et al., *J. Chem. Phys.* **1984**, *81*, 2732–2736.

[78]   M. Dolg, U. Wedig, H. Stoll, H. Preuss, *J. Chem. Phys.* **1987**, *86*, 866–872.

[79]   W. Leitner, *Coord. Chem. Rev.* **1996**, *153*, 257–284.

[80]   X. Lv, Y.-B. Wu, G. Lu, *Catal. Sci. Technol.* **2017**, *7*, 5049–5054.

[81]   D. García-López, L. Pavlovic, K. H. Hopmann, *Organometallics* **2020**, *39*, 1339–1347.

[82] C. M. Williams, J. B. Johnson, T. Rovis, *J. Am. Chem. Soc.* **2008**, *130*, 14936–7.

[83] T. Fujihara, K. Nogi, T. Xu, J. Terao, Y. Tsuji, *J. Am. Chem. Soc.* **2012**, *134*, 9106–9.

[84] K. Nogi, T. Fujihara, J. Terao, Y. Tsuji, *J. Org. Chem.* **2015**, *80*, 11618–23.

[85] Y. Liu, J. Cornella, R. Martin, *J. Am. Chem. Soc.* **2014**, *136*, 11212–5.

[86] F. B. Sayyed, S. Sakaki, *Chem. Commun. (Camb.)* **2014**, *50*, 13026–9.

[87] M. Mohadjer Beromi, G. W. Brudvig, N. Hazari, H. M. C. Lant, B. Q. Mercado, *Angew. Chem.* **2019**, *131*, 6155–6159.

[88] J. B. Diccianni, C. T. Hu, T. Diao, *Angew. Chem. Int. Ed. Engl.* **2019**, *58*, 13865–13868.

[89] Computational Chemistry Comparison and Benchmark DataBase, National Institute of Standards and Technology (NIST), `https : / / cccbdb.nist.gov/vibscalejust.asp` (visited on 06/15/2020).

Paper I

Caesium Fluoride-mediated Hydrocarboxylation of Alkenes and Allenes: Scope and Mechanistic Insights

A. Gevorgyan, M. Obst, Y. Guttormsen
F. Maseras, K. H. Hopmann and A. Bayer

Supporting Information and

a .XYZ file can be found under:

https://dx.doi.org/10.1039/C9SC02467K

Check for updates

Caesium fluoride-mediated hydrocarboxylation of alkenes and allenes: scope and mechanistic insights†

Ashot Gevorgyan, [ID] ‡[a] Marc F. Obst, [ID] ‡[b] Yngve Guttormsen,[a] Feliu Maseras, [ID] [c] Kathrin H. Hopmann [ID] *[b] and Annette Bayer [ID] *[a]

A caesium fluoride-mediated hydrocarboxylation of olefins is disclosed that does not rely on precious transition metal catalysts and ligands. The reaction occurs at atmospheric pressures of CO_2 in the presence of 9-BBN as a stoichiometric reductant. Stilbenes, β-substituted styrenes and allenes could be carboxylated in good yields. The developed methodology can be used for preparation of commercial drugs as well as for gram scale hydrocarboxylation. Computational studies indicate that the reaction occurs *via* formation of an organocaesium intermediate.

Introduction

CO_2 provides a sustainable source of carbon that increasingly is being used in chemical synthesis.[1] Construction of anthropogenic chemical carbon cycles[2] by valorisation of CO_2 into chemicals, materials, and fuels, is a promising strategy for replacing fossil carbon in the chemical industry.[1,3] Various studies have shown that transition metal-based catalysts are able to selectively reduce CO_2 into simple chemicals, such as formic acid, methanol, alkanes, and CO.[3a] CO_2 can also be incorporated into carbonates, which are valuable starting materials for polymer science.[3b] Use of CO_2 in C–C bond forming reactions opens new pathways towards value-added products and pharmaceuticals from CO_2.[4]

As part of our research interest to develop C–CO_2 bond forming reactions,[5] we became interested in the copper-catalysed hydrocarboxylation reactions reported by Hou,[6a] Sawamura[6b] and Skrydstrup[6c] (Scheme 1A). In these formal hydrocarboxylations, an initial hydroboration with 9-borabicyclo[3.3.1]nonane (9-BBN) transforms an alkene to an organoborane, which in a subsequent copper-catalysed step is carboxylated with CO_2. In order to elucidate the mechanistic details of the carboxylation step, we embarked on a computational study of the reaction. Surprisingly, our

computational analysis indicated the existence of a feasible carboxylation pathway that does not involve the copper complex. Our subsequent experiments confirmed that it is possible to carboxylate *in situ* formed organoboranes in absence of copper. Related reports of carboxylations with CO_2 in absence of transition metals include fluoride-mediated carboxylations of organosilanes[7b–f] and KO*t*Bu-mediated carboxylations of benzylboronic esters (Scheme 1B).[7a] However, none of these reports addressed a possible role of the counterion for the observed reactivity. To the best of our knowledge, a CsF-mediated hydrocarboxylation with *in situ* generated organoboranes has not been reported. In the following, we detail our findings of the CsF-mediated hydrocarboxylation of alkenes with CO_2 (Scheme 1C). A detailed computational analysis indicates that the reaction proceeds *via* formation of organocaesium intermediates. The described transformation expands the repertoire of carboxylation

[a]Department of Chemistry, UiT The Arctic University of Norway, Norway. E-mail: annette.bayer@uit.no

[b]Hylleraas Centre for Quantum Molecular Sciences, Department of Chemistry, UiT The Arctic University of Norway, Norway. E-mail: kathrin.hopmann@uit.no

[c]Institute of Chemical Research of Catalonia (ICIQ), Spain

† Electronic supplementary information (ESI) available. See DOI: 10.1039/c9sc02467k

‡ These authors contributed equally.

Scheme 1 Previous works (A[6] and B[7]) and present study (C).

reactions that can be performed without the use of transition metal catalysts.

Results and discussion

On basis of a preliminary computational investigation of the hydrocarboxylation of alkenes, we speculated that *trans*-stilbene **1a** can be hydrocarboxylated *via* an organoborane intermediate in the absence of a transition metal catalyst, which is in contrast to previous reports.[6] To test our hypothesis, we used 9-BBN in dioxane to convert **1a** into an organoborane intermediate, which we attempted to carboxylate with CO_2 in a CsF-mediated transformation (Table 1). Gratifyingly, the corresponding carboxylic acid **2a** was obtained in 83% yield (Table 1, entry 2). In comparison, the previously reported copper-catalysed reaction[6c] gave the carboxylation product **2a** in 78% yield (Table 1, entry 1). The higher yield in absence of copper was observed for several substrates (ESI, Scheme S1 and S2†). This phenomenon may be explained by a copper-promoted decarboxylation reaction slowly consuming the product **2a**.[8] To support this hypothesis, we mixed 2-phenylpropionic acid with the Cu complex under reaction conditions, which lead us to recover only 95% of the starting acid, while in the absence of Cu, the recovery of acid was 99% (ESI, Scheme S1†).

We proceeded to establish the optimum reaction conditions of the base-mediated carboxylation reaction. Screening of

different solvents revealed that the reaction works well in ethers. The best yield was observed in dimethoxyethane (DME, 87%, Table 1, entry 5). The screening of different bases indicated that the optimal base is CsF (87% yield; Table 1, entry 5), while other fluoride containing bases like KF and NaF gave inferior results (50% and 0% yield, entry 9 and 10). Interestingly, also Cs_2CO_3 and K_2CO_3 gave good results (71% and 67% yield, entry 11 and 12), showing that not only the fluoride anion is important for the outcome of the reaction. On basis of the reports by Hou,[6a] Sawamura[6b] and Schomaker,[7a] we also attempted to employ alkoxides as base, but observed difficulties in our system. If mixed simultaneously, the reaction between alkoxide and CO_2 lead to the corresponding carbonates, and no carboxylation product was formed. Alkoxide bases were effective only if the second reaction step was run without CO_2 for minimum 30 minutes at 20 °C, followed by addition of CO_2, which provided a yield of 47% (Table 1, entry 13). Further screening related to the stoichiometry of reagents, duration of the reaction, and temperature showed that the best conditions are 1 equiv. olefin and (9-BBN)$_2$ and 3 equiv. CsF in DME at 120 °C for 24 h (Table 1, entry 5; for further details see ESI, Table S1†).
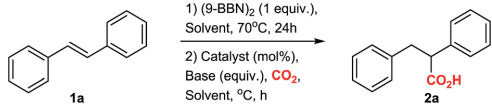
With the optimized conditions at hand, we explored the substrate scope of the reaction (Scheme 2; ESI Scheme S3†). Screening of different substrates showed that the CsF-mediated hydrocarboxylation works only on systems where the *in situ* hydroboration step (mediated by 9-BBN) generates benzylic or allylic borane intermediates. Indeed, styrene and cyclohexene were not reactive under optimal conditions (ESI Table S1†). On the other hand, stilbenes, β-substituted styrenes and allenes were successful substrates. Neither the pinacol ester of benzylboronic acid nor *in situ*-generated benzylic catechol esters (instead of the organoborane intermediate) were reactive in the CsF-mediated carboxylation (ESI Scheme S4†).

The CsF-mediated hydrocarboxylation of stilbene derivatives (**1a–e**) produced the corresponding carboxylic acids **2a–e** with moderate to excellent yields (Scheme 2A). The conversion of (*E*)-α-methyl stilbenes (**1d, 1e**) was regioselective, providing exclusive carboxylation at the sterically less hindered β-position and resulting in formation of **2d** and **2e**, each as a mixture of diastereomers. The observed regioselectivity is assumed to be controlled by steric effects.[6,9,10]

The CsF-mediated hydrocarboxylation of β-substituted styrenes (**1f–l**) gave the α-carboxylated products **3a–g** as the sole product in moderate to good yields (Scheme 2B). Interestingly, whereas the selectivity of the 9-BBN-initiated hydroboration of β-substituted styrenes is substrate-dependent and generally gives a non-regioselective mixture of boranes,[6,9,10] our base-initiated carboxylation appears to convert only the benzylic boranes, providing a single carboxylation product with excellent regioselectivity for **3a–g** (Scheme 2B). In contrast, the Cu-catalysed hydrocarboxylation does not differentiate between the regioisomeric borane intermediates, giving a mixture of carboxylic acids.[6c] For example, in the copper-catalysed hydrocarboxylation of indene (**1k**), we observed a mixture of α- and β-regioisomers with a ratio of 4 : 1 (ESI, Scheme S2†).

Allenes also proved to be suitable substrates for CsF-mediated hydrocarboxylation (Scheme 2C). Both aliphatic and

Table 1 Optimization of reaction conditions[a]

Entry	Catalyst (mol%)	Base (equiv.)	Solvent	°C/h	[b]Yield %
1	IPrCuI(5)[c]	CsF(3)	Dioxane	120/24	78
2	—	CsF(3)	Dioxane	120/24	83
3	—	CsF(3)	THF	120/24	61
4	—	CsF(3)	Diglyme	120/24	67
5	—	CsF(3)	DME	120/24	87
6	—	CsF(3)	DMA	120/24	0
7	—	CsF(3)	Toluene	120/24	70
8	—	CsF(3)	MeCN	120/24	0
9	—	KF(3)	DME	120/24	50
10	—	NaF(3)	DME	120/24	0
11	—	Cs_2CO_3(3)	DME	120/24	71
12	—	K_2CO_3(3)	DME	120/24	67
13	—	KOtBu(3)[d]	DME	120/24	47
14	—	CsF(2)	DME	120/24	57
15	—	CsF(3)	DME	80/24	59
16	—	CsF(3)	DME	120/28	85

[a] Reaction conditions: (1) **1a** (0.444 mmol), (9-BBN)$_2$ (1 equiv.), solvent (3 mL), 70 °C, 24 h. (2) (IPrCuI (5 mol%)), base (2–3 equiv.), CO_2 120 mL, 80–120 °C, 24–28 h. [b] Isolated yields. [c] The active catalyst was prepared *in situ* (IPr = 1,3-bis(2,6-diisopropylphenyl)imidazol-2-ylidene). [d] The reaction mixture was run at 20 °C for 30 min before addition of CO_2.
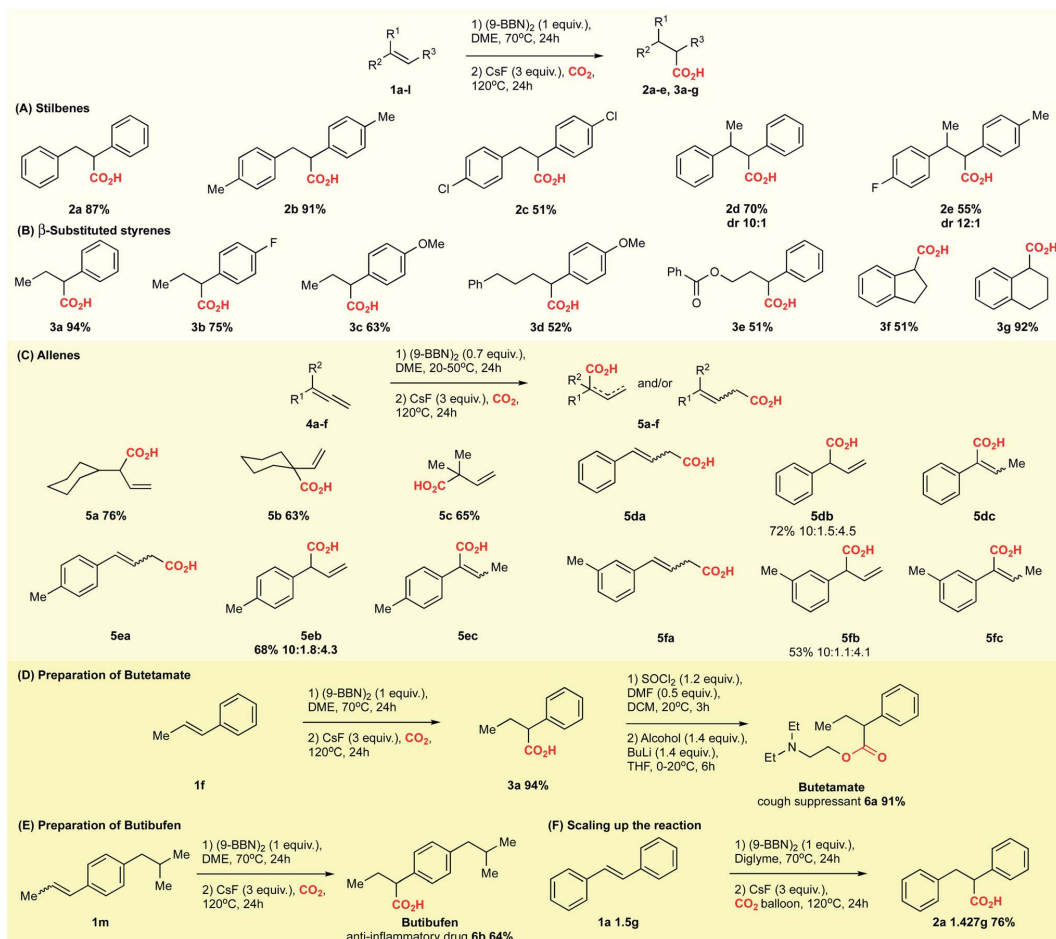
Scheme 2 Substrate scope of the CsF-mediated hydrocarboxylation.

aromatic allenes could be transformed to carboxylic acids **5a–f** with good yields. The regioselectivity of the reaction was strongly dependent on the nature of the allene substituents. Allenes with aliphatic substituents gave the internal allylic carboxylic acid as a single product **5a–c** (Scheme 2C). In contrast, allenes possessing aromatic substituents yielded the carboxylic acids **5d–f** as isomeric mixtures, with the terminal carboxylic acids as the major product (Scheme 2C). Although borane-mediated hydroboration of allenes has been described,[11] the selectivity is not well understood, and equilibria of internal and terminal allylic boranes have been proposed. Recently, Chida and Sato showed that the hydroboration of allenes in deuterated THF occurs predominantly at the terminal double bond.[11f] Carboxylation of alkyl allenes may then proceed from the terminal allylic borane with an allyl shift, or involve the internal allylic borane generated through equilibration. For aryl

allenes, the direct carboxylation of the terminal allylic borane is preferred as the system is less likely to rearrange due to conjugation.

We further tested the possibility of asymmetric hydrocarboxylation using the (−)-isopinocampheylborane TMEDA complex – a chiral analogue of 9-BBN – in the initial hydroboration step (ESI Scheme S5†).[12] Even though the hydroboration–oxidation of *trans*-β-methylstyrene gave the corresponding alcohol with 36% *ee* (ESI, Scheme S5A†), the hydroboration–carboxylation using our conditions led to racemic product (ESI, Scheme S5B†). The observed racemisation may be explained by the structural instability of intermediate organometallic compounds, such as the organoborane or an organocaesium (*vide infra*) at elevated temperatures.[13]

In order to show the versatility of the developed CsF-mediated hydrocarboxylation reaction, we applied our strategy in the synthesis of the commercial drugs butetamate **6a** and butibufen **6b** from β-substituted styrenes (Scheme 2D and E). Although in case of butetamate, four steps are required (hydroboration, carboxylation, preparation of acid anhydride, and esterification), only two isolations were needed, providing almost quantitative yields. Similarly, butibufen was obtained in 64% yield using the direct hydrocarboxylation of β-substituted styrene **1m** (Scheme 2E).

Importantly, the hydrocarboxylation reaction can be scaled up (Scheme 2F). For this we changed the solvent from DME to diglyme (2-methoxyethyl ether), which has a higher boiling point, allowing the reaction to be performed in simple flasks using a CO_2 balloon. Starting from 1.5 g of stilbene, we could prepare 1.427 g of the corresponding acid **2a** (Scheme 2F). The yield at gram scale (76%, Scheme 2) is slightly larger compared to the small scale (67%, Table 1, entry 4), probably due to better recovery of material during work-up at larger scale.

The computational analysis of the CsF-mediated carboxylation of *in situ* generated organoboranes provided insights into the mechanistic steps. Three boranes were included in the theoretical study (Fig. 1): **b1** and **b2**, derived from the experimentally reactive alkenes *trans*-stilbene (**1a**) and *trans*-β-methylstyrene (**1f**), and **b3**, corresponding to the non-reactive alkene cyclohexene (**1o**). Three possible reaction mechanisms (referred to as **A**, **B** and **C**) were found by an automated search of the potential energy surface with the AFIR method.[14] Mechanism **A** (ESI, Fig. S6†) is characterized by a nucleophilic attack of the reactive carbon of the borane on a CO_2 molecule, followed by a transmetalation with CsF. This mechanism is considered not viable, as all the evaluated boranes show a computed Gibbs free activation energy of >50 kcal mol^{-1} for the first step (ESI, Table S2†).

Reaction mechanism **B** (Scheme 3) occurs through two steps: First, the formation of a B–F bond between the borane **i0** and a CsF molecule yielding intermediate **i1**, and second, the nucleophilic attack of intermediate **i1** on CO_2. The latter step is characterized by a concerted formation of the C–CO_2 bond and the cleavage of the B–C bond, releasing F-(9-BBN) and forming the product **p1**. The overall barrier computed for the different boranes with mechanism **B** (ESI, Table S3†) is significantly lower than with mechanism **A** (Table S2†). However, with values of 44.4 kcal mol^{-1} (cyclohexane-derived borane **b3**) to 52.3 kcal mol^{-1} (*trans*-β-methylstyrene-derived borane **b2**), the barriers are too high to be overcome at the reaction temperature of 120 °C.[15]

Scheme 3 Computed reaction mechanisms **B** and **C**.

The first step of mechanism **C** (Scheme 3) is the same as for **B**, the formation of intermediate **i1**. In the next step, the boron–carbon bond is cleaved, releasing a F-(9-BBN) molecule and forming the organocaesium intermediate **i2** (Fig. 2). In the final step, **i2** undergoes a nucleophilic attack on a CO_2 molecule. Interestingly, at the insertion TS for substrate **b1**, CO_2 shows no clear preference to interact with the cesium centre (Fig. 2; see also ESI, Fig. S9†), in contrast to other computational studies predicting CO_2–Cs interactions.[16] However, for **b2**, a preference for a weak CO_2–Cs interaction is seen (ESI, Fig. S10†). The reason may be that the Cs atom experiences stronger interactions with the two phenyl rings of **b1** than with the single aromatic ring in **b2**, making additional CO_2–Cs interactions preferable for **b2**.

For boranes **b1** and **b2**, the rate-limiting step of mechanism **C** is the cleavage of the boron–carbon bond with overall barriers of 34.0 kcal mol^{-1} for borane **b1** (derived from *trans*-stilbene) and 36.7 kcal mol^{-1} for **b2** (derived from *trans*-β-methylstyrene). Mechanism **C** is thus the preferred pathway for boranes **b1** and **b2**. The full energy profile for carboxylation of **b1** *via* mechanism **C** is shown in Fig. 3.

For borane **b3** (derived from cyclohexene), the rate-limiting step of mechanism **C** is the C–CO_2 bond formation with an overall barrier of 51.5 kcal mol^{-1}, which is not feasible. The lowest computed barrier for borane **b3** is thus observed with mechanism **B** (Fig. 3), which at 44.4 kcal mol^{-1} is not feasible at
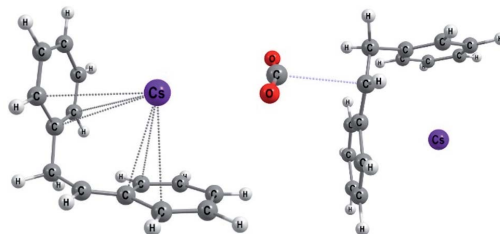

Fig. 1 Computationally investigated boranes.

Fig. 2 Optimized geometries for **b1** (Mechanism **C**): the organocaesium intermediate **i2** (left) and the C–CO_2 bond formation TS (TS$_{i2-p1}$, right).
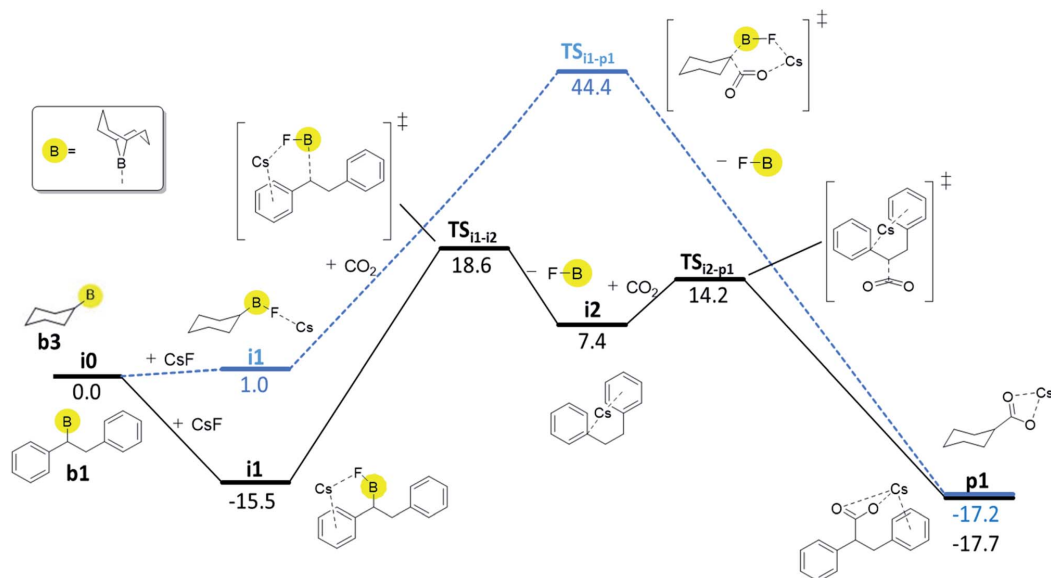
Fig. 3 Computed Gibbs free energy profile (kcal/mol; DLPNO-CCSD(T)//ωB97XD) of the preferred reaction pathways, mechanism **C** for **b1** (black solid line) and mechanism **B** for **b3** (blue dashed line).

the experimental temperature, in line with the experimentally observed lack of reactivity of cyclohexene.

Our computational and experimental results are in good agreement, indicating that the carboxylation of benzylic boranes occurs *via* reaction mechanism **C**, which features an organocaesium intermediate **i2**. The benzylic boranes **b1** and **b2** are able to stabilize the organocaesium intermediate **i2** *via* delocalization of the negative charge, and *via* cation–π interactions between caesium and the aromatic substituents on the organoborane. Similar Cs–π interactions have been observed in related computational studies.[17] The cost of forming **i2** is only 7.4 kcal mol^{-1} for **b1** and 12.7 kcal mol^{-1} for **b2**. The cyclohexyl borane **b3** lacks these stabilizing effects, resulting in a relative energy of 37.2 kcal mol^{-1} for the **i2** intermediate. We therefore suggest that the stability of the organocaesium intermediate **i2** is the factor determining the reactivity of olefins in the CsF-mediated hydrocarboxylation.

Conclusions

We report a CsF-mediated hydrocarboxylation of alkenes and allenes proceeding *via* a hydroboration with 9-BBN followed by a CsF-mediated carboxylation of the resulting organoboranes. The caesium fluoride-mediated carboxylation was effective for *in situ* generated benzylic and allylic organoboranes derived from stilbenes, β-substituted styrenes and allenes, providing the corresponding carboxylic acids with good yields and excellent regioselectivities. The developed methodology was demonstrated at gram-scale and was used for the production of commercial drugs. Computational studies indicate that

benzylic organoboranes are transformed to organocaesium intermediates, which then undergo a nucleophilic attack on CO_2. Stabilisation of the organocaesium intermediate by the aromatic substituent account for the observed selectivity towards benzylic organoboranes.

Methods

Experimental and computational details are given in the ESI.† The ESI includes experimental procedures and analytical data, an example input for DLPNO-CCSD(T) calculations, computed energies for the full reaction pathways for **b1**, **b2** and **b3**, and a comparison of computed C–CO_2 TS structures. A separate xyz file contains all optimized coordinates in a format that allows easy visualization with Mercury.

General procedure for metal–free hydrocarboxylation of stilbenes, β-substituted styrenes and allenes

Inside the glove box, a 45 mL pressure tube was charged with the corresponding olefin or allene (1.5 mmol), (9-BBN)$_2$ (1 equiv. for olefins or 0.7 equiv. for allenes) and dry DME (7 mL). The flask was closed with a suitable cap, removed from the glove box and heated to 70 °C (olefin) or 50 °C (allene) for 24 h. Afterwards, the pressure tube was transferred back to the glove box. To the reaction mixture at 20 °C was added CsF (3 equiv.). The pressure tube was closed with the cap and removed from the glove box. Afterwards CO_2 (120 mL) was added *via* a syringe, which was followed by stirring of the reaction mixture at 120 °C for 24 h. Next, the reaction mixture was

diluted with 30 mL Et$_2$O and transferred into a 500 mL separating funnel. The resulting mixture was extracted with 30 mL saturated basic (NaHCO$_3$, 1 M KOH) solution (3 times). The resulting basic solution was washed with 15 mL Et$_2$O (once), acidified (50–55 mL 6 M HCl) and extracted with 30 mL Et$_2$O (3 times). The resulting solution of Et$_2$O was distilled to dryness to give the corresponding acid (in case of **5c** the final solution of Et$_2$O was dried using Na$_2$SO$_4$, which was followed by careful evaporation of solvents).

Computational methods

Density functional theory (DFT) calculations were performed with the ωB97XD hybrid functional,[18] as implemented in Gaussian 16, Revision B.01.[19] Geometries were optimized with the SDD ECP and basis set for Cs and the 6-31+G* basis set for all other elements. Initial guess structures for the transition states were obtained through linear transit calculations and through artificial force induced reaction modelling (AFIR) as implemented in GRRM.[14] Solvation effects were included in the final geometry optimizations via the IEFPCM model (1,4-dioxane). Explicit solvent molecules may bind to specific points in the system, but we do not expect them to affect the overall mechanistic picture,[17] and because of this they were omitted from the calculation. Vibrational, entropic, and temperature corrections were computed at 393.15 Kelvin, with the same level of theory as geometry optimizations. Electronic energies were obtained with DLPNO-CCSD(T)[20] using ORCA 4.1.1.[21] The ZORA operator as well as the basis sets SARC-ZORA-TZVPP (for Cs) and ZORA-def2-QZVPP (all other elements) were employed. The final Gibbs free energies ($\Delta G_{\text{DLPNO-CCSD(T)}//\omega\text{B97XD}}$) in the main text correspond to the DLPNO-CCSD(T) electronic energies combined with the DFT-based vibrational, entropic and temperature corrections, and the standard state (SS, 393.15 K) conversion in case of a change in the number of moles:[22] $\Delta G_{\text{DLPNO-CCSD(T)}//\omega\text{B97XD}} = \Delta G_{\omega\text{B97XD/IEFPCM}} - \Delta E_{\omega\text{B97XD/IEFPCM}} + \Delta E_{\text{DLPNO-CCSD(T)}} + \text{SS}$. All ORCA and Gaussian calculations were performed on the Norwegian supercomputer Stallo at UiT, whereas GRRM calculations were performed on the computer cluster at ICIQ. More information on the computational details and example inputs as well as additional DFT energies are given in the ESI.†

Conflicts of interest

There are no conflicts to declare.

Acknowledgements

Notes and references

1 (a) M. Aresta, A. Dibenedetto and I. Tommasi, *Energy Fuels*, 2001, **15**, 269–273; (b) M. Mikkelsen, M. Jørgensen and F. C. Krebs, *Energy Environ. Sci.*, 2010, **3**, 43–81; (c) Q. Liu, L. Wu, R. Jackstell and M. Beller, *Nat. Commun.*, 2015, **6**, 5933, DOI: 10.1038/ncomms6933.

2 G. A. Olah, G. K. S. Prakash and A. Goeppert, *J. Am. Chem. Soc.*, 2011, **133**, 12881–12898.

3 For selected reviews on valorisation of CO$_2$, see: (a) M. Aresta, A. Dibenedetto and A. Angelini, *Chem. Rev.*, 2014, **114**, 1709–1742; (b) R. R. Shaikh, S. Pornpraprom and V. D'Elia, *ACS Catal.*, 2018, **8**, 419–450.

4 For a review on transition metal-catalysed C–C bond forming reactions involving CO$_2$, see: A. Tortajada, F. Juliá-Hernández, M. Börjesson, T. Moragas and R. Martin, *Angew. Chem., Int. Ed.*, 2018, **57**, 15948–15982.

5 (a) J. Vaitla, Y. Guttormsen, J. K. Mannisto, A. Nova, T. Repo, A. Bayer and K. H. Hopmann, *ACS Catal.*, 2017, **7**, 7231–7244; (b) M. Obst, L. Pavlovic and K. H. Hopmann, *J. Organomet. Chem.*, 2018, **864**, 115–127; (c) L. Pavlovic, J. Vaitla, A. Bayer and K. H. Hopmann, *Organometallics*, 2018, **37**, 941–948.

6 (a) T. Ohishi, L. Zhang, M. Nishiura and Z. Hou, *Angew. Chem., Int. Ed.*, 2011, **50**, 8114–8117; (b) H. Ohmiya, M. Tanabe and M. Sawamura, *Org. Lett.*, 2011, **13**, 1086–1088; (c) M. Juhl, S. L. R. Laursen, Y. Huang, D. U. Nielsen, K. Daasbjerg and T. Skrydstrup, *ACS Catal.*, 2017, **7**, 1392–1396.

7 (a) R. D. Grigg, J. W. Rigoli, R. V. Hoveln, S. Neale and J. M. Schomaker, *Chem.–Eur. J.*, 2012, **18**, 9391–9396; (b) T. Mita, K. Michigami and Y. Sato, *Org. Lett.*, 2012, **14**, 3462–3465; (c) M. Yonemoto-Kobayashi, K. Inamoto, Y. Tanaka and Y. Kondo, *Org. Biomol. Chem.*, 2013, **11**, 3773–3775; (d) T. Mita, M. Sugawara, K. Saito and Y. Sato, *Org. Lett.*, 2014, **16**, 3028–3031; (e) M. Yonemoto-Kobayashi, K. Inamoto and Y. Kondo, *Chem. Lett.*, 2014, **43**, 477–479; (f) X. Frogneux, N. von Wolff, P. Thuery, G. Lefevre and T. Cantat, *Chem. - Eur. J.*, 2016, **22**, 2930–2934.

8 For selected examples on Cu-catalysed/initiated decarboxylation, see: (a) T. Cohen and R. A. Schambach, *J. Am. Chem. Soc.*, 1970, **92**, 3189–3190; (b) O. Toussaini, P. Capdevielle and M. Maumy, *Tetrahedron*, 1984, **17**, 3229–3233; (c) L. J. Gooßen, W. R. Thiel, N. Rodriguez, C. Linder and B. Melzer, *Adv. Synth. Catal.*, 2007, **349**, 2241–2246; (d) L. J. Gooßen, N. Rodriguez, C. Linder, P. P. Lange and A. Fromm, *ChemCatChem*, 2010, **2**, 430–442.

9 For a selected review on borane-mediated hydroboration of olefins, see: *Selective Hydroboration and Synthetic Utility of Organoboranes Thus Obtained*, A. Suzuki and R. S. Dhillon, *Top. Curr. Chem.*, 1986, **130**, 23–88.

10 The selectivity of hydroboration is substrate dependent. For selected examples on borane-mediated hydroboration of β-substituted styrenes, see: (a) H. C. Brown, P. K. Jadhav and A. K. Mandal, *J. Org. Chem.*, 1982, **47**, 5074–5083; (b)

H. C. Brown, D. J. Nelson and C. G. Scouten, *J. Org. Chem.*, 1983, **48**, 641–643; (c) H. C. Brown and J. Chandrasekharan, *J. Org. Chem.*, 1983, **48**, 644–648; (d) H. C. Brown, J. V. N. V. Prasad and S. H. Zee, *J. Org. Chem.*, 1986, **51**, 439–445; (e) G. Erker and R. Aul, *Chem. Ber.*, 1991, **124**, 1301–1310; (f) J. M. Clay and E. Vedejs, *J. Am. Chem. Soc.*, 2005, **127**, 5766–5767; (g) P. Moquist, G.-Q. Chen, C. Muck-Lichtenfeld, K. Bussmann, C. G. Daniliuc, G. Kehr and G. Erker, *Chem. Sci.*, 2015, **6**, 816–825.

11 For selected examples on borane-mediated hydroboration of allenes, see:(a) H. C. Brown, R. Liotta and G. W. Kramer, *J. Am. Chem. Soc.*, 1979, **101**, 2966–2970; (b) K. K. Wang, Y. G. Gu and C. Liu, *J. Am. Chem. Soc.*, 1990, **112**, 4424–4431; (c) S.-C. Hung, Y.-F. Wen, J.-W. Chang, C.-C. Liao and B.-J. Uang, *J. Org. Chem.*, 2002, **67**, 1308–1313; (d) L. Yang, Z. Lin, S.-H. Huang and R. Hong, *Angew. Chem., Int. Ed.*, 2016, **55**, 6280–6284; (e) T. Suto, Y. Yanagita, Y. Nagashima, S. Takikawa, Y. Kurosu, N. Matsuo, T. Sato and N. Chida, *J. Am. Chem. Soc.*, 2017, **139**, 2952–2955; (f) Y. Nagashima, K. Sasaki, T. Suto, T. Sato and N. Chida, *Chem.–Asian J.*, 2018, **13**, 1024–1028.

12 For a review on asymmetric hydroborations using (−)-isopinocampheylborane, see: M. Srebnik and P. V. Ramachandran, *Aldrichimica Acta*, 1987, **20**, 9–24.

13 Related chiral organolithium reagents racemize above -78 °C, see: (a) *Stereochemical Aspects of Organolithium Compounds*, ed. R. E. Gawley, Verlag Helvetica Chimica Acta, Postfach, CH-8042 Zürich, Switzerland, 2010, ISBN: 978-3-906-39061-1; (b) A. Basu and S. Thayumanavan, *Angew. Chem., Int. Ed.*, 2002, **41**, 716–738; (c) H. J. Reich, *J. Org. Chem.*, 2012, **77**, 5471–5491.

14 S. Maeda, K. Ohno and K. Morokuma, *Phys. Chem. Chem. Phys.*, 2013, **15**, 3683–3701.

15 For a discussion of feasible barriers at different temperatures, see : H. Ryu, J. Park, H. K. Kim, J. Y. Park, S.-T. Kim and M.-H. Baik, *Organometallics*, 2018, **37**, 3228–3239.

16 H. D Velázquez, Z.-H. Wu, M. Vandichel and F. Verpoort, *Catal. Lett.*, 2017, **147**, 463–471.

17 R. Kuniyil and F. Maseras, *Theor. Chem. Acc.*, 2017, **136**, 65.

18 J.-D. Chai and M. Head-Gordon, *Phys. Chem. Chem. Phys.*, 2008, **10**, 6615–6620.

19 *Gaussian 16, Revision B.01*, M. J. Frisch, G. W. Trucks, H. B. Schlegel, G. E. Scuseria, M. A. Robb, J. R. Cheeseman, G. Scalmani, V. Barone, G. A. Petersson, H. Nakatsuji, X. Li, M. Caricato, A. V. Marenich, J. Bloino, B. G. Janesko, R. Gomperts, B. Mennucci, H. P. Hratchian, J. V. Ortiz, A. F. Izmaylov, J. L. Sonnenberg, D. Williams-Young, F. Ding, F. Lipparini, F. Egidi, J. Goings, B. Peng, A. Petrone, T. Henderson, D. Ranasinghe, V. G. Zakrzewski, J. Gao, N. Rega, G. Zheng, W. Liang, M. Hada, M. Ehara, K. Toyota, R. Fukuda, J. Hasegawa, M. Ishida, T. Nakajima, Y. Honda, O. Kitao, H. Nakai, T. Vreven, K. Throssell, J. A. Montgomery, Jr., J. E. Peralta, F. Ogliaro, M. J. Bearpark, J. J. Heyd, E. N. Brothers, K. N. Kudin, V. N. Staroverov, T. A. Keith, R. Kobayashi, J. Normand, K. Raghavachari, A. P. Rendell, J. C. Burant, S. S. Iyengar, J. Tomasi, M. Cossi, J. M. Millam, M. Klene, C. Adamo, R. Cammi, J. W. Ochterski, R. L. Martin, K. Morokuma, O. Farkas, J. B. Foresman, and D. J. Fox, Gaussian, Inc., Wallingford CT, 2016.

20 Y. Guo, C. Riplinger, U. Becker, D. Liakos, Y. Minenkov, L. Cavallo and F. Neese, *J. Chem. Phys.*, 2018, **148**, 011101.

21 (a) F. Neese, The ORCA program system, *Wiley Interdiscip. Rev.: Comput. Mol. Sci.*, 2012, **2**(1), 73–78; (b) F. Neese, Software update: the ORCA program system, version 4.0, *Wiley Interdiscip. Rev.: Comput. Mol. Sci.*, 2017, **8**(1), 1327.

22 (a) K. H. Hopmann, *Organometallics*, 2016, **35**, 3795–3807; (b) C. J. Cramer, *Essentials of Computational Chemistry: Theories and models*, Wiley, 2004, p. 379.

Paper II

Mechanistic Insights into Copper-Catalyzed Carboxylations

M. Obst, A. Gevorgyan,
A. Bayer, and K. H. Hopmann

Supporting Information and

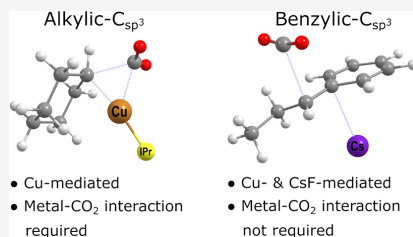a .XYZ file can be found under:

https://doi.org/10.1021/acs.organomet.9b00710

Mechanistic Insights into Copper-Catalyzed Carboxylations

Marc F. Obst,[†] Ashot Gevorgyan,[‡] Annette Bayer,*,[‡] and Kathrin H. Hopmann*,[†]

[†]Hylleraas Center for Quantum Molecular Sciences, Department of Chemistry, UiT The Arctic University of Norway, N-9037 Tromsø, Norway

[‡]Department of Chemistry, UiT The Arctic University of Norway, N-9037 Tromsø, Norway

S *Supporting Information*

ABSTRACT: The copper-NHC-catalyzed carboxylation of organo-boranes with CO_2 was investigated using computational and experimental methods. The DFT and DLPNO-CCSD(T) results indicate that nonbenzylic substrates are converted via an inner-sphere carboxylation of an organocopper intermediate, whereas benzylic substrates may simultaneously proceed along both inner- and outer-sphere CO_2 insertion pathways. Interestingly, the computations predict that two conceptually different carboxylation mechanisms are possible for benzylic organoboranes, one being copper-catalyzed and one being mediated by the reaction additive CsF. Our experimental evaluation of the computed reactions confirms that carboxylation of nonbenzylic substrates requires copper catalysis, whereas benzylic substrates can be carboxylated with and without copper.

Alkylic-C_{sp3}

Benzylic-C_{sp3}

- Cu-mediated
- Metal-CO_2 interaction required

- Cu- & CsF-mediated
- Metal-CO_2 interaction not required

INTRODUCTION

Carbon dioxide has significant potential as a carbon source for chemical synthesis, because it is plentiful, readily available, and cheap.[1−7] In this function, CO_2 could help replace fossil carbon sources, such as crude oil or natural gas, thus reducing the dependence on these finite resources. A challenge in this approach is the relatively high chemical inertness of CO_2, resulting in the necessity for catalysts or reactive cosubstrates for many reactions involving CO_2. Nevertheless, CO_2-based synthesis pathways for a variety of products have been developed, which can be classified into three categories: (i) reactions selectively reducing CO_2 to formic acid, CO, methanol, or lower alkanes, (ii) reactions fixating CO_2 through carbon−carbon (C−C) bond formation to form e.g. carboxylic acids, and (iii) reactions fixating CO_2 through carbon−heteroatom (C−X) bond formation, leading to cyclic carbonates or carbamates.[6−8]

A Cu(I)-based system able to fixate CO_2 through C−C bond formation was published independently by Hou[9] and Sawamura[10] in 2011 and improved upon by Skrydstrup, Nielsen, and co-workers[11] in 2017 (Scheme 1). The reaction

Scheme 1. Cu-Catalyzed Carboxylations Reported by Hou (X = 70, Y = 24, Cu = CuCl, L = IPr, B = MeOLi, R″ = H), Sawamura (X = 100, Y = 12, Cu = CuOAc, L = 1,10-phen, B = KO^{t}Bu, R″ = H), and Skrydstrup (X = 120, Y = 16, Cu = CuI, L = IPr, B = CsF, R″ = Alkyl)[9−11]

1) (9-BBN)$_2$, Solvent
2) **Cu, Ligand L**, Base B,
CO$_2$, X °C, Y h
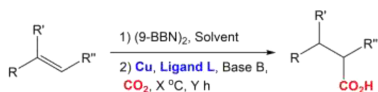
protocol involves two steps: first, a hydroboration with the 9-borabicyclo[3.3.1]nonane dimer (9-BBN)$_2$ and, second, a (1,10-phenanthroline)Cu(I)- or IPrCu(I)-catalyzed (IPr = 1,3-bis(2,6-diisopropylphenyl)imidazol-2-ylidene) carboxylation of the in situ formed organoborane with CO_2 in the presence of a base. Skrydstrup and co-workers employed the milder base CsF instead of the strong alkoxides used by Sawamura or Hou, expanding the scope of substrates to cyclic olefins, stilbenes, β-substituted styrenes, and terminal acetylenes.[9−11]

We here set out to investigate the mechanistic details of the Cu-NHC-catalyzed carboxylation of in situ formed organo-boranes.[11] To achieve this goal, we employed computational methods, namely density functional theory (DFT) and domain-based local pair natural orbital coupled cluster (DLPNO-CCSD(T)). We were particularly interested to establish if the CO_2 molecule experiences activation from the copper center during C−C bond formation (implying an inner-sphere mechanism) or if an outer-sphere path with a free CO_2 molecule is preferred, as recently proposed by us for Rh-catalyzed hydrocarboxylation.[12] Further, it can be noted that the Cu-catalyzed reaction reported by Skrydstrup, Nielsen, and co-workers occurs in the presence of 3 equivalents of CsF,[11] and we thus paid particular attention to the role of CsF in the reaction mechanism, because we recently showed that it may promote carboxylations.[13] Different types of substrates were investigated, involving both a benzylic and a nonbenzylic organoborane, which here are shown to have different
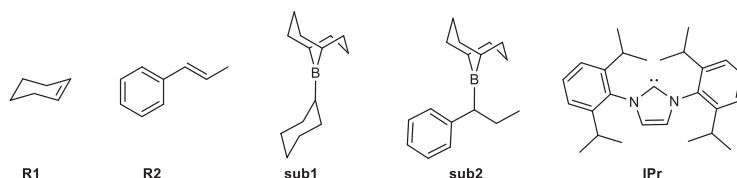
Figure 1. The two investigated organoboranes **sub1** (derived from cyclohexene **R1**) and **sub2** (derived from *trans-β*-methylstyrene **R2**) as well as the NHC ligand used, IPr.

mechanistic preferences. Our experiments support the computational predictions.

■ COMPUTATIONAL AND EXPERIMENTAL DETAILS

Computational Model. All calculations were performed on the full molecular systems without any truncations or symmetry constraints. The two in situ formed organoboranes **sub1** and **sub2** (Figure 1) derived from cyclohexene **R1** and *trans-β*-methylstyrene **R2**, respectively, were used to investigate the reaction mechanism. These substrates were chosen because they previously showed high yields in experiments (**R1**, 94%; **R2**, 89%)[11] while having different electronic properties. For steps where CsF enters or leaves, the reference structure for CsF was modeled as a dimer, Cs_2F_2. However, as the exact nature of the CsF reference state under experimental conditions (dioxane solvent, 120 °C) is not known, we also computed the overall barriers with an alternative tetrameric reference state (Cs_4F_4) for comparison (Table S1 and Scheme S1).

Computational Methods. Geometries were optimized using the long-range corrected ωB97XD functional.[14] This functional was chosen on the basis of good results in recent benchmarks.[15,16] Additional DFT calculations were performed using the PBE[17,18] and B3LYP[19] functionals with the GD3BJ[20] dispersion correction to assess the robustness of the computed results (details are given in the Supporting Information). The employed software was Gaussian16 B.01 for all DFT calculations.[21] For optimizations, the basis set BS1 was used, which consists of the SDD basis for Cu and Cs as well as the 6-31+G* basis for all other elements. DFT single-point (SP) energies were calculated at the BS2 level, using the same DFT functional as used in optimizations. BS2 comprises the SDD basis for Cu and the def2-TZVP basis for all other elements. Both BS1 and BS2 employed the SDD ECPs for Cu and Cs. Solvation effects were included in optimizations and SP calculations through the use of an IEFPCM model of 1,4-dioxane.

In order to obtain accurate electronic energies beyond DFT, we employed DLPNO-CCSD(T).[22,23] This method is reported to have an accuracy comparable to that of CCSD(T), while scaling considerably better, allowing the treatment of large molecules with high accuracy.[24−26] The DLPNO-CCSD(T) SP energies were calculated using the ωB97XD-based geometries obtained as described above. The DLPNO-CCSD(T) method was used with the scalar-relativistic ZORA operator and basis set BS3, consisting of the SARC-ZORA-TZVPP basis for Cs and the minimally augmented ma-ZORA-def2-TZVPP basis for all other elements. These calculations were accelerated by using the RIJCOSX approximation[27] employing the auxiliary basis sets def2-TZVP/C and SARC/J. The employed software for these calculations was ORCA 4.1.2.[28] The final DLPNO-CCSD(T) standard state Gibbs free energies ($\Delta G_{CCSD(T)}$) were obtained by applying the ωB97XD-based thermal, entropic, and solvation corrections at 393.15 K (120 °C) and the BS1 level to the SP DLPNO-CCSD(T) electronic energies. Unless explicitly stated otherwise, the $\Delta G_{CCSD(T)}$ energies are used for the discussion.

$$\Delta G_{CCSD(T)} = \Delta G_{\omega B97XD,PCM,BS1} - \Delta E_{\omega B97XD,Vac,BS1}$$
$$+ \Delta E_{CCSD(T),Vac,BS3} \qquad (1)$$

Final DFT standard state Gibbs free energies were obtained similarly by applying the BS1 thermal and entropic corrections (393.15 K) to the SP DFT energies calculated at the BS2 level:

$$\Delta G_{DFT} = \Delta G_{DFT,PCM,BS1} - \Delta E_{DFT,PCM,BS1} + \Delta E_{DFT,PCM,BS2}$$
$$(2)$$

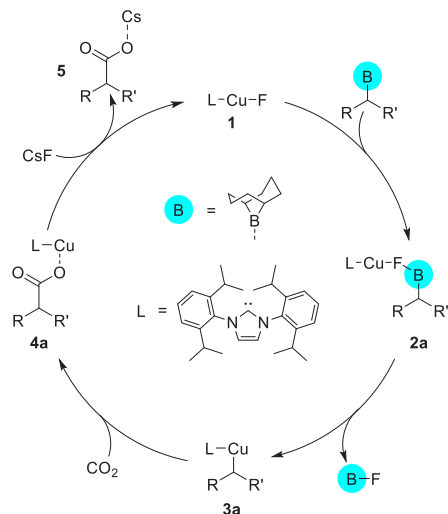All energies correspond to a 1 atm standard state.

Experimental Methods. Commercially available starting materials, reagents, catalysts, and anhydrous and degassed solvents were used without further purification. Thin-layer chromatography was carried out using Merck TLC silica gel 60 F_{254} and visualized by short-wavelength ultraviolet light or by treatment with potassium permanganate ($KMnO_4$) stain. ^{1}H and ^{13}C NMR spectra were recorded on a Bruker Avance 400 MHz spectrometer at 20 °C. All ^{1}H NMR spectra are reported in parts per million (ppm) downfield of TMS and were measured relative to the signals for $CHCl_3$ (7.26 ppm). All ^{13}C NMR spectra were reported in ppm relative to residual $CDCl_3$ (77.20 ppm) and were obtained with ^{1}H decoupling. Coupling constants, J, are reported in hertz (Hz). High-resolution mass spectra (HRMS) were recorded from methanol solutions on an LTQ Orbitrap XL instrument (Thermo Scientific) in negative electrospray ionization (ESI) mode. Melting points were measured using a Stuart SMP50 automatic melting point detector.

General Procedure for Cu-Catalyzed/Cu-Free Hydrocarboxylation. Inside a glovebox, a 45 mL pressure tube was charged with the corresponding olefin (1.7 mmol), (9-BBN)$_2$ (1 equiv), and dry dioxane (4 mL (Cu-catalyzed), 6 mL (Cu-free)). The flask was closed with a suitable cap, removed from the glovebox, and heated to 65 °C for 16 h. Afterward, the pressure tube was transferred back to the glovebox. To the reaction mixture at 20 °C was added CsF (3 equiv) and, in the case of Cu-catalyzed reactions, a solution of the catalyst (a mixture of CuI (5 mol %), IPrHCl (6 mol %), and NaO*t*Bu (6 mol %) in dry dioxane (3 mL) stirred at 20 °C for 30 min before use). The pressure tube was closed with a cap and removed from the glovebox. Afterward, CO_2 (120 mL) was added via a syringe, followed by stirring the reaction mixture at 120 °C for 16 h. Next, the reaction mixture was diluted with 30 mL of Et$_2$O and transferred into a 500 mL separating funnel. The resulting mixture was extracted with 30 mL of saturated basic (NaHCO$_3$) solution (three times). The resulting basic solution was washed with 15 mL of Et$_2$O (once), acidified (50−55 mL 6 M HCl), and extracted with 30 mL of Et$_2$O (three times). The resulting solution of Et$_2$O was distilled to dryness to give the corresponding acid.

■ RESULTS AND DISCUSSION

Cu(I)-Catalyzed Conversion of sub1. We initiated our investigation of the copper-catalyzed carboxylation of organoboranes from the mechanism proposed by Skrydstrup, Nielsen, and co-workers.[11] Their schematic proposal suggests a transmetalation of I-Cu-IPr with CsF to form the active species F-Cu-IPr, which reacts with the organoborane to give a Cu-alkyl intermediate, followed by insertion of CO_2. Our computational results indicate that such a mechanism is feasible for the cyclohexene-derived organoborane **sub1**, although our data suggest some modifications to the original proposal, with the obtained mechanism shown in Scheme 2.

Scheme 2. Computed Catalytic Cycle for the Copper-NHC-Catalyzed Carboxylation of Organoboranes, Based on Our Work Here and the Proposed Mechanism by Skrydstrup, Nielsen, and Co-workers[a],[11]

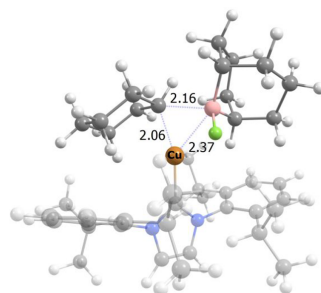[a]The "B" in a blue circle denotes 9-BBN.

Figure 3. Optimized geometry of $TS_{2a\text{-}3a}$ for **sub1**. Distances are in Å. The NHC ligand (IPr) is transparent for clarity. Color code for this and subsequent figures: C, gray; H, white; N, blue; B, pink; F, green; O, red.

We will refer to this mechanism as **A**, with the computed Gibbs free energy profile for **sub1** shown in Figure 2.

The computed pathway **A** starts with a nucleophilic attack of the fluoride ligand of the active species (F-Cu-IPr) at the boron atom of the substrate. The corresponding transition state ($TS_{1\text{-}2a}$) has a barrier of 16.8 kcal/mol relative to **1** and is characterized by a partial transfer of the fluoride from copper to boron. At the intermediate **2a**, the fluoride is bridging between boron and the metal center. The energy of this intermediate is 7.2 kcal/mol. In the following step, a concerted rearrangement leads to the formation of the Cu-alkyl intermediate **3a**, concomitant with release of (9-BBN)-F. This step has a barrier of 22.8 kcal/mol and can be viewed as a transmetalation, with the cyclic TS ($TS_{2a\text{-}3a}$, Figure 3) composed of copper, boron, and the reactive carbon. When

this TS is reached, the fluoride is already fully transferred to boron. A separate TS for fluoride transfer could not be identified. The formed Cu-alkyl intermediate **3a** has a relative energy of 0.4 kcal/mol, making it relatively stable. **3a** can then insert a CO_2 molecule via $TS_{3a\text{-}4a}$. Several TSs were identified for this step, which can be classified as inner- or outer-sphere, depending on the presence of Cu−CO_2 interactions at the transition state. With a computed barrier of 31.9 kcal/mol, the inner-sphere TS is clearly preferred for **sub1**, in comparison to the outer-sphere TS with a barrier of 39.6 kcal/mol (Figure 4). The energies obtained with different DFT functionals (ωB97XD, PBE-D3BJ, B3LYP-D3BJ) provide the same clear preference for an inner-sphere attack (Table S2 in the Supporting Information). This result is in line with the inner-sphere mechanism predicted for carboxylation of non-benzylic C_{sp^3} carbons with Rh complexes,[30−32] but it is in contrast to computational work on Ni- and Pd-mediated carboxylations, supporting outer-sphere pathways for non-benzylic C_{sp^3} carbons.[32−34] In our computations, the CO_2 insertion step is rate-limiting. The formed intermediate **4a** has a relative energy of −11.3 kcal/mol. The final step of the catalytic cycle is the transmetalation of **4a** with CsF to regenerate the active species F-Cu-IPr and form the product **5** (relative energy of −15.0 kcal/mol). No TS for this transmetalation could be located. The overall barrier of 31.9 kcal/mol for the Cu(I)-IPr-catalyzed carboxylation of **sub1** via
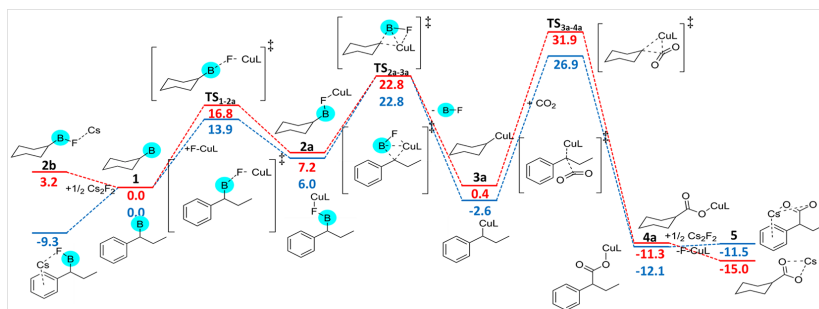
Figure 2. Computed Gibbs free energy profile (kcal/mol) of the Cu(I)-catalyzed path **A** for **sub1** (red) and **sub2** (blue). The "B" in a blue circle denotes 9-BBN, and L denotes IPr.

TS$_{3a\text{-}4a}$(inner): 31.9 kcal/mol   **TS$_{3a\text{-}4a}$(outer)**: 39.6 kcal/mol
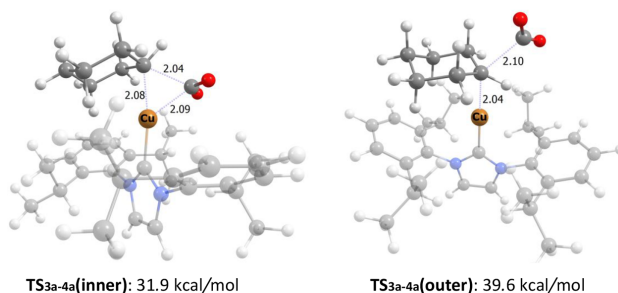
Figure 4. Optimized geometries of the inner- and outer-sphere TS for CO$_2$ insertion (**TS$_{3a\text{-}4a}$**) with the nonbenzylic substrate **sub1**. Distances are in Å. The IPr ligand is transparent for clarity. Color code as in Figure 3.

**TS$_{3a\text{-}4a}$(inner)**: 27.2 kcal/mol   **TS$_{3a\text{-}4a}$(outer)**: 26.9 kcal/mol
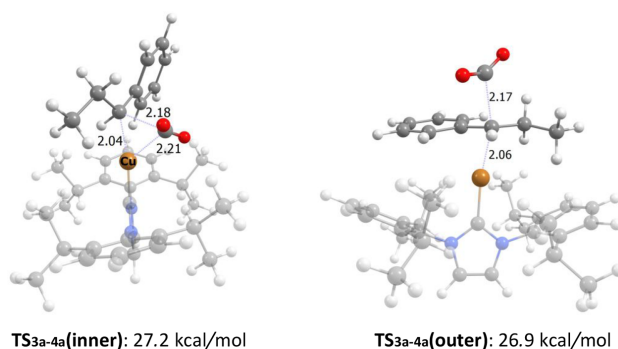
Figure 5. Optimized geometries for the inner- and outer-sphere TS for CO$_2$ insertion (**TS$_{3a\text{-}4a}$**) with the benzylic substrate **sub2**. Distances are in Å, and energies are relative to **1**. The IPr ligand is transparent for clarity. Color code as in Figure 3.

Table 1. Computed Overall Standard State Gibbs Free Energy Barriers (kcal/mol, 323 K) for the Cu-Catalyzed Pathway A and CsF-Mediated Pathway B Obtained at Different Levels of Theory

substrate	method	solvation model	path **A**	path **B**	$\Delta\Delta G$(**A**−**B**)
sub1	DLPNO-CCSD(T)	PCM	31.9	53.3	−21.4
sub1	DLPNO-CCSD(T)	PCM+Explicit	31.9	47.7	−15.5
sub1	ωB97XD	PCM	33.6	53.9	−20.3
sub1	ωB97XD	PCM+Explicit	33.6	48.6	−15.0
sub1	PBE-GD3BJ	PCM	26.4	49.6[a]	−23.2
sub1	B3LYP-GD3BJ	PCM	29.9	50.5[a]	−20.6
sub2	DLPNO-CCSD(T)	PCM	36.2	37.0	−0.8
sub2	DLPNO-CCSD(T)	PCM+Explicit	39.2	38.6	0.6
sub2	ωB97XD	PCM	40.4	36.4	4.0
sub2	ωB97XD	PCM+Explicit	40.6	35.6	5.0
sub2	PBE-GD3BJ	PCM	25.6	29.6[a]	−4.0
sub2	B3LYP-GD3BJ	PCM	29.8	28.9[a]	0.9

[a]Energies based on SP calculations on the ωB97XD structures (**TS$_{3b\text{-}5}$**), as reoptimization at the given level was unsuccessful.

Scheme 3. Our Proposed Mechanism for the CsF-Mediated Carboxylation of Benzylic Organoboranes
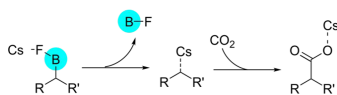
path **A** is feasible at the experimental temperature of 393 K (on the basis of the discussion by Baik and co-workers,[35] a barrier

of up to ~33.2 kcal/mol should be viable). It can be noted that path **A** for C$_{sp^3}$ carboxylation of the nonbenzylic organoborane **sub1** is similar to the reported mechanism for Cu-NHC-catalyzed C$_{sp^2}$ carboxylation of arylboronate esters,[36] although the involvement of CsF here, instead of KO^{t}Bu, provides some differences with respect to the formed intermediates and products.

Cu(I)-Catalyzed Conversion of sub2. The computed steps for the Cu-IPr-catalyzed carboxylation of the *trans-β*-methylstyrene-derived borane **sub2** are essentially as for **sub1**,
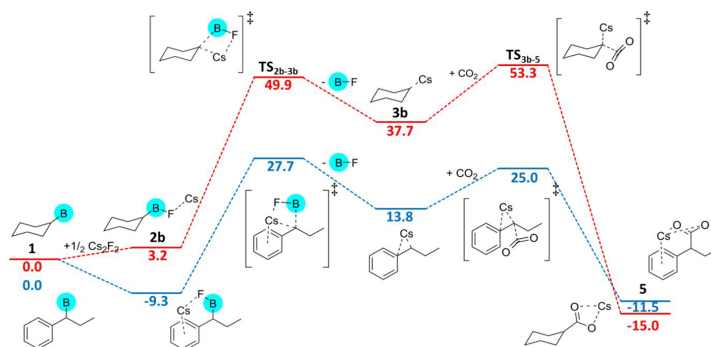
Figure 6. Computed Gibbs free energy profile (kcal/mol) of the CsF-mediated pathway **B** for the two substrates **sub1** (red) and **sub2** (blue). The "B" in a blue circle denotes 9-BBN.
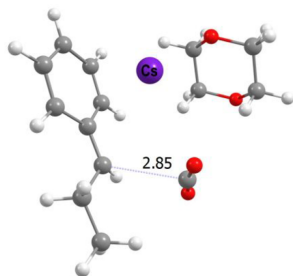
Figure 7. CO_2 insertion TS (**TS$_{3b-5}$**) for **sub2** via path **B** in the presence of a 1,4-dioxane molecule. Color code as in Figure 3.

with the Gibbs free energy profile shown in Figure 2. However, there are two major differences. First, for the CO_2 insertion TS, the inner- and outer-sphere conformers are only 0.3 kcal/mol apart (**TS$_{3a-4a}$**, Figure 5). This indicates that, for benzylic carbons, a Cu-NHC-catalyzed carboxylation may operate via *both* inner- and outer-sphere pathways. The DFT-based energies also support this conclusion (Tables S2 and S3 in the Supporting Information). It can be noted that a recent study on Cu-NHC-mediated boracarboxylation of alkenes reported an inner-sphere TS for carboxylation of a benzylic C_{sp^3} carbon;[37] however, it is unclear if the outer-sphere path was evaluated. For Rh-mediated carboxylations, we have earlier observed a very strong preference for outer-sphere pathways for benzylic substrates.[12] Second, **sub2** features a different resting state in comparison to **sub1**, which is greatly influencing the rate-limiting barrier. Our calculations predict that the complexation of **sub2** with the reaction additive CsF leads to an energetically low-lying species (**2b**), −9.3 kcal/mol below **1**. This raises the rate-limiting barrier for CO_2 insertion from 29.5 kcal/mol to 36.2 kcal/mol for **sub2**, which appears slightly above a feasible barrier limit at the experimental temperature (∼33.2 kcal/mol, vide supra). It can be noted that the barrier of this step is dependent on which CsF reference state is employed in calculations. If the reference state is Cs_4F_4 instead of Cs_2F_2, the barrier for **TS$_{3a-4a}$** is reduced from 36.2 to 33.5 kcal/mol (see Table S1 in the Supporting Information). Thus, there is an uncertainty in the carboxylation barrier for **sub2** with mechanism **A**, which is further discussed below

(Table 1). For **sub1**, a similar CsF–substrate adduct **2b** can also be optimized (Figure 2), but it is not lower in energy than **1** and therefore does not influence the rate-limiting barrier for **sub1**.

We proceeded to explore if a variant of pathway **A**, with a transmetalation of the alkyl to copper occurring directly from the CsF–**sub2** adduct **2b**, may provide lower barriers. However, this pathway showed unfeasible barriers of at least 47 kcal/mol for **sub2** (Table S4 in the Supporting Information). The adduct **2b** is thus not expected to be reactive, and it needs to dissociate prior to Cu-catalyzed transmetalation of **sub2**.

CsF-Mediated Carboxylation. We recently showed that CsF can mediate the carboxylation of benzylic boranes.[13] As the reaction conditions (Scheme 1) of the copper system involves addition of 3 equiv of CsF, we proceeded to explore if the additive could be the carboxylating agent. Setting out from the low-lying **2b** adduct, a possible carboxylation pathway involving a organocaesium species **3b** may exist, as shown in our previous work.[13] This pathway will be referred to as path **B** and is shown in Scheme 3, while the corresponding computed Gibbs free energy profile is shown in Figure 6. This pathway is of no importance for **sub1**, for which we compute a rate-limiting barrier of 53.3 kcal/mol (Figure 6). However, for **sub2** the rate-limiting barrier computed for the CsF-mediated carboxylation path **B** is 37.0 kcal/mol (Figure 6), indicating that it is equally likely to occur as the copper-catalyzed pathway **A** (36.2 kcal/mol, Figure 2). It needs to be mentioned here that the TS for the rate-limiting step of path **B** (**TS$_{2b-3b}$**) shows only a small imaginary frequency of 16i to 35i cm^{-1} with the different DFT functionals, making both its optimization and its interpretation challenging.[38] However, a displacement of the TS geometry along the intrinsic reaction coordinate (IRC) supports that **TS$_{2b-3b}$** indeed is linking **2b** and **3b**, implying that the small imaginary frequency may be an inherent feature of this TS.

Explicit Solvation Effect. All calculations presented above (Figures 2 and 6) were performed with an implicit IEFPCM model to obtain an approximate estimate of the effect of the solvent (1,4-dioxane) on the reaction geometries and energies. This is a standard approach in computational chemistry; however, it does not take into account the effect that explicit solvent may have. We here recomputed paths **A** and **B** with one explicit 1,4-dioxane molecule added as a ligand to the Cs-

Scheme 4. Experimental Conditions and Yields for Cu-Catalyzed and CsF-Mediated Carboxylation of Cyclohexene and *trans-β*-Methylstyrene
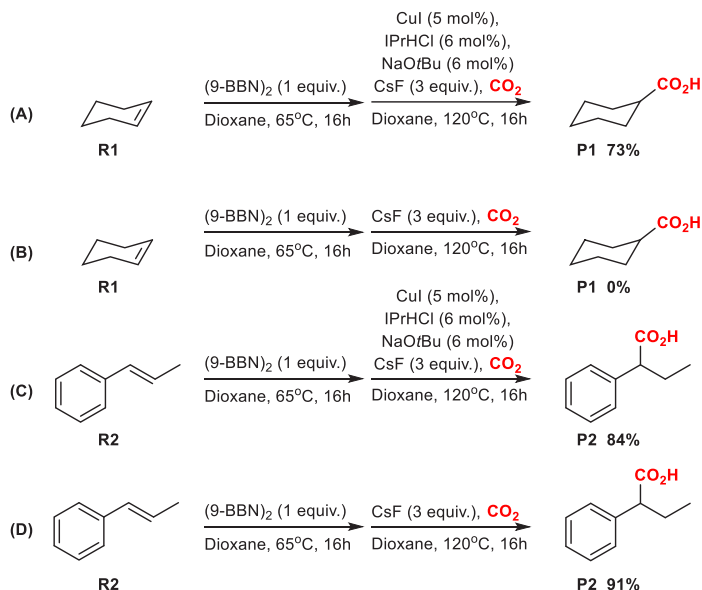
containing species (Figure 7). For the different computational protocols, the computed barriers (Tables S5 and S6 in the Supporting Information) are either identical or change by a maximum of 3 kcal/mol relative to the energies obtained with the implicit solvent model. In particular, we find that the involvement of explicit solvent does *not* change the proposed mechanistic preferences of **sub1** (preferably path **A**) or **sub2** (paths **A** and **B** equally likely with DLPNO-CCSD(T)).

Discussion of the Computed Barriers. Table 1 shows the computed overall barriers at 323 K for the Cu-catalyzed pathway **A** and the CsF-mediated pathway **B** for **sub1** and **sub2** obtained with different levels of theory.

For **sub1**, it can be seen that the different computational protocols predict barriers that vary by up to 7.2 kcal/mol. However, all methods predict that the preferred pathway is **A**, which has a feasible barrier close to the discussed threshold of 33.2 kcal/mol at 323 K[35] for all electronic structure methods (DLPNO-CCSD(T), ωB97XD, PBE-D3BJ, B3LYP-D3BJ) and molecular models (with/without 1,4-dioxane) tested here. Instead, for path **B**, all methods and models predict a barrier above 47 kcal/mol for **sub1**. This strongly indicates that Cu catalysis via path **A** is viable for **sub1**, whereas the CsF-mediated path **B** is excluded.

For **sub2**, the different protocols predict barriers that vary by up to 15 kcal/mol (Table 1). This large variation cannot be explained definitely, but one possibility is that the stability of the predicted resting state of **sub2** (the low-lying CsF–substrate adduct **2b**) may be described rather differently by the different methods. This state is not involved in the reactivity of **sub1**, where smaller energetic variations between the computational protocols are observed. The results for **sub2** show a trend, where the computed barriers for both path **A** and **B** are consistently below 33 kcal/mol with B3LYP-D3BJ or PBE-

D3BJ but consistently above 33 kcal/mol with DLPNO-CCSD(T) or ωB97XD. Although the results indicate that both paths **A** and **B** may be equally likely to occur for **sub2**, a clear conclusion regarding their feasibility cannot be made. An important point in this analysis is the expected accuracy of the computed values. Absolute barriers obtained with DFT may have an error of more than 5 kcal/mol,[29] and also for DLPNO-CCSD(T), a recent benchmark showed an average deviation of more than 7 kcal/mol between experimental and computed dissociation energies,[39] with the origin of the error being unknown. A conclusion on the feasibility of paths **A** and **B** for **sub2** thus cannot be made from computations alone. We therefore proceeded to perform experimental tests.

Experimental Evaluation. A possible prediction derived from our computational work is that **sub1** will only work under Cu-catalysis (path **A**), whereas **sub2** may be converted either with Cu-catalysis (path **A**) or via a CsF-mediated path (path **B**). We tested this hypothesis by redoing the experiment in Scheme 1 with the two alkenes cyclohexene (**R1**; the precursor of organoborane **sub1**) and *trans-β*-methylstyrene (**R2**; the precursor of organoborane **sub2**), with or without Cu-IPr added to the reaction mixture (Scheme 4). For cyclohexene, the reaction gives 0% yield in the absence of copper but 73% yield in the presence of copper. This is in excellent agreement with the computed barriers, predicting that Cu-catalysis is essential for **sub1** (Table 1). For this substrate, the results for path **A** indicate that the CsF additive only seems to be important for the transmetalation step allowing reformation of the active IPr-Cu-F species but it should not be involved in the CO_2 insertion.

In contrast, the **sub2** precursor *trans-β*-methylstyrene is converted to the carboxylic acid with and without copper added to the reaction mixture, providing 84% and 91% yields,

respectively (Scheme 4). The higher yield in the absence of copper may be attributed to a decarboxylation reaction mediated by the copper complex.[13] The experimental results support the prediction that conversion of **sub2** can occur in the absence of copper, indicating that path **B** may be operative. In the presence of both copper and CsF, it cannot be determined which pathway occurs for **sub2**, but on the basis of our computations indicating similar barriers for the copper-catalyzed path **A** and the CsF-mediated path **B** (Table 1), we predict that both occur simultaneously.

CONCLUSIONS

We have investigated the Cu-NHC-catalyzed carboxylation of cyclohexene and *trans-β*-methylstyrene using DFT and DLPNO-CCSD(T). Several interesting conclusions can be drawn. First, a main conclusion is that nonbenzylic organoboranes such as **sub1** require copper for successful CO_2 insertion, whereas for the benzylic organoborane **sub2**, the copper-catalyzed reaction and the CsF-mediated carboxylation path appear equally accessible. This behavior is consistent for different computational protocols and models. Our experimental testing verified the need for copper for **sub1** but showed good carboxylation of the benzylic carbon in **sub2** in the absence of copper.

Second, an analysis of the involved transition states shows that nonbenzylic C_{sp^3} substrates prefer an inner-sphere carboxylation (where CO_2 exhibits interactions with the metal center), whereas the benzylic C_{sp^3} species can proceed along both inner- and outer-sphere routes for CO_2 insertion. A clear consensus regarding inner- versus outer-sphere mechanism for $C-CO_2$ bond formation is currently not available from the literature. Both inner and outer have been predicted for metal-coordinated C_{sp^3} carbons,[12,30−34,37] although sometimes only one alternative appears to have been studied computationally. The intimate details of the CO_2 insertion step are of particular interest for developing enantioselective carboxylations, where the inner and outer pathways would give opposite configurations. Our conclusions that both CO_2 insertion modes may occur simultaneously in Cu-IPr-based carboxylations of benzylic carbons indicate that attempts to develop an asymmetric variant of this type of reactions are unlikely to succeed. More investigations regarding the effect of the metal catalyst and substrate on the preferred CO_2 insertion mode are in progress in our laboratory.

ASSOCIATED CONTENT

Ⓢ Supporting Information

The Supporting Information is available free of charge at https://pubs.acs.org/doi/10.1021/acs.organomet.9b00710.

> Additional computational results, experimental procedures, data for compound characterization, and NMR spectra (PDF)
>
> Cartesian coordinates of the calculated structures (XYZ)

AUTHOR INFORMATION

Corresponding Authors

*E-mail for A.B.: annette.bayer@uit.no.
*E-mail for K.H.H.: kathrin.hopmann@uit.no.

ORCID Ⓘ

Annette Bayer: 0000-0003-3481-200X
Kathrin H. Hopmann: 0000-0003-2798-716X

REFERENCES

(1) Otto, A.; Grube, T.; Schiebahn, S.; Stolten, D. Closing the loop: captured CO_2 as a feedstock in the chemical industry. *Energy Environ. Sci.* **2015**, 8, 3283−3297.

(2) Dai, W.-L.; Luo, S.-L.; Yin, S.-F.; Au, C.-T. The direct transformation of carbon dioxide to organic carbonates over heterogeneous catalysts. *Appl. Catal., A* **2009**, 366, 2−12.

(3) Ma, J.; Sun, N.; Zhang, X.; Zhao, N.; Xiao, F.; Wei, W.; Sun, Y. A short review of catalysis for CO_2 conversion. *Catal. Today* **2009**, 148, 221−231.

(4) Liu, Q.; Wu, L.; Jackstell, R.; Beller, M. Using carbon dioxide as a building block in organic synthesis. *Nat. Commun.* **2015**, 6, 5933.

(5) Dabral, S.; Schaub, T. The Use of Carbon Dioxide (CO_2) as a Building Block in Organic Synthesis from an Industrial Perspective. *Adv. Synth. Catal.* **2019**, 361, 223−246.

(6) Aresta, M.; Dibenedetto, A.; Angelini, A. Catalysis for the valorization of exhaust carbon: from CO_2 to chemicals, materials, and fuels. Technological use of CO_2. *Chem. Rev.* **2014**, 114, 1709−42.

(7) Aresta, M.; Dibenedetto, A.; Quaranta, E. State of the art and perspectives in catalytic processes for CO_2 conversion into chemicals and fuels: The distinctive contribution of chemical catalysis and biotechnology. *J. Catal.* **2016**, 343, 2−45.

(8) Shaikh, R. R.; Pornprapram, S.; D'Elia, V. Catalytic Strategies for the Cycloaddition of Pure, Diluted, and Waste CO_2 to Epoxides under Ambient Conditions. *ACS Catal.* **2018**, 8, 419−450.

(9) Ohishi, T.; Zhang, L.; Nishiura, M.; Hou, Z. Carboxylation of alkylboranes by N-heterocyclic carbene copper catalysts: synthesis of carboxylic acids from terminal alkenes and carbon dioxide. *Angew. Chem., Int. Ed.* **2011**, 50, 8114−7.

(10) Ohmiya, H.; Tanabe, M.; Sawamura, M. Copper-catalyzed carboxylation of alkylboranes with carbon dioxide: formal reductive carboxylation of terminal alkenes. *Org. Lett.* **2011**, 13, 1086−8.

(11) Juhl, M.; Laursen, S. L. R.; Huang, Y.; Nielsen, D. U.; Daasbjerg, K.; Skrydstrup, T. Copper-Catalyzed Carboxylation of Hydroborated Disubstituted Alkenes and Terminal Alkynes with Cesium Fluoride. *ACS Catal.* **2017**, 7, 1392−1396.

(12) Pavlovic, L.; Vaitla, J.; Bayer, A.; Hopmann, K. H. Rhodium-Catalyzed Hydrocarboxylation: Mechanistic Analysis Reveals Unusual Transition State for Carbon−Carbon Bond Formation. *Organometallics* **2018**, 37, 941−948.

(13) Gevorgyan, A.; Obst, M. F.; Guttormsen, Y.; Maseras, F.; Hopmann, K. H.; Bayer, A. Caesium Fluoride-Mediated Hydrocarboxylation of Alkenes and Allenes: Scope and Mechanistic Insights. *Chem. Sci.* **2019**, 10, 10072−10078.

(14) Chai, J. D.; Head-Gordon, M. Long-range corrected hybrid density functionals with damped atom-atom dispersion corrections. *Phys. Chem. Chem. Phys.* **2008**, 10, 6615−6620.

(15) Goerigk, L.; Hansen, A.; Bauer, C.; Ehrlich, S.; Najibi, A.; Grimme, S. A look at the density functional theory zoo with the advanced GMTKN55 database for general main group thermochemistry, kinetics and noncovalent interactions. *Phys. Chem. Chem. Phys.* **2017**, 19, 32184−32215.

(16) Mardirossian, N.; Head-Gordon, M. Thirty years of density functional theory in computational chemistry: an overview and extensive assessment of 200 density functionals. *Mol. Phys.* **2017**, 115, 2315−2372.

(17) Perdew, J. P.; Burke, K.; Ernzerhof, M. Generalized Gradient Approximation Made Simple. *Phys. Rev. Lett.* **1996**, *77*, 3865−3868.

(18) Perdew, J. P.; Burke, K.; Ernzerhof, M. Generalized Gradient Approximation Made Simple [Phys. Rev. Lett. 77, 3865 (1996)]. *Phys. Rev. Lett.* **1997**, *78*, 1396−1396.

(19) Becke, A. D. Density-functional thermochemistry. III. The role of exact exchange. *J. Chem. Phys.* **1993**, *98*, 5648−5652.

(20) Grimme, S.; Ehrlich, S.; Goerigk, L. Effect of the damping function in dispersion corrected density functional theory. *J. Comput. Chem.* **2011**, *32*, 1456−65.

(21) Frisch, M. J.; Trucks, G. W.; Schlegel, H. B.; Scuseria, G. E.; Robb, M. A.; Cheeseman, J. R.; Scalmani, G.; Barone, V.; Petersson, G. A.; Nakatsuji, H.; Li, X.; Caricato, M.; Marenich, A. V.; Bloino, J.; Janesko, B. G.; Gomperts, R.; Mennucci, B.; Hratchian, H. P.; Ortiz, J. V.; Izmaylov, A. F.; Sonnenberg, J. L.; Williams; Ding, F.; Lipparini, F.; Egidi, F.; Goings, J.; Peng, B.; Petrone, A.; Henderson, T.; Ranasinghe, D.; Zakrzewski, V. G.; Gao, J.; Rega, N.; Zheng, G.; Liang, W.; Hada, M.; Ehara, M.; Toyota, K.; Fukuda, R.; Hasegawa, J.; Ishida, M.; Nakajima, T.; Honda, Y.; Kitao, O.; Nakai, H.; Vreven, T.; Throssell, K.; Montgomery, J. A., Jr.; Peralta, J. E.; Ogliaro, F.; Bearpark, M. J.; Heyd, J. J.; Brothers, E. N.; Kudin, K. N.; Staroverov, V. N.; Keith, T. A.; Kobayashi, R.; Normand, J.; Raghavachari, K.; Rendell, A. P.; Burant, J. C.; Iyengar, S. S.; Tomasi, J.; Cossi, M.; Millam, J. M.; Klene, M.; Adamo, C.; Cammi, R.; Ochterski, J. W.; Martin, R. L.; Morokuma, K.; Farkas, O.; Foresman, J. B.; Fox, D. J. *Gaussian 16 Rev. B.01*; Gaussian, Inc.: Wallingford, CT, 2016.

(22) Riplinger, C.; Neese, F. An efficient and near linear scaling pair natural orbital based local coupled cluster method. *J. Chem. Phys.* **2013**, *138*, 034106.

(23) Riplinger, C.; Sandhoefer, B.; Hansen, A.; Neese, F. Natural triple excitations in local coupled cluster calculations with pair natural orbitals. *J. Chem. Phys.* **2013**, *139*, 134101.

(24) Sparta, M.; Neese, F. Chemical applications carried out by local pair natural orbital based coupled-cluster methods. *Chem. Soc. Rev.* **2014**, *43*, 5032−41.

(25) Liakos, D. G.; Sparta, M.; Kesharwani, M. K.; Martin, J. M. L.; Neese, F. Exploring the Accuracy Limits of Local Pair Natural Orbital Coupled-Cluster Theory. *J. Chem. Theory Comput.* **2015**, *11*, 1525−1539.

(26) Minenkov, Y.; Chermak, E.; Cavallo, L. Accuracy of DLPNO-CCSD(T) method for noncovalent bond dissociation enthalpies from coinage metal cation complexes. *J. Chem. Theory Comput.* **2015**, *11*, 4664−76.

(27) Neese, F.; Wennmohs, F.; Hansen, A.; Becker, U. Efficient, approximate and parallel Hartree−Fock and hybrid DFT calculations. A 'chain-of-spheres' algorithm for the Hartree−Fock exchange. *Chem. Phys.* **2009**, *356*, 98−109.

(28) Neese, F. The ORCA program system. *WIREs Comput. Mol. Sci.* **2012**, *2*, 73−78.

(29) Hopmann, K. H. How Accurate is DFT for Iridium-Mediated Chemistry? *Organometallics* **2016**, *35*, 3795−3807.

(30) Ostapowicz, T. G.; Hölscher, M.; Leitner, W. Catalytic Hydrocarboxylation of Olefins with CO_2 and H_2- a DFT Computational Analysis. *Eur. J. Inorg. Chem.* **2012**, *2012*, 5632−5641.

(31) Ostapowicz, T. G.; Hölscher, M.; Leitner, W. CO_2 insertion into metal-carbon bonds: a computational study of Rh(I) pincer complexes. *Chem. - Eur. J.* **2011**, *17*, 10329−38.

(32) Schmeier, T. J.; Hazari, N.; Incarvito, C. D.; Raskatov, J. A. Exploring the reactions of CO_2 with PCP supported nickel complexes. *Chem. Commun.* **2011**, *47*, 1824−6.

(33) Lau, K.-C.; Petro, B. J.; Bontemps, S.; Jordan, R. F. Comparative Reactivity of Zr− and Pd−Alkyl Complexes with Carbon Dioxide. *Organometallics* **2013**, *32*, 6895−6898.

(34) Johnson, M. T.; Johansson, R.; Kondrashov, M. V.; Steyl, G.; Ahlquist, M. r. S. G.; Roodt, A.; Wendt, O. F. Mechanisms of the CO_2 Insertion into (PCP) Palladium Allyl and Methyl σ-Bonds. A Kinetic and Computational Study. *Organometallics* **2010**, *29*, 3521−3529.

(35) Ryu, H.; Park, J.; Kim, H. K.; Park, J. Y.; Kim, S.-T.; Baik, M.-H. Pitfalls in Computational Modeling of Chemical Reactions and How To Avoid Them. *Organometallics* **2018**, *37*, 3228−3239.

(36) Dang, L.; Lin, Z.; Marder, T. B. DFT Studies on the Carboxylation of Arylboronate Esters with CO_2 Catalyzed by Copper(I) Complexes. *Organometallics* **2010**, *29*, 917−927.

(37) Lv, X.; Wu, Y.-B.; Lu, G. Computational exploration of ligand effects in copper-catalyzed boracarboxylation of styrene with CO_2. *Catal. Sci. Technol.* **2017**, *7*, 5049−5054.

(38) The imaginary frequency is inversely proportional to the square root of the reduced mass of the vibrating atoms. If many atoms are displaced during the TS, the imaginary frequency will necessarily be small. The obtained imaginary frequencies for TS_{2b-3b} for **sub1** and **sub2** are respectively $19i$ and $16i$ cm^{-1} for ωB97XD, $25i$ cm^{-1} and $23i$ cm^{-1} for B3LYP-D3, and $35i$ and $13i$ cm^{-1} for PBE-D3BJ.

(39) Husch, T.; Freitag, L.; Reiher, M. Calculation of Ligand Dissociation Energies in Large Transition-Metal Complexes. *J. Chem. Theory Comput.* **2018**, *14*, 2456−2468.

Paper III

Ni(I)−Alkyl Complexes Bearing Phenanthroline Ligands: Experimental Evidence for CO$_2$ Insertion at Ni(I) Centers

R. Somerville, C. Odena, M. Obst
N. Hazari, K. H. Hopmann, and R. Martin

Supporting Information and

a .XYZ file can be found under:

https://dx.doi.org/10.1021/jacs.0c04695

Ni(I)−Alkyl Complexes Bearing Phenanthroline Ligands: Experimental Evidence for CO_2 Insertion at Ni(I) Centers

Rosie J. Somerville, Carlota Odena,[#] Marc F. Obst,[#] Nilay Hazari, Kathrin H. Hopmann,* and Ruben Martin*

Cite This: https://dx.doi.org/10.1021/jacs.0c04695

Read Online

ACCESS | Metrics & More | Article Recommendations | Supporting Information

ABSTRACT: Although the catalytic carboxylation of unactivated alkyl electrophiles has reached remarkable levels of sophistication, the intermediacy of (phenanthroline)Ni(I)−alkyl species—complexes proposed in numerous Ni-catalyzed reductive cross-coupling reactions—has been subject to speculation. Herein we report the synthesis of such elusive (phenanthroline)Ni(I) species and their reactivity with CO_2, allowing us to address a long-standing question related to Ni-catalyzed carboxylation reactions.

Over the past decade, Ni-catalyzed reductive carboxylation reactions involving organic (pseudo)halides and carbon dioxide have received considerable attention as methodologies for the preparation of many synthetically useful carboxylic acids.[1] Among the wide variety of Ni-catalyzed reductive carboxylation reactions developed to date, the carboxylation of *unactivated* alkyl (pseudo)halides possessing β-hydrogens was found to be particularly challenging.[2] This is likely due to the propensity of the alkylnickel intermediates that are formed via $C(sp^3)−X$ scission (X = Br, Cl, OSO_2R) to undergo unproductive reduction, β-hydride elimination, and homocoupling reactions.[3] Although nickel catalysts supported by (di)phosphine or N-heterocyclic carbene ligands are routinely employed in a myriad of Ni-catalyzed C−C and C−heteroatom bond-forming reactions,[4] only finely tuned 1,10-phenanthroline derivatives—phen ligands—have enabled the carboxylation of unactivated alkyl electrophiles either at the initial $C(sp^3)−X$ site or at remote $C(sp^3)−H$ bonds via chain-walking of the Ni catalyst along the alkyl side chain (Scheme 1).[2,5] Furthermore, a careful analysis of the literature indicates that phen ligands are also crucial for a wide number of Ni-catalyzed cross-couplings of unactivated alkyl halides, indicating that the importance of these ligands extends beyond carboxylation reactions.[4,6]

Scheme 1. Carboxylation of Unactivated Alkyl Electrophiles
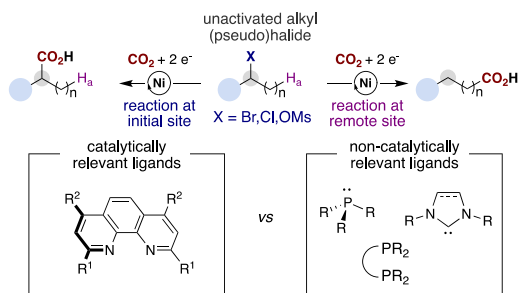
Despite significant advances in methodology design, the mechanism of the Ni-catalyzed reductive carboxylation of unactivated alkyl (pseudo)halides with CO_2 is poorly understood. At present, our knowledge is primarily based on studies using *aryl* (pseudo)halide substrates. These suggest that CO_2 insertion at a (phen)Ni(I)−alkyl complex is a crucial elementary step (Scheme 2, left).[7,8] However, it is worth noting that no

Scheme 2. Proposed Reductive Carboxylation Mechanism via CO_2 Insertion at Phen-Ligated Ni(I)−Alkyl Species
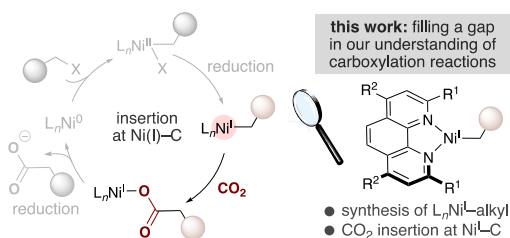
(phen)Ni(I)−alkyl complexes have been structurally characterized or even observed spectroscopically, probably because of the fleeting nature and high reactivity of these paramagnetic species.[9] Elegant efforts toward this goal were recently described by Diao, and cultimated in the synthesis of (diphosphine)Ni-(I)−alkyl complexes and investigations into their reactivity with CO_2.[10,11] Unfortunately, diphosphine ligands have not been shown to facilitate the Ni-catalyzed carboxylation of unactivated alkyl (pseudo)halides (Scheme 1).[2,12] Therefore, a study aimed
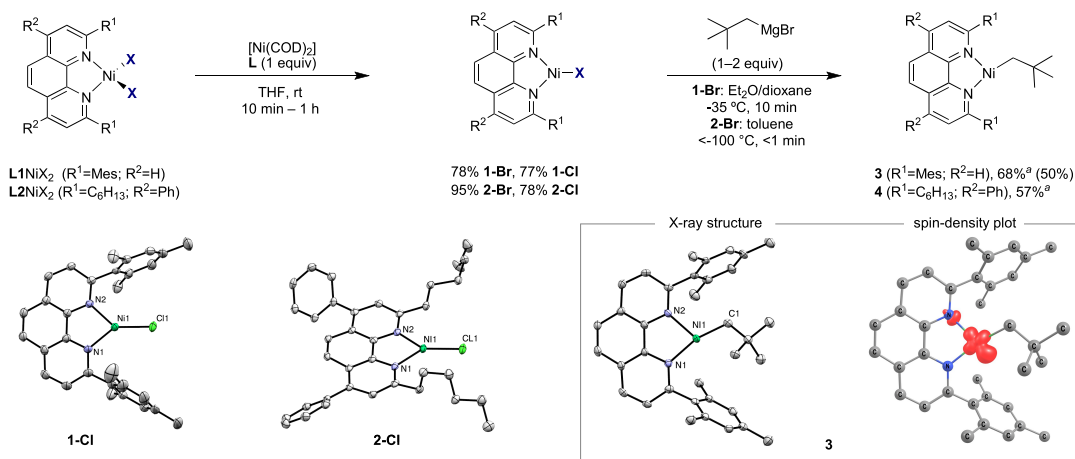
Figure 1. (top) Synthesis of Ni(I)−X and Ni(I)−alkyl complexes. [a]Yield determined by EPR spectroscopy against Cu(II) standards. All other yields are isolated yields (0.010 mmol scale for **3**). (bottom left and center) X-ray structures with thermal ellipsoids drawn at the 50% probability level (see the Supporting Information for details). Selected distances (Å) and angles (deg): **1-Cl**: Ni1−Cl1 2.1064(6), N1−Ni1−Cl1 140.24(6), N2−Ni1−Cl1 136.32(6). **2-Cl**: Ni−Cl1 2.1417(9), N1−Ni−Cl1 133.80(8), N2−Ni−Cl1 142.61(9). **3**: Ni−C1 1.961(3), N1−Ni−C1 156.74(14), C1−Ni−N2 114.25(13). (bottom right) Calculated spin-density plot of **3** with a spin population of 0.94 on Ni (PBE-D3BJ/def2-TZVP, isovalue = 0.01; Figure S33).

at preparing well-defined Ni(I)−alkyl complexes bearing catalytically relevant phen ligands would represent (a) an opportunity to study the reactivity of elusive Ni(I)−alkyl complexes supported by nitrogen-donor ligands, (b) a foundation for investigating the mechanistic intricacies of catalytic reductive carboxylation reactions, and (c) a starting point for understanding the speciation of Ni catalysts supported by phen ligands in related cross-coupling and chain-walking reactions.[4] Herein we report the realization of these goals through the synthesis and isolation of Ni(I)−alkyl complexes bearing phen ligands, which has enabled us to obtain experimental evidence for rapid CO_2 insertion at Ni(I)−carbon bonds (Scheme 2, right). These results not only shed light on a long-speculated mechanistic step but also support efforts to exploit and expand the reactivity of (phen)Ni(I)−alkyl intermediates through photoredox or electrochemical methodologies.[2a,b,4,13]

Our study began by establishing a route to Ni(I)−halide complexes bearing phen ligands **L1** or **L2**. The choice of these ligands was not arbitrary, as substituents adjacent to the nitrogen donor atoms are critical in Ni-catalyzed reductive carboxylation reactions of unactivated alkyl (pseudo)halides.[2] Steric shielding by the bulky mesityl substituents of **L1** may help to stabilize our targeted Ni(I)−alkyl complexes, which are likely highly reactive.[9,14] Additionally, **L2** is employed in the Ni-catalyzed chain-walking carboxylation of alkyl bromides.[2c] We envisioned that (**L**)Ni(I)−alkyl species could be accessed by alkylation of inner-sphere Ni(I)−halide complexes with an appropriate organometallic reagent. However, at the outset of our investigations, it was unclear whether an inner-sphere (**L**)Ni-(I)−halide precursor could be obtained, as the most closely related reported species bearing a phen ligand was the outer-sphere halide complex [Ni(**L**)$_2$]Cl, formed via oxidation of Ni(0)**L**$_2$ (**L** = 2,9-dimethylphen) with AgCl.[8,14,16] In order to avoid the synthesis of Ni(0)**L**$_2$ complexes and the purification steps required to remove oxidation byproducts, we hypothesized

that inner sphere (**L**)Ni(I)X (X = Br, Cl) might be obtained via comproportionation of (**L**)NiX$_2$ with [Ni(COD)$_2$] in the presence of 1 equiv of bulky **L**.[15,16] This was indeed the case, and deep-blue (**L**)Ni(I)X species were obtained in high yields (Figure 1, left). The presence of the inner-sphere halide ligand was confirmed by X-ray crystallographic analysis of **1-Cl** and **2-Cl**. In addition, the axial electron paramagnetic resonance (EPR) spectra of the four (**L**)Ni(I)X complexes at 77 K support the presence of a Ni-centered radical. These results are noteworthy, as they represent examples of Ni(I) complexes bearing phen ligands with the halide directly coordinated to the Ni center.[16,17] With a reliable route to (**L1,L2**)Ni(I)X in hand, we turned our attention to accessing the targeted Ni(I)−alkyl complexes via alkylation. An initial survey of the stability of the resulting Ni(I)−alkyl products was carried out by monitoring these reactions using EPR spectroscopy. As expected, the choice of alkyl group, reaction temperature, and ligand employed all influenced the reaction outcome. For example, reactions with EtMgBr and MeMgCl resulted in negligible amounts of new metal-centered radicals, if any. Analysis of these reactions by ^{1}H NMR spectroscopy indicated the presence of Ni(0)**L**$_n$ complexes, suggesting decomposition pathways arising from β-hydride elimination, reduction, and/or homolytic cleavage.[18]

Gratifyingly, the reactions of **1-Br** and **2-Br** with neopentylMgBr resulted in new rhombic EPR spectra, suggesting that the desired alkylation may have taken place.[19] Low-temperature crystallization (−35 °C, Et$_2$O/pentane) furnished deep-green crystals suitable for X-ray diffraction, allowing us to identify three-coordinate [(**L1**)Ni(I)CH$_2$tBu] (**3**) (Figure 1, right). Density functional theory (DFT) calculations support the Ni(I) description, with one unpaired electron centered on Ni (Figures 1 and S33). The synthesis of **3** is particularly noteworthy: to the best of our knowledge, *it is the first Ni(I)−alkyl complex to be obtained with a catalytically relevant phen ligand*. The Ni−C bond distance of 1.961(3) Å is similar to that of Ni(I) complexes bearing phosphine or NHC ligands.[10,20] The
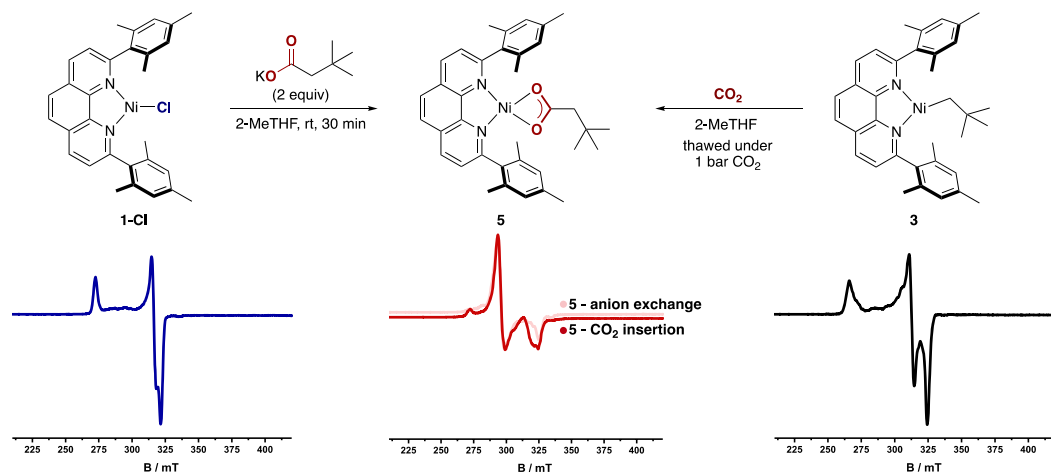
Figure 2. CO_2 insertion at Ni(I). (top) Anion metathesis reaction (left) and CO_2 insertion into **3** (right). (bottom) Changes in the 77 K X-band EPR spectra of **1-Cl** (left, $g_x = 2.084$, $g_y = 2.119$, $g_z = 2.461$) after anion metathesis and after CO_2 insertion at **3** (right, $g_x = 2.065$, $g_y = 2.145$, $g_z = 2.519$) to form **5** (center, $g_x = 2.299$, $g_y = 2.272$, $g_z = 2.064$).
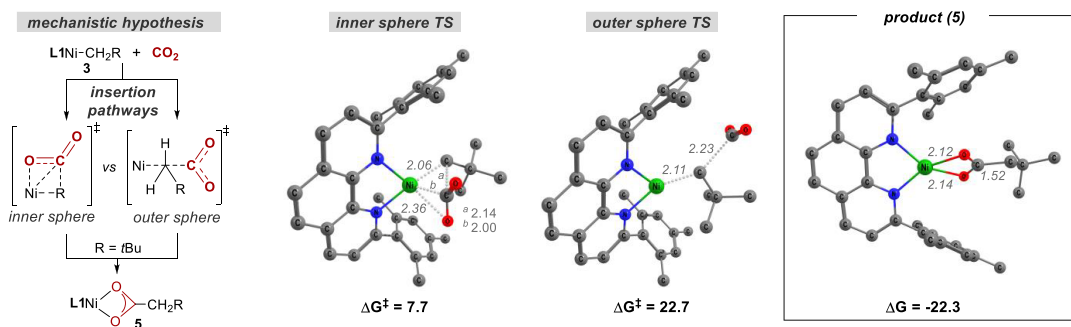

Figure 3. Optimized TS geometries for inner-sphere vs outer-sphere CO_2 insertion and the optimized geometry of **5** (PBE-D3BJ/def2-TZVP/IEFPCM, H atoms omitted, distances in Å, energies in kcal mol^{-1} relative to **3** + free CO_2, 298.15 K).

Ni coordination plane is offset by ca. 23° from the mean plane through **L1**, presumably because of the steric bulk of the neopentyl ligand. Interestingly, the N−Ni−C angles in **3** are 114.25(13)° and 156.74(14)°. The distortion of **3** to this T-shaped geometry is similar to that observed in a related diphosphine species [(dtbpe)Ni(CH$_2t$Bu)] (dtbpe = 1,2-bis(di-*tert*-butylphosphino)ethane) (110.97(8)° and 157.82(8)°).[20a] This geometry is electronically favored for a range of three-coordinate Ni(I) complexes and differs from the Y-shaped geometry of **1-Cl** and **2-Cl**.[21,22] We propose that the geometry of the latter complexes is due to the π-donating nature of the chloride ligand, which has been shown to favor Y-shaped complexes.[22] Alkylation of **2-Br** at low temperature gave [(**L2**)Ni(I)CH$_2t$Bu] (**4**) in 57% yield as estimated by EPR spectroscopy against a Cu(II) standard. Unfortunately, the thermal instability of **4** prevented its isolation or characterization by X-ray diffraction.

Next, we turned our attention to an investigation of CO_2 insertion into the Ni(I)−C bond en route to Ni(I) carboxylate complexes, proposed to be the key elementary step in the catalytic carboxylation of alkyl (pseudo)halides (Figure 2).[7,8]

Prior to these insertion experiments, however, an anion metathesis reaction between **1-Cl** and tBuCH$_2$CO$_2$K was performed to obtain reference EPR and IR spectra of the proposed CO_2 insertion product (Figure 2, left). Gratifyingly, spectroscopic analysis of the reaction mixture showed the formation of a complex distinct from both **3** and **1-Cl** and supported the formation of Ni(I)−carboxylate complex **5**. For example, the band in the IR spectrum at 1543 cm^{-1} is suggestive of a ν_{asym} carboxylate stretch.[23] Furthermore, although repeated attempts to crystallize **5** did not provide crystals suitable for X-ray diffraction, the observed stretching frequency combined with the absence of signals between 1200 and 1400 cm^{-1} suggests κ^2 coordination of the carboxylate to the Ni(I) center.[23a] This was supported by DFT calculations that suggested a pseudotetrahedral geometry for **5** (Figure 3, right) with a computed stretching frequency of 1484 cm^{-1} (Figure S36). With these results in hand, we next investigated the reaction between **3** and CO_2 (1 bar) at −60 °C (Figure 2, right). Analysis by EPR spectroscopy (77 K) showed the disappearance of the rhombic signal of **3** and the appearance of a new pseudoaxial signal with g_x, $g_y > g_z$ that very closely resembles the spectrum of **5** (Figure 2, center).

Importantly, comparison of the IR spectrum of the product of direct CO_2 insertion with that of the anion metathesis product showed an identical ν_{asym} carboxylate stretch at 1543 cm^{-1}. Particularly illustrative was the disappearance of this signal and the appearance of new signals at lower wavenumber when the reaction was performed with $^{13}CO_2$, providing evidence that **5** was formed via CO_2 insertion into the Ni(I)−C bond. Calculations predicted a 34 cm^{-1} shift to lower wavenumbers upon incorporation of ^{13}C, consistent with the observed shift of 38 cm^{-1} to a band at 1505 cm^{-1} (Figures S18 and S37). Insertion was also corroborated by quenching in-situ-generated **5** with dilute HCl and observing a 52% yield of *tert*-butylacetic acid (Scheme 3, top). These observations are

Scheme 3. CO_2 Insertion En Route to tBuCH$_2$CO$_2$H
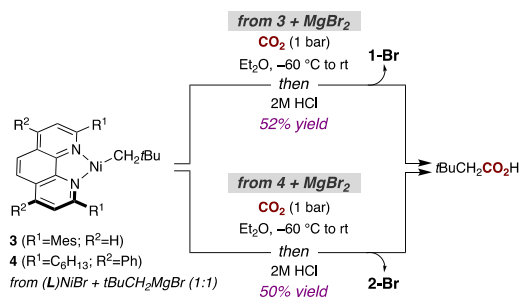
consistent with DFT calculations indicating facile CO_2 insertion into the Ni(I)−C bond of **3** with a free energy barrier of 7.7 kcal mol^{-1} relative to **3** and free CO_2 (Figure 3, middle). The calculations argue against the formation of a stable Ni−CO_2 adduct before insertion (Figure S38), with interactions between Ni and CO_2 first becoming significant at the carboxylation transition state (TS), where CO_2 is significantly bent (137°) and interacts with Ni in a η^2(C,O) fashion (Figure 3, center). Notably, an alternative *outer-sphere* insertion where CO_2 does not interact with Ni in the transition state is predicted to have a barrier of 22.7 kcal mol^{-1}, a 15.0 kcal mol^{-1} penalty compared to the inner-sphere pathway (Figure 3, center).[24] Although an inner-sphere pathway has been calculated for the Ni/PCp$_3$-catalyzed reductive carboxylation of benzyl halides,[25] our data contrast with the outer-sphere pathway suggested for (Xantphos)Ni(I)−methyl and (PCP pincer)Ni(II)−methyl complexes.[9,11] While one might argue that the bulky neopentyl group in **3** disfavors an outer-sphere pathway, we note that the inner-sphere pathway at the less sterically encumbered [(**L1**)-Ni(I)Me] was still found to be favored computationally by 6.6 kcal mol^{-1} (Figure S39). This finding is important, as it supports the notion that the ancillary ligand can influence the mechanism of CO_2 insertion.[24,26]

Given the relevance of **L2** in Ni-catalyzed carboxylation reactions, CO_2 insertion at **4** was also studied. Although the sensitivity of **4** prevented workup to remove MgBr$_2$ (the byproduct obtained by reacting (**L2**)Ni(I)Br with 1 equiv of neopentylMgBr), a 50% yield of *tert*-butylacetic acid was obtained upon exposure of a cold solution of **4** to CO_2 (1 bar) and then to dilute HCl (Scheme 3, bottom). Interestingly, this reaction mixture rapidly turned blue upon CO_2 addition, and only **2-Br** was observed by EPR spectroscopy. This suggested that the **L2** carboxylate complex [(**L2**)Ni(I)-O$_2$CCH$_2$$t$Bu] (**6**) resulting from CO_2 insertion at Ni(I)

underwent halide exchange with MgBr$_2$ to form blue **2-Br**. This was confirmed by the addition of MgBr$_2$ to salt-free **5**. Given the wide number of Ni-catalyzed reductive coupling reactions that employ MgX$_2$ (X = Br, Cl) additives,[27] the formation of **2-Br** from in situ-generated **6** provides support for the formation of Ni(I) halide complexes prior to reduction to the propagating Ni(0)L$_n$ species.[28]

In conclusion, we have investigated the synthesis and CO_2 insertion reactivity of Ni(I)−alkyl complexes bearing catalytically relevant phen ligands. We have obtained experimental evidence for the rapid insertion of CO_2 into Ni(I)−C bonds, a long-presumed elementary step in the reductive carboxylation of alkyl (pseudo)halides. Given the widespread use of phen ligands in Ni-catalyzed reactions, these results are expected to guide new investigations into the catalytic relevance of Ni(I)−alkyl complexes. Further investigations along these lines are currently underway in our laboratories.

■ ASSOCIATED CONTENT

ⓢ Supporting Information

The Supporting Information is available free of charge at https://pubs.acs.org/doi/10.1021/jacs.0c04695.

Crystallographic data for **1-Cl** (CIF)

Crystallographic data for **2-Cl** (CIF)

Crystallographic data for **3** (CIF)

Cartesian coordinates of calculated structures (XYZ)

Experimental procedures, spectra, crystallographic details, and computational details (PDF)

■ AUTHOR INFORMATION

Corresponding Authors

Ruben Martin − *Institute of Chemical Research of Catalonia (ICIQ), The Barcelona Institute of Science and Technology, 43007 Tarragona, Spain; ICREA, 08010 Barcelona, Spain;* ◉ orcid.org/0000-0002-2543-0221; Email: rmartinromo@iciq.es

Kathrin H. Hopmann − *Hylleraas Center for Quantum Molecular Sciences, Department of Chemistry, UiT The Arctic University of Norway, N-9307 Tromsø, Norway;* ◉ orcid.org/0000-0003-2798-716X; Email: kathrin.hopmann@uit.no

Authors

Rosie J. Somerville − *Institute of Chemical Research of Catalonia (ICIQ), The Barcelona Institute of Science and Technology, 43007 Tarragona, Spain; Departament de Química Analítica i Química Orgànica, Universitat Rovira i Virgili, 43007 Tarragona, Spain*

Carlota Odena − *Institute of Chemical Research of Catalonia (ICIQ), The Barcelona Institute of Science and Technology, 43007 Tarragona, Spain; Departament de Química Analítica i Química Orgànica, Universitat Rovira i Virgili, 43007 Tarragona, Spain*

Marc F. Obst − *Hylleraas Center for Quantum Molecular Sciences, Department of Chemistry, UiT The Arctic University of Norway, N-9307 Tromsø, Norway*

Nilay Hazari − *Department of Chemistry, Yale University, New Haven, Connecticut 06520, United States;* ◉ orcid.org/0000-0001-8337-198X

Complete contact information is available at:
https://pubs.acs.org/10.1021/jacs.0c04695

Author Contributions

[#]C.O. and M.F.O. contributed equally.

Notes

The authors declare no competing financial interest.

REFERENCES

(1) For selected reviews, see: (a) Burkart, M. D.; Hazari, N.; Tway, C. L.; Zeitler, E. L. Opportunities and Challenges for Catalysis in Carbon Dioxide Utilization. *ACS Catal.* **2019**, *9*, 7937. (b) Yang, Y.; Lee, J.-W. Toward Ideal Carbon Dioxide Functionalization. *Chem. Sci.* **2019**, *10*, 3905. (c) Tortajada, A.; Juliá-Hernández, F.; Börjesson, M.; Moragas, T.; Martin, R. Transition-Metal-Catalyzed Carboxylation Reactions with Carbon Dioxide. *Angew. Chem., Int. Ed.* **2018**, *57*, 15948. (d) Yeung, C. Photoredox Catalysis as a Strategy for CO_2 Incorporation: Direct Access to Carboxylic Acids from a Renewable Feedstock. *Angew. Chem., Int. Ed.* **2019**, *58*, 5492. (e) Artz, J.; Müller, T. E.; Thenert, K.; Kleinekorte, J.; Meys, R.; Sternberg, A.; Bardow, A.; Leitner, W. Sustainable Conversion of Carbon Dioxide: An Integrated Review of Catalysis and Life Cycle Assessment. *Chem. Rev.* **2018**, *118*, 434. (f) Cokoja, M.; Bruckmeier, C.; Rieger, B.; Herrmann, W. A.; Kühn, F. E. Transformation of Carbon Dioxide with Homogeneous Transition-Metal Catalysts: A Molecular Solution to a Global Challenge? *Angew. Chem., Int. Ed.* **2011**, *50*, 8510. (g) Huang, K.; Sun, C. L.; Shi, Z.-J. Transition-Metal-Catalyzed C—C Bond Formation through the Fixation of Carbon Dioxide. *Chem. Soc. Rev.* **2011**, *40*, 2435. (h) *Carbon Dioxide as Chemical Feedstock*; Aresta, M., Ed.; Wiley-VCH: Weinheim, Germany, 2010. (i) Sakakura, T.; Choi, J. C.; Yasuda, H. Transformation of Carbon Dioxide. *Chem. Rev.* **2007**, *107*, 2365.

(2) For selected references, see: (a) Sahoo, B.; Bellotti, P.; Juliá-Hernández, F.; Meng, Q. − Y.; Crespi, S.; König, B.; Martin, R. Site-Selective Remote sp³ C—H Carboxylation Enabled by the Merger of Photoredox and Nickel Catalysis. *Chem. - Eur. J.* **2019**, *25*, 9001. (b) Meng, Q. − Y.; Wang, S.; König, B. Carboxylation of Aromatic and Aliphatic Bromides and Triflates with CO_2 by Dual Visible-Light Nickel Catalysis. *Angew. Chem., Int. Ed.* **2017**, *56*, 13426. (c) Juliá-Hernández, F.; Moragas, T.; Cornella, J.; Martin, R. Remote Carboxylation of Halogenated Aliphatic Hydrocarbons with Carbon Dioxide. *Nature* **2017**, *545*, 84. (d) Börjesson, M.; Moragas, T.; Martin, R. Ni-Catalyzed Carboxylation of Unactivated Alkyl Chlorides with CO_2. *J. Am. Chem. Soc.* **2016**, *138*, 7504. (e) Wang, X.; Liu, Y.; Martin, R. Ni-Catalyzed Divergent Cyclization/Carboxylation of Unactivated Primary and Secondary Alkyl Halides with CO_2. *J. Am. Chem. Soc.* **2015**, *137*, 6476. (f) Liu, Y.; Cornella, J.; Martin, R. Ni-Catalyzed Carboxylation of Unactivated Primary Alkyl Bromides and Sulfonates with CO_2. *J. Am. Chem. Soc.* **2014**, *136*, 11212.

(3) For selected reviews on the use of unactivated alkyl electrophiles in cross-coupling reactions, see: (a) Kambe, N.; Iwasaki, T.; Terao, J. Pd-Catalyzed Cross-Coupling Reactions of Alkyl Halides. *Chem. Soc. Rev.*

2011, *40*, 4937. (b) Hu, X. Nickel-Catalyzed Cross-Coupling of Non-Activated Alkyl Halides: A Mechanistic Perspective. *Chem. Sci.* **2011**, *2*, 1867. (c) Jana, R.; Pathak, T. P.; Sigman, M. S. Advances in Transition Metal (Pd,Ni,Fe)-Catalyzed Cross-Coupling Reactions Using Alkyl-Organometallics as Reaction Partners. *Chem. Rev.* **2011**, *111*, 1417.

(4) For excellent authoritative reviews on Ni catalysis, see: (a) Diccianni, J. B.; Diao, T. Mechanisms of Nickel-Catalyzed Cross-Coupling Reactions. *Trends Chem.* **2019**, *1*, 830. (b) Richmond, E.; Moran, J. Recent Advances in Nickel Catalysis Enabled by Stoichiometric Metallic Reducing Agents. *Synthesis* **2018**, *50*, 499. (c) Ananikov, V. P. Nickel: The "Spirited Horse" of Transition Metal Catalysis. *ACS Catal.* **2015**, *5*, 1964. (d) Tasker, S.; Standley, E.; Jamison, T. Recent Advances in Homogeneous Nickel Catalysis. *Nature* **2014**, *509*, 299.

(5) For a recent review on Ni-catalyzed chain-walking reactions, see: Janssen-Müller, D.; Sahoo, B.; Sun, S.-Z.; Martin, R. Tackling Remote sp³ C—H Functionalization via Ni-Catalyzed "Chain-walking" Reactions. *Isr. J. Chem.* **2020**, *60*, 195.

(6) For selected reviews on Ni-catalyzed cross-coupling reactions, including those that make use of phen-type ligands, see: (a) Goldfogel, M. J.; Huang, L.; Weix, D. J. Cross-Electrophile Coupling. In *Nickel Catalysis in Organic Synthesis*; Ogoshi, S., Ed.; Wiley, 2019; pp 183− 222. (b) Gu, J.; Wang, X.; Xue, W.; Gong, H. Nickel-Catalyzed Reductive Coupling of Alkyl Halides with Other Electrophiles: Concept and Mechanistic Considerations. *Org. Chem. Front.* **2015**, *2*, 1411. (c) Hu, X. Nickel-Catalyzed Cross Coupling of Non-Activated Alkyl Halides: A Mechanistic Perspective. *Chem. Sci.* **2011**, *2*, 1867.

(7) (a) García-López, D.; Pavlovic, L.; Hopmann, K. H. To Bind or Not to Bind: Mechanistic Insights into C—CO_2 Bond Formation with Late Transition Metals. *Organometallics* **2020**, *39*, 1339. (b) Obst, M.; Pavlovic, L.; Hopmann, K. H. Carbon-Carbon Bonds with CO_2: Insights from Computational Studies. *J. Organomet. Chem.* **2018**, *864*, 115.

(8) Somerville, R. J.; Martin, R. Relevance of Ni(I) in Catalytic Carboxylation Reactions. In *Nickel Catalysis in Organic Synthesis*; Ogoshi, S., Ed.; Wiley, 2019; pp 285−330.

(9) For a recent example of Ni(I)−*aryl* complexes bearing N-donor ligands, see: Mohadjer Beromi, M.; Brudvig, G. W.; Hazari, N.; Lant, H. M. C.; Mercado, B. Q. Synthesis and Reactivity of Paramagnetic Polypyridyl Ni Complexes Relevant to C(Sp²)−C(Sp³) Coupling Reactions. *Angew. Chem., Int. Ed.* **2019**, *58*, 6094.

(10) Diccianni, J. B.; Hu, C. T.; Diao, T. Insertion of CO_2 Mediated by a (Xantphos)Ni[I]−Alkyl Species. *Angew. Chem., Int. Ed.* **2019**, *58*, 13865.

(11) For examples of CO_2 insertion at PCP and PCN (pincer)Ni(II)−Me complexes, see: (a) Mousa, A. H.; Polukeev, A. V.; Hansson, J.; Wendt, O. F. Carboxylation of the Ni−Me Bond in an Electron-Rich Unsymmetrical PCN Pincer Nickel Complex. *Organometallics* **2020**, *39* (9), 1553. (b) Mousa, A. H.; Bendix, J.; Wendt, O. F. Synthesis, Characterization, and Reactivity of PCN Pincer Nickel Complexes. *Organometallics* **2018**, *37* (15), 2581−2593. (c) Jonasson, K. J.; Wendt, O. F. Synthesis and Characterization of a Family of POCOP Pincer Complexes with Nickel: Reactivity towards CO_2 and Phenylacetylene. *Chem. - Eur. J.* **2014**, *20*, 11894. (d) Schmeier, T. J.; Hazari, N.; Incarvito, C. D.; Raskatov, J. A. Exploring the Reactions of CO_2 with PCP Supported Nickel Complexes. *Chem. Commun.* **2011**, *47*, 1824.

(12) For control experiments using [tBu]Xantphos in the catalytic carboxylation of unactivated alkyl halides, see the Supporting Information.

(13) For reviews on Ni-catalyzed reductive cross-coupling reactions, see: (a) Diccianni, J.; Lin, Q.; Diao, T. Mechanisms of Nickel-Catalyzed Coupling Reactions and Applications in Alkene Functionalization. *Acc. Chem. Res.* **2020**, *53*, 906. (b) Gu, J.; Wang, X.; Xue, W.; Gong, H. Nickel-Catalyzed Reductive Coupling of Alkyl Halides with other Electrophiles: Concept and Mechanistic Considerations. *Org. Chem. Front.* **2015**, *2*, 1411. (c) Weix, J. D. Methods and Mechanisms for Cross-Electrophile Coupling of Csp2 Halides with Alkyl Electrophiles. *Acc. Chem. Res.* **2015**, *48*, 1767. (d) Moragas, T.; Correa, A.; Martin, R. Metal-Catalyzed Reductive Coupling Reactions of Organic Halides with Carbonyl-Type Compounds. *Chem. - Eur. J.* **2014**, *20*, 8242.

(e) Knappke, C. E. I.; Grupe, S.; Gärtner, D.; Corpet, M.; Gosmini, C.; Jacobi von Wangelin, A. Reductive Cross-Coupling Reactions between Two Electrophiles. *Chem. - Eur. J.* **2014**, *20*, 6828.

(14) For the first reports of **L1** complexes, see: (a) Schmittel, M.; Lüning, U.; Meder, M.; Ganz, A.; Michel, C.; Herderich, M. Synthesis of Sterically Encumbered 2,9-Diaryl Substituted Phenanthrolines. Key Building Blocks for the Preparation of Mixed (Bis-Heteroleptic) Phenanthroline Copper(I) Complexes. *Heterocycl. Commun.* **1997**, *3*, 493. (b) Schmittel, M.; Ganz, A. Stable Mixed Phenanthroline Copper(I) Complexes. Key Building Blocks for Supramolecular Coordination Chemistry. *Chem. Commun.* **1997**, 999.

(15) During the course of our studies, a comproportionation route to inner-sphere Ni(I)−halide complexes was reported. See: Zarate, C.; Yang, H.; Bezdek, M. J.; Hesk, D.; Chirik, P. J. Ni(I)−X Complexes Bearing a Bulky α-Diimine Ligand: Synthesis, Structure, and Superior Catalytic Performance in the Hydrogen Isotope Exchange in Pharmaceuticals. *J. Am. Chem. Soc.* **2019**, *141*, 5034.

(16) During the course of our studies, an inner-sphere bromide complex bearing a bulky bipyridine ligand that was obtained via reduction of a Ni(II) complex was reported. See: Lin, Q.; Diao, T. Mechanism of Ni-Catalyzed Reductive 1,2-Dicarbofunctionalization of Alkenes. *J. Am. Chem. Soc.* **2019**, *141*, 17937.

(17) **2-Br** and **L1** were competent as the precatalyst and ligand, respectively, for the chain-walking carboxylation of 2-bromoheptane. See the Supporting Information and ref 2c for details.

(18) It is worth noting that Ni(**L2**)$_2$ was detected when **L2** complexes were employed (see ref 2c). For reactions with **L1**-bearing complexes, unusual [Ni(**L1**)]$_3$ trimers and [Ni(**L4**)]$_4$ tetramers crystallized from the reaction mixtures (see the Supporting Information for details).

(19) Reactions between **1-Cl** or **2-Cl** and neopentylMgBr also form **3**.

(20) (a) Kitiachvili, K. D.; Mindiola, D. J.; Hillhouse, G. L. Preparation of Stable Alkyl Complexes of Ni(I) and Their One-Electron Oxidation to Ni(II) Complex Cations. *J. Am. Chem. Soc.* **2004**, *126*, 10554. (b) Laskowski, C. A.; Bungum, D. J.; Baldwin, S. M.; Del Ciello, S. A.; Iluc, V. M.; Hillhouse, G. L. Synthesis and Reactivity of Two-Coordinate Alkyl and Aryl Complexes of Ni(I). *J. Am. Chem. Soc.* **2013**, *135*, 18272.

(21) For a selection of T-shaped Ni(I) complexes, see: (a) Kogut, E.; Wiencko, H. L.; Zhang, L.; Cordeau, D. E.; Warren, T. H. A Terminal Ni(III)-Imide with Diverse Reactivity Pathways. *J. Am. Chem. Soc.* **2005**, *127*, 11248. (b) Eckert, N. A.; Dinescu, A.; Cundari, T. R.; Holland, P. L. A T-Shaped Three-Coordinate Nickel(I) Carbonyl Complex and the Geometric Preferences of Three-Coordinate d^9 Complexes. *Inorg. Chem.* **2005**, *44*, 7702. (c) Iluc, V. M.; Hillhouse, G. L. Three-Coordinate Nickel Carbene Complexes and Their One-Electron Oxidation Products. *J. Am. Chem. Soc.* **2014**, *136*, 6479.

(22) For information about the geometries of three-coordinate d^9 complexes, see: (a) Alvarez, S. Bonding and Stereochemistry of Three-Coordinated Transition Metal Compounds. *Coord. Chem. Rev.* **1999**, *193−195*, 13. (b) Jean, Y.; Marsden, C. T. *Molecular Orbitals of Transition Metal Complexes*; Oxford University Press, 2005.

(23) (a) Deacon, G. B.; Phillips, R. J. Relationships between the Carbon-Oxygen Stretching Frequencies of Carboxylato Complexes and the Type of Carboxylate Coordination. *Coord. Chem. Rev.* **1980**, *33*, 227. (b) Nara, M.; Torii, H.; Tasumi, M. Correlation between the Vibrational Frequencies of the Carboxylate Group and the Types of Its Coordination to a Metal Ion: An Ab Initio Molecular Orbital Study. *J. Phys. Chem.* **1996**, *100*, 19812.

(24) Hazari, N.; Heimann, J. E. Carbon Dioxide Insertion into Group 9 and 10 Metal-Element σ Bonds. *Inorg. Chem.* **2017**, *56*, 13655.

(25) Sayyed, F. B.; Sakaki, S. The crucial roles of MgCl$_2$ as a non-innocent additive in the Ni-catalyzed carboxylation of benzyl halide with CO$_2$. *Chem. Commun.* **2014**, *50*, 13026.

(26) For an example where the nature of the ligand affects the CO$_2$ insertion pathway, see ref 7.

(27) For selected examples in which MgX$_2$ additives were employed in Ni-catalyzed reductive cross-coupling reactions, see: (a) Ye, Y.; Chen, H.; Yao, K.; Gong, H. Iron-Catalyzed Reductive Vinylation of Tertiary alkyl Oxalates with Activated Vinyl Halides. *Org. Lett.* **2020**, *22*, 2070.

(b) Gao, M.; Sun, D.; Gong, H. Ni-Catalyzed Reductive C−O Bond Arylation of Oxalates Derived from α-Hydroxy Esters with Aryl Halides. *Org. Lett.* **2019**, *21*, 1645. (c) Wang, X.; Ma, G.; Peng, Y.; Pitsch, C. E.; Moll, B. J.; Ly, T. D.; Wang, X.; Gong, H. Ni-Catalyzed Reductive Coupling of Electron-Rich Aryl Iodides with Tertiary Alkyl Halides. *J. Am. Chem. Soc.* **2018**, *140*, 14490. (d) Fujihara, T.; Horimoto, Y.; Mizoe, T.; Sayyed, F. B.; Tani, Y.; Terao, J.; Sakaki, S.; Tsuji, Y. Nickel-Catalyzed Double Carboxylation of Alkynes Employing Carbon Dioxide. *Org. Lett.* **2014**, *16*, 4960. (e) Leon, T.; Correa, A.; Martin, R. Nickel-Catalyzed Direct Carboxylation of Benzyl Halides. *J. Am. Chem. Soc.* **2013**, *135*, 1221.

(28) Charboneau, D. J.; Brudvig, G. W.; Hazari, N.; Lant, H. M. C.; Saydjari, A. K. Development of an Improved System for the Carboxylation of Aryl Halides through Mechanistic Studies. *ACS Catal.* **2019**, *9*, 3228.

Paper VI

Carbon-Carbon Bonds with CO₂: Insights from Computational Studies

M. Obst, Lj. Pavlović,
and K. H. Hopmann

Carbon-carbon bonds with CO_2: Insights from computational studies

Marc Obst [1], Ljiljana Pavlovic [1], Kathrin H. Hopmann[*]

Hylleraas Centre for Quantum Molecular Sciences, Department of Chemistry, University of Tromsø - The Arctic University of Norway, N-9037 Tromsø, Norway

A B S T R A C T

In this mini-review, we provide an overview of recent computational studies on homogeneous transition metal-catalyzed carbon-carbon bond formation with CO_2. We cover substitution and addition reactions involving different metals (mainly Ni, Rh, Cu) and substrates (alkanes, alkenes, alkynes, arenes) with focus on the mechanistic details. The CO_2 insertion step is generally found to be rate-limiting. The reported transition state geometries for C-C bond formation mostly display three-membered cyclic arrangements involving the metal and the two reacting carbon atoms, except for reaction with C_{sp} atoms, where acyclic conformations are observed. Other reported exceptions point to that an interaction of CO_2 with the metal catalyst may not be essential. Several studies suggest that Lewis acid additives could help activating CO_2 during C-C bond formation.

© 2018 The Authors. Published by Elsevier B.V. This is an open access article under the CC BY-NC-ND license (http://creativecommons.org/licenses/by-nc-nd/4.0/).

1. Introduction

CO_2 can be used as a reagent in the synthesis of a variety of chemical building blocks including carbonates, carbamates, carboxylic acids and derivatives (for relevant reviews see Refs. [1—18]). For formation of these molecules, two metal-catalyzed strategies have found widespread use, respectively leading to the formation of C-CO_2 and O/N-CO_2 bonds (Fig. 1).

Rational improvement of CO_2—converting catalysts requires insights into their mechanistic details. Computational studies are often used to understand the activation, selectivity and reaction pathways of homogeneous catalysts. For reactions involving CO_2, relevant computational studies were reviewed in 2012 by both Lin and co-workers [19] and Kühn and co-workers [20]. Both reviews were thematically broad, covering examples of reduction of CO_2 to CO, hydrogenation of CO_2 to formate, reaction of CO_2 with epoxides or alcohols to form carbonates or reaction with carbon-based nucleophiles to form carboxylic acids.

The carbon-carbon (C-C) bond is the most fundamental constituent of organic molecules. In order for CO_2 to become a versatile carbon source in the laboratory, it is essential to design efficient catalysts for C-C bond formation from CO_2. Catalytic strategies typically involve insertion of CO_2 into metal-alkyl or -aryl bonds. Such reactions can be divided into two main types: *i*) Substitution reactions involving alkanes, alkenes, alkynes or arenes as substrates and *ii*) Addition reactions to alkenes or alkynes (Fig. 2).

Here we summarize 16 computational studies (from 2010 and onwards) related to the two transition metal-catalyzed C-C bond formation reactions given in Fig. 2. Particular focus is on the proposed mechanisms and the transition state (TS) geometries at the C-CO_2 bond formation step. On basis of the discussed examples for substitution at C_{sp}, C_{sp2}, C_{sp3} and addition at C_{sp} and C_{sp2}, we identify trends connected to transition metal-catalyzed CO_2 activation and fixation into C-C bonds.

2. Review of computational studies

2.1. Substitution at C_{sp}

Copper: In 2010, Lu and co-workers [21] reported the carboxylative coupling of terminal alkynes and allylic chlorides with CO_2 in the presence of IPr-Cu-Cl (Fig. 3). The details of the reaction were computationally investigated by Yuan and Lin in 2014, employing B3P86 together with PCM (DMF solvent) on the full molecular system [22]. The first step of the proposed mechanism is the base-mediated insertion of the terminal alkyne into IPr-Cu-Cl to form the Cu-acetylide intermediate. This intermediate undergoes a

* Corresponding author.
E-mail address: kathrin.hopmann@uit.no (K.H. Hopmann).
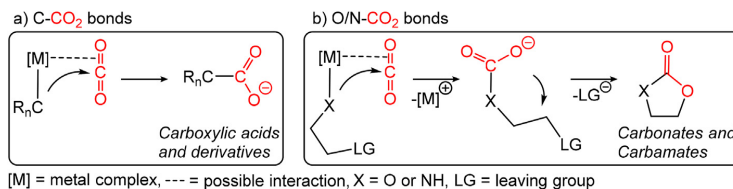[1] These authors contributed equally to this work.

Fig. 1. Two transition metal-catalyzed strategies for the formation of C-CO$_2$ and O/N-CO$_2$ bonds.
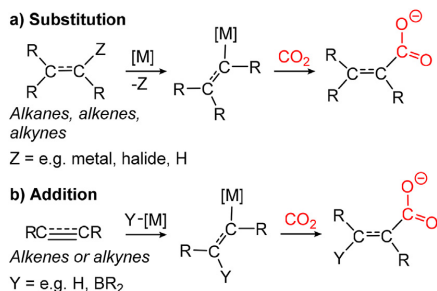

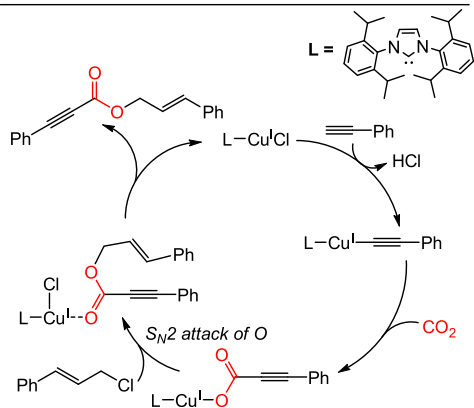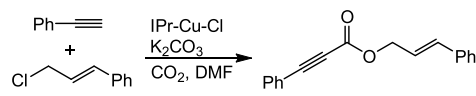**Fig. 2.** Two types of C-CO$_2$ bond formation.

Fig. 3. Mechanism for carboxylative coupling of alkynes and allylic chlorides [21,22].

nucleophilic attack on CO$_2$ with an activation barrier of 18.6 kcal/mol, leading to formation of a Cu-carboxylate. The TS of the CO$_2$ insertion step is pictured in Fig. 4, showing no significant interaction between copper and CO$_2$ (Cu-C$_{CO2}$ distance of 2.94 Å). The third step is rate-determining with a barrier of 24.1 kcal/mol and consists of an SN$_2$-like attack of the carboxylic oxygen on the allylic chloride, resulting in the dissociation of Cl, which then binds to Cu. An oxidative addition of the allylic chloride was excluded. The authors also computed a cross coupling side reaction, which from
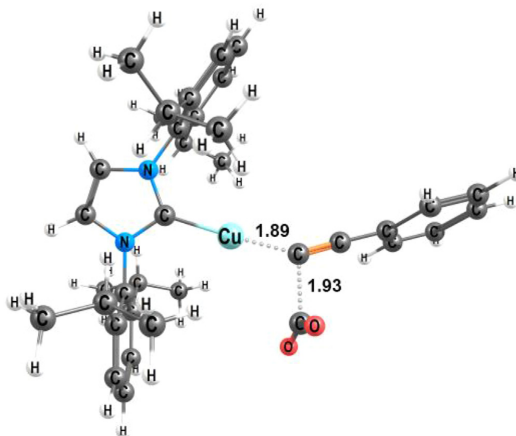
Fig. 4. TS geometry for C$_{sp}$-CO$_2$ bond formation with a Cu-(IPr) complex (distances in Å, coordinates from Ref. [22]).

experiment is known to be competitive. Comparing B3P86 with and without the Grimme empirical dispersion correction D2 [23], the authors concluded that pure B3P86 gives an energetic profile that is in better agreement with experiment.

In 2010, Yu and Zhang reported the Cu-catalyzed C-H bond activation and carboxylation of terminal alkynes [24]. Yang et al. studied the CO$_2$ insertion step of this reaction in 2014 utilizing an NHC ligand possessing two carbenes [25]. Geometries of the full molecular system were optimized with B3LYP in vacuum. The CPCM model (DMF solvent) was employed for computing single point energies of some of the optimized geometries. The authors compared several possible reaction paths, differing with respect to the interaction of CO$_2$ and Cu with the NHC ligand. Their results predict that the Cu species coordinated by both carbenes of the ligand gives the reaction path with the lowest overall barrier (Fig. 5). The associated CO$_2$ insertion TS indicates that CO$_2$ is not interacting with copper (Cu-C$_{CO2}$ distance of 2.84 Å), in line with the observations by Yuan and coworkers (Fig. 4) [22]. The computations also predict formation of a stable off-cycle intermediate with one carbene coordinating to Cu and the other binding to CO$_2$ (**II**, Fig. 5). Analysis of the energies presented in Ref. [25] indicate that **II** is 4.5 kcal/mol lower in energy than the di-coordinated species **I** (Fig. 5). The barrier for formation of **II** via dissociation of a carbene ligand in **I** was not computed, but based on the energy of an intermediate species, it should be above 9.6 kcal/mol (relative to **I**). The barrier for the on-cycle conversion of **I** to **III** via CO$_2$ insertion into the metal-substrate bond was computed to 10.3 kcal/mol (relative to **I**). The barriers appear so similar that formation of **II** should not be ignored, as it may either represent an off-cycle
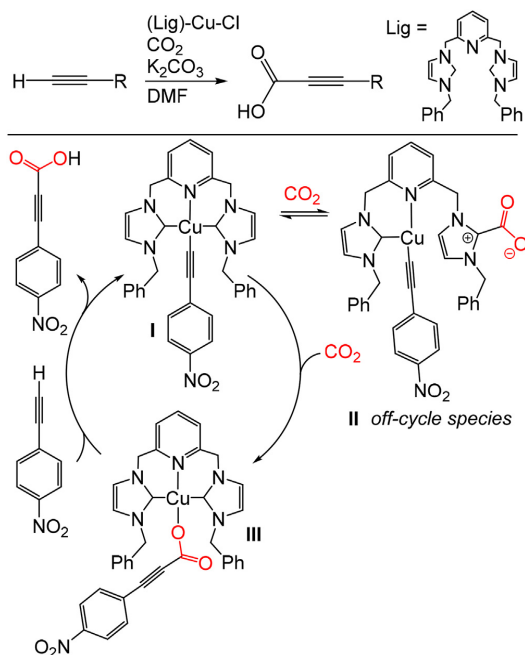
Fig. 5. Proposed mechanism for copper-catalyzed C–H bond activation and carboxylation of terminal alkynes [25].

thermodynamic sink, or the true catalytic species. The latter was excluded by the authors due to the high barrier for insertion of the captured CO_2 of **II** into the metal-substrate bond. However, we recommend to test reaction of an additional *free* CO_2 molecule with **II**, which clearly should be lower in energy than insertion of the captured CO_2. **II** may actually be both an on-cycle species and the resting state of the system.

Copper vs. Silver: In 2017, Velázquez et al. reported a combined experimental and theoretical investigation of the carboxylation of terminal alkynes in presence of NHC-Cu or Ag and a cesium additive (Fig. 7) [26]. Geometry optimizations were performed on the full molecular system under vacuum conditions with B3LYP and the Grimme empirical dispersion correction D3 [27]. The authors concentrated their computational investigation on the CO_2 insertion step of the reaction and found a TS, were the CO_2 is activated by a cesium ion, which is interacting with the sulfonic group of the NHC ligand. Optimized coordinates of the TS were not provided, but the given illustrations indicate that Cu and Ag do not show significant interactions with CO_2. The barriers were similar for the two metals (25.8 kcal/mol for Cu vs. 24.3 kcal/mol for Ag), slightly favouring the Ag complex.

Cu vs Ni vs Rh vs Ir vs Co: In 2016, Vummaleti et al. computed the barrier heights for insertion of CO_2 into different metal-C≡C-Ph complexes [28]. The metals [Cu(I), Ir(I), Ni(II), Rh(I), Co(I)] were bearing COD and IPr ligands [COD = 1,5-cyclooctadiene; IPr = 1,3-bis(isopropyl)-imidazol-2-ylidene]. Geometry optimizations were performed at the BP86 level in vacuum, with single point energy evaluations with M06. The optimized TSs show significantly different distances for the M-C_{alkyl}, C_{alkyl}-C_{CO2}, M-C_{CO2}, and M-O bonds (see Fig. 8 for the Cu-, Ni- and Rh-geometries). The Cu complex shows a C_{alkyl}-C_{CO2} distance of only 1.76 Å, which is

significantly shorter than for the related Cu-catalyzed reactions in Figs. 4 and 6. This may be due to the presence of both a COD and an NHC ligand on copper. The CO_2 molecule is positioned 2.75 Å from the metal, indicating a weak interaction at best. A similar geometry is observed for the rhodium system. In contrast, the nickel complex shows metal-CO_2 interactions involving the O atom, and a weak interaction to C (Fig. 8). The computed barriers for the different complexes showed substantial differences, with Ni(II) giving the highest barrier (45.4 kcal/mol) and Cu(I) displaying the smallest barrier (20.8 kcal/mol, Fig. 9). The poor performance of Ni(II) is in line with related findings for substitution at C_{sp2} (*vide infra*).

2.2. Substitution at C_{sp2}

Nickel: In 2012, Tsuji and co-workers reported Ni-(PPh₃)₂-catalyzed carboxylation of aryl chlorides (Fig. 10) [29]. Sayyed et al. studied this mechanism computationally in 2013 [30]. The calculations were performed on the full molecular system with B3LYP-D2. Geometries were optimized in vacuum, with PCM (DMI solvent) included as a correction to the electronic energy. The calculations predict that the substrate initially undergoes oxidative addition to nickel, followed by Mn-mediated reduction of Ni(II) to Ni(I) (Fig. 10). CO_2 reacts with the Ni(I) species and then forms a bond to the aryl carbon. The barrier for an alternative reaction pathway involving direct reaction of the Ni(II)-complex with CO_2 was considered too high, i.e. Mn-mediated reduction of nickel to Ni(I) is essential for the reaction to occur. The optimized TS shows a cyclic conformation with substantial interactions between Ni and CO_2 at the C_{sp2}-CO_2 bond formation step (Fig. 10).

Rhodium: In 2006, Iwasawa and co-workers reported the Rh(I)-catalyzed carboxylation of aryl- and alkenylboronic esters [31]. Qin et al. provided a computational investigation in 2014 [32]. The DFT functional PBE0 with PCM was employed. The authors examined the Rh-catalyzed carboxylation of arylboronic esters, involving bidentate rhodium ligands with different electronic properties: a phosphine-based ligand [dppp = 1,3-bis(diphenylphosphino) propane] or the diene ligand COD. The computational analysis supported the previously proposed mechanism (Fig. 11): formation of an Rh-Ph intermediate (**I**), which then interacts with CO_2 to form the Rh-OOCPh species (**II**) through a rate-limiting carboxylation step. At the TS, the CO_2 interacts with the rhodium center through the oxygen and carbon atom in a η^2 binding mode (Fig. 12). The formed carboxylate coordinates either in a monodentate (**IIa**) or a bidentate (**IIb**) fashion (Fig. 11). The complex can then undergo
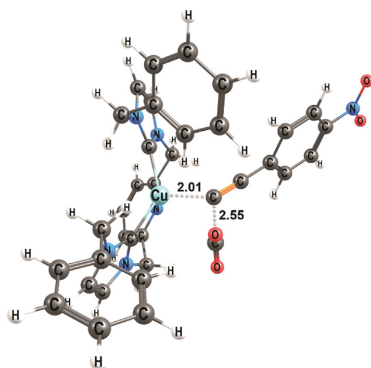

Fig. 6. TS geometry for Cu-catalyzed C_{sp}-CO_2 bond formation (distances in Å, coordinates from Ref. [25]).
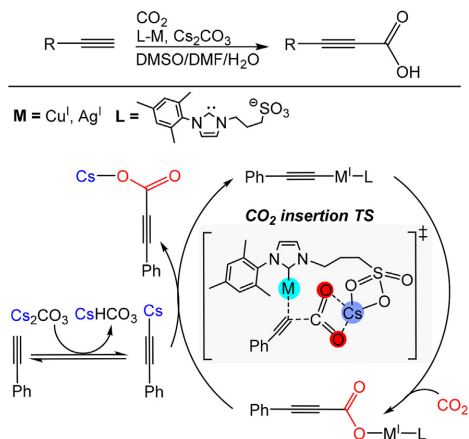
either a direct transmetallation with an arylbororonic ester substrate to form a carboxylated boron species and regenerate **I**, or proceed via a cesium benzoate (Fig. 11).

With dppp as ligand, the computed barrier was 12.7 kcal/mol. It involved a transformation from a square-planar O-(η^1)-bonded CO_2 to a distorted tetrahedral η^2-coordination. With COD as ligand, the barrier was 17.7 kcal/mol. According to the authors, bidentate phosphines are a better choice due to the larger σ-donor/π-acceptor properties compared to COD.

In 2011, Iwasawa and co-workers reported the direct Rh(I)-catalyzed carboxylation of arenes via chelation-assisted C-H bond activation [33] (Fig. 13). Recently, Lv et al. provided a computational study of this reaction [34]. B3LYP and the SMD model (solvent DMA) were employed. The modelled reaction was the carboxylation of 2-phenylpyridine, which in presence of [Rh(coe)$_2$Cl]$_2$, a PMes$_3$ ligand, and a methylmetallic reagent forms the desired *ortho*-carboxylated product, alongside a methylated byproduct. The proposed mechanism (Fig. 13) included C-H oxidative addition, CO_2 insertion into the Rh-C(aryl) bond, transmetallation, and methylation.

The authors considered two possible active species of the catalyst, [Rh(I)-Cl] or [Rh(I)-Me], but found that the latter was more likely, due to a lower barrier for the reductive elimination step. The analysis also revealed that AlMe$_2$(OMe) may act as a Lewis acid, which facilitates the rate-limiting CO_2 insertion step (Fig. 14). For C-C bond formation in the absence of AlMe$_2$(OMe), the barrier was higher in energy by 6.2 kcal/mol. According to the authors, a favorable interaction between aluminum and CO_2 could make the latter more electrophilic and facilitate its insertion. A possible interaction between ZnMe$_2$ and CO_2 was excluded, as it made both CO_2 coordination and insertion highly disfavored.

Copper: In 2008, Hou and co-workers reported the carboxylation of aryl- and alkenylboronic esters with CO_2 in the presence of IPr-Cu-Cl [35]. Dang et al. investigated this reaction computationally in 2010 [36]. Calculations were performed with B3LYP on a truncated molecular system with the 1,3-diisopropylphenyl groups of the IPr ligand replaced with methyl groups. Optimizations were performed in vacuum, with PCM (THF solvent) single-point
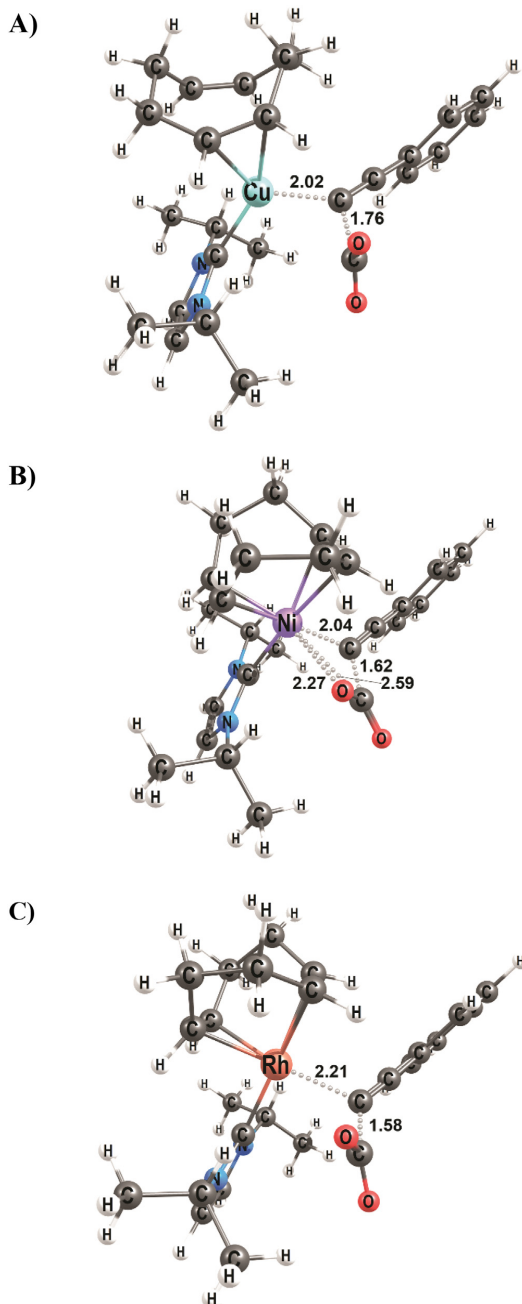
Fig. 8. C_{sp}-CO_2 bond forming TS with metal-(COD)(IPr) complexes, A) Cu(I), B) Ni(II), C) Rh(I) (distances in Å, from coordinates given in Ref. [28]).
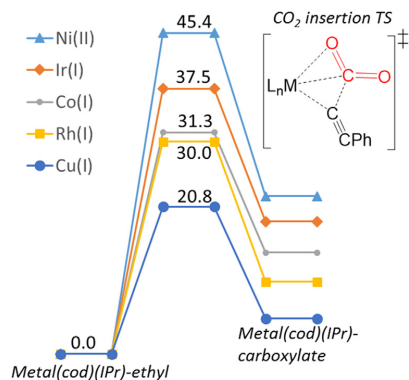
Fig. 9. Computed barriers for C_{sp}-CO_2 bond formation with five metal-(COD)(IPr) complexes (adapted from Ref. [28]).

calculations.

The reaction (Fig. 15) occurs in three steps: the base-mediated formation of the Cu-aryl intermediate, the rate-determining insertion of CO_2 (occurring via a three-membered cyclic TS, Fig. 16), and the regeneration of the active species. The barriers for CO_2 insertion were 25.5 kcal/mol for 4-nitrobenzene and 24.3 kcal/mol for N,N-dimethyl-4-aminobenzene. The authors evaluated the effect of charge on the barrier of the CO_2 insertion and found that electron donating ligands lower the barrier. In addition, they compared CO_2 insertion into Cu-C_{sp3}, Cu-C_{sp2} and Cu-C_{sp} bonds for ethyl derivates and found that the barrier is decreasing in the order $C_{sp} > C_{sp3} > C_{sp2}$.

2.3. Substitution at C_{sp3}

Rhodium: In 2011, Ostapowicz et al. reported a computational study on the insertion of CO_2 into the rhodium-ethyl bond of 38 different pincer complexes [37]. The DFT functional B97-D was employed in geometry optimizations and frequency calculations. The computational analysis focused on the interaction between CO_2 and the Rh-pincer complexes prior to insertion, and on the TS for the C-C bond formation step leading to the carboxylate complex. Different binding modes of the CO_2 to the metal center were observed (Fig. 17).

In 30 complexes, the CO_2 molecule coordinated to the metal center through the carbon atom in an η^1-fashion. Only one complex had an η^2-coordinated CO_2 through the C=O bond, while seven complexes show negligible interactions between rhodium and CO_2, with the distances greater than 3.2 Å.

The insertion of CO_2 into the Rh-C bond occurs through a three-membered cyclic TS between Rh, alkyl and CO_2, where the oxygen atom of CO_2 does not interact with the metal (Fig. 18). The activation barriers were calculated as the difference between the energies of the CO_2 adducts and the TSs and their values varied broadly, from 4.0 to 47.3 kcal/mol. Some complexes, e.g. an anionic Rh-pincer-ethyl complex (Fig. 19), showed strong binding to CO_2, yet very low activation barriers for the CO_2 insertion step, implying that no correlation between the calculated binding energies and insertion barriers could be observed. Interestingly, certain complexes did not show any ability to bind CO_2 but still had moderate insertion barriers, implying that pre-coordination of CO_2 to the metal center is not an essential requirement for this reaction. The authors concluded that the nucleophilicity of the alkyl chain is a main factor that affects the heights of the insertion barriers.

Nickel: In 2013, Martin and co-workers reported the Ni-catalyzed carboxylation of a benzyl halide [38]. Efficient transformation was dependent on the presence of Zn and $MgCl_2$. It was proposed that an Ni(I) intermediate is involved (Fig. 20). Sakaki and co-workers studied the putative pathway computationally in 2014 [39]. The mechanism is very similar to the C_{sp2} case (Fig. 10), but involves an $MgCl_2$ molecule, which interacts with CO_2 (Fig. 20, right). Calculations were performed at the B3LYP-D2 level of theory on the full molecular system, with geometries optimized in vacuum. Single point energy calculations included IEFPCM (DMF solvent). The study concluded that $MgCl_2$ plays a crucial role during the mechanism in activating CO_2. In absence of $MgCl_2$, the C-CO_2 bond formation barrier is computed to be 12 kcal/mol higher.

2.4. Addition at C_{sp}

Copper: In 2011, Tsuji and co-workers [40] reported the Cu-catalyzed hydrocarboxylation of alkynes with hydrosilanes (Fig. 21). The mechanism of the reaction was investigated in 2012
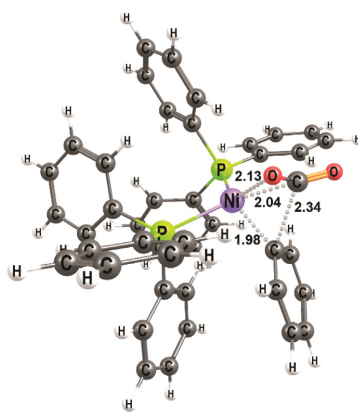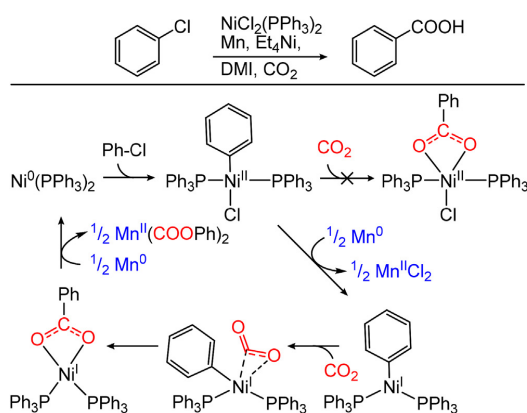

Fig. 10. Left: Ni-catalyzed carboxylation of aryl chloride and proposed mechanism [29,30]. Right: Optimized geometry for the CO_2 insertion TS of Ni(PPh$_3$)$_2$-mediated carboxylation of an arene (distances in Å, based on coordinates in Ref. [30]).
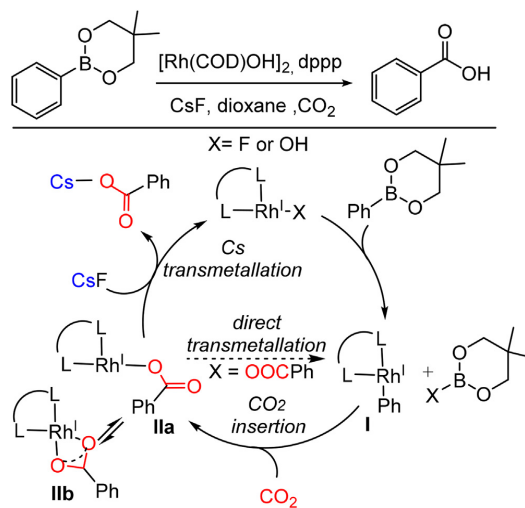
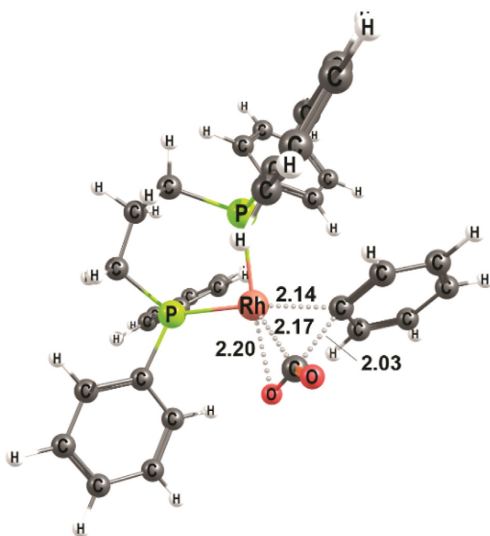**Fig. 11.** Rh(dppp)-catalyzed carboxylation of alkyl-boronic esters and proposed mechanism (based on [32]).

Fig. 13. Direct Rh(I)-catalyzed carboxylation of arenes with CO_2 and proposed mechanism (based on [33,34]).

Fig. 12. C_{sp2}-CO_2 bond forming TS with a Rh-(dppp) complex (distances in Å, based on coordinates from Ref. [32]).
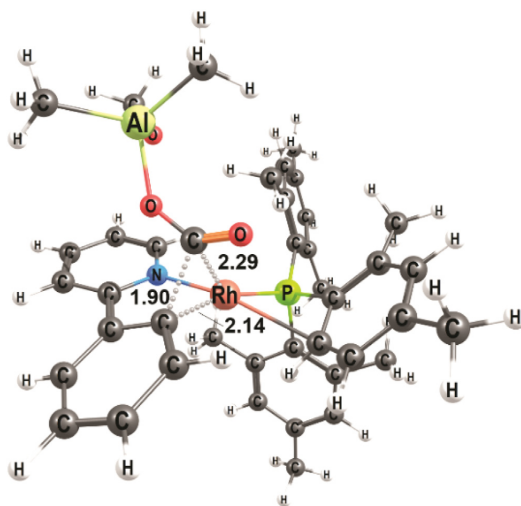
Fig. 14. Rh/Al-catalyzed carboxylation of 2-phenylpyridine (distances in Å, coordinates from Ref. [34]).

by Wang et al. [41] with emphasis on the regioselectivity of asymmetric alkynes, and in 2013 by Fan et al. [42], with focus on the full reaction cycle including putative side reactions. Different NHC ligands were employed, matching the experimental setup for the studied substrates. Both groups optimized geometries with B3LYP in vacuum. Energies were calculated with MP2 (Wang) and B3LYP (Fan) and PCM (Wang: *n*-heptane, Fan:1,4-dioxane solvent) was included. Both groups truncated the system by replacing the 1,3,5-trimethylphenyl groups of the NHC with methyl groups.

The computed reaction path has three major steps (Fig. 21). First

the insertion of the alkyne into the (NHC)-Cu-H species, forming an alkenyl, second the insertion of the CO_2 into the Cu-C bond (Fig. 22) and third the regeneration of the active species via reaction with a hydrosilane. Wang et al. working on asymmetric alkynes, found that the regioselectivity is determined by first step of the reaction, the insertion of the alkyne into (NHC)-Cu-H. While this step is not rate-determining for the overall reaction, it is decisive for the selectivity due to its irreversibility. The authors calculated the barrier of the first step for three alkynes, observing similar preferred regioisomers. In Wang's calculations, the insertion of CO_2
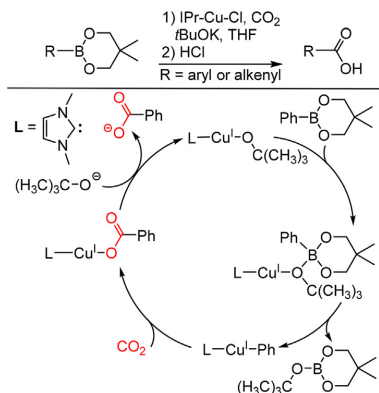
Fig. 15. Proposed mechanism for Cu-catalyzed carboxylation of arylboronate esters with CO_2 (based on [35,36]).
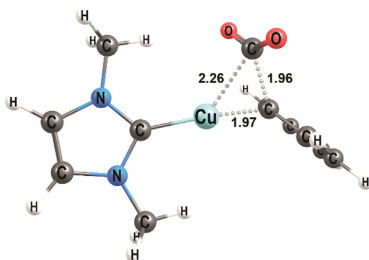

Fig. 16. TS for Cu-catalyzed carboxylation of aryl-boronate esters (distances in Å, coordinates from Ref. [36]).

Fig. 17. Interaction modes of CO_2 with metal-pincer complexes prior to CO_2 insertion [adapted from Ref. [37]].

Fig. 18. Schematic representation of the CO_2 insertion into Rh(I)-pincer-ethyl complexes [adapted from Ref. [37]].

is rate determining [41], whereas Fan predicted it to be the regeneration of the catalyst [42]. In addition to the alkyne hydrocarboxylation, Fan et al. investigated three potential side reactions: silacarboxylation of alkynes, hydrosilylation of alkynes, and hydrosilylation of CO_2. None of these is observed in experiment. It was concluded that silacarboxylation is endergonic and hydrosilylation of alkynes has an inaccessibly high reaction barrier. Hydrosilylation of CO_2 appears feasible based on the computed energies, but was suggested to be unlikely to occur, as CO_2 insertion into a Cu-hydride is heterogeneous in nature compared to homogeneous insertion of an alkyne into Cu-H [42].

2.5. Addition at C_{sp2}

Rhodium: In 2012, Ostapowitz et al. reported a computational investigation of a hypothetical Rh-catalyzed hydrocarboxylation of ethene with CO_2 and H_2 [43]. From their previous investigation [37], three Rh-pincer complexes with different electronic properties were chosen as potential catalysts (Fig. 23). The functional B97-D was employed. In the proposed mechanism (Fig. 24), a rhodium hydride species was used as a starting point. The insertion of ethene gives a Rh-alkyl intermediate, which interacts with CO_2 through a three-membered cyclic TS (Fig. 25) to form a carboxylate complex. The activation barrier for the C-CO_2 bond formation step of the anionic complex **C** was found to be 12.3 kcal/mol and for the corresponding complexes **A** and **B**, 24.5 kcal/mol and 36.1 kcal/mol, respectively. Subsequently, the hydrogenolytic cleavage of the
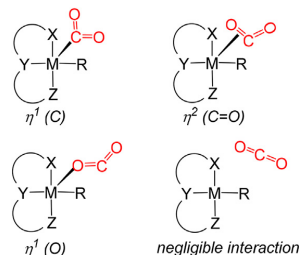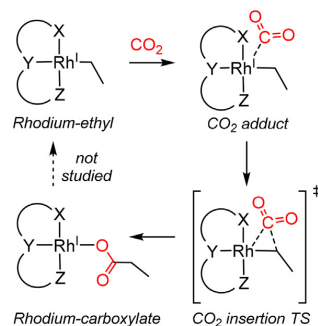
carboxylate complex leads to the carboxylic acid (Fig. 24). The authors found four possible pathways for the hydrogenolysis: i) a σ-bond metathesis via a four-membered or ii) six-membered transition state, iii) an exchange of the carboxylate for H_2 followed by heterolytic cleavage, and iv) a classical oxidative addition/reductive elimination. The computed energy profile showed that each of the three complexes (**A-C**, Fig. 23) gave different hydrogenolysis pathways, which was attributed to the different electronic properties of the pincer ligands. The σ-bond metathesis via a six-membered TS was preferred for complex **A**. For **B**, only a pathway via oxidative addition of H_2 was found. For **C**, a σ-bond metathesis pathway was not located and it was concluded that the carboxylate may be replaced by H_2, followed by heterolytic H_2 cleavage.

From the energy profiles, the anionic complex **C** was proposed to be the most promising candidate, with stable intermediates and overall barriers below 13 kcal/mol. The enhanced electron density at the metal center of **C** leads to a very nucleophilic alkyl intermediate that can easily interact with the electrophilic CO_2. The authors concluded that an electron-rich rhodium center is important for successful hydrocarboxylation and prevention of the major competing reaction, the hydrogenation of olefins.

Nickel: In 2008, Rovis and co-workers reported a seminal study on nickel-catalyzed hydrocarboxylation of substituted styrenes [44] (Fig. 26). The details of this reaction were studied computationally by Yuan and Lin in 2014 [45]. Calculations were performed on the full molecular model with B3LYP and a PCM solvent model. The work compared two mechanisms: an oxidative coupling mechanism and a nickel-hydride pathway (Fig. 26). Both mechanisms set out from a Ni(DBU)$_2$-CO_2 species. In the oxidative coupling, reaction with styrene leads to formation of an
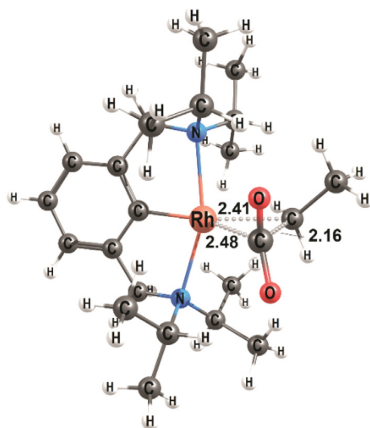
Fig. 19. CO_2 insertion TS with an anionic Rh-pincer-ethyl complex (distances in Å, coordinates from Ref. [37]).

Fig. 21. Mechanism for the copper-catalyzed hydrocarboxylation of alkynes (adapted from Refs. [41,42]).

energetically low-lying metallacycle species. According to the authors this was unlikely to take place in reality, as it would result in a too high barrier for the hydrocarboxylation reaction. The metallacycle mechanism also predicts carboxylation of the styrene β-carbon to be energetically preferred, in disagreement with experiment [44]. The nickel-hydride mechanism gave a reasonable barrier (but only if it is assumed that formation of a metallacycle can be avoided) and the correct regioselectivity, resulting in the α-carboxylated product. The overall barrier for the Ni-H mechanism was 19.8 kcal/mol relative to a Ni(DBU)$_2$-CO$_2$ species, with hydride transfer to the β-carbon and subsequent carboxylation of the α-carbon exhibiting identical barriers. At the carboxylation TS, the CO$_2$ molecule interacts both with Ni and the Zn additive (Fig. 27). When the computational protocol was augmented with the empirical dispersion corrections D3, formation of the metallacycle was strongly preferred, but the authors considered this an incorrect result. In our opinion, this system deserves additional theoretical

and experimental studies to elucidate if a metallacycle intermediate maybe be formed, possibly as an off-cycle species to the nickel-hydride pathway.

Palladium: In 2015, Wu and co-workers reported a computational investigation of the insertion of CO$_2$ into a (PSiP) palladium allyl bond to form β,γ−unsaturated carboxylic acids [46], originally reported by Takaya and Iwasawa [47]. The functional M06 was employed for the calculations, with the IEFPCM model (solvent DMF) added as single point calculations. In the proposed mechanism (Fig. 28), a palladium hydride intermediate is formed in the presence of AlEt$_3$. Next, insertion of allene forms the η^1-allyl palladium complex, which then interacts with CO$_2$ to form a
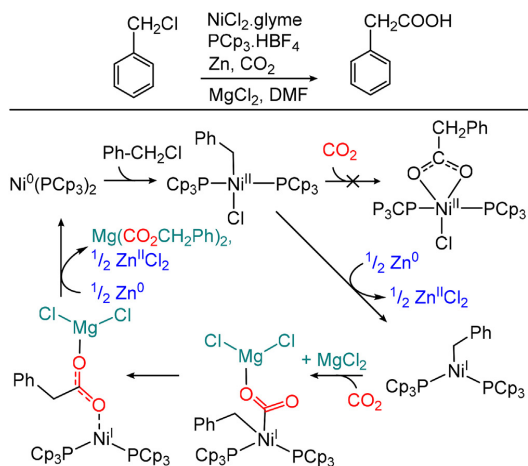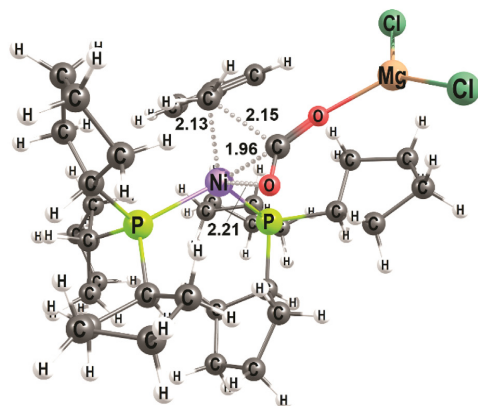

Fig. 20. Left: Ni-catalyzed carboxylation of benzyl chloride and proposed mechanism [38,39]. MgCl$_2$ accelerates the CO$_2$ insertion. Right: Optimized geometry for the CO$_2$ insertion step (distances in Å, based on coordinates in Ref. [38]).

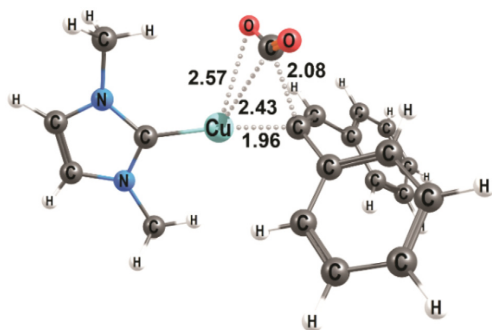**Fig. 22.** CO_2 insertion TS in the Cu-catalyzed hydrocarboxylation of a symmetrical alkyne (distances in Å, based on coordinates in Ref. [42]).
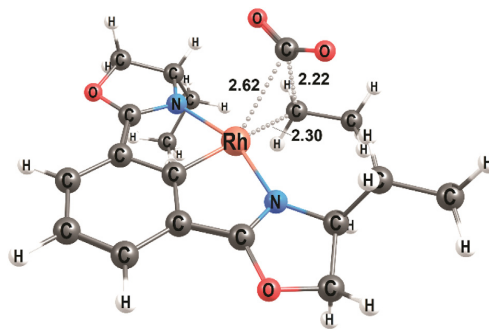

Fig. 25. CO_2 insertion TS in the Rh-catalyzed hydrocarboxylation of ethene (complex **C**, distances in Å, figure prepared from optimized coordinates in Ref. [43]).
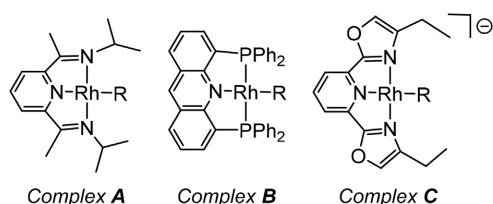

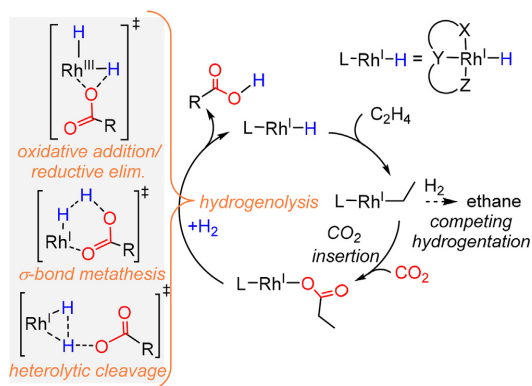**Fig. 23.** Rh-catalysts employed in the theoretical study of a hypothetical hydro-carboxylation reaction [43].

Fig. 24. Proposed mechanism for the direct hydrocarboxylation of ethene with CO_2 and H_2 (based on [43]).

palladium—carboxylate intermediate. Finally, a transmetallation and β-H-elimination regenerates the palladium hydride.

Three possible CO_2 insertion modes were considered: *i*) a direct insertion of CO_2 into the Pd-C bond (leading to carboxylation of the terminal carbon), *ii*) a metallo-ene mode, where the substituted carbon of the double bond reacts with CO_2 via a six-membered TS and *iii*) an S_E2 type reaction, which lacks the CO_2-Pd interaction seen in the metallo-ene mode. The metallo-ene mode (Figs. 28 and 29) was found to be most favorable, with an activation barrier of 21.1 kcal/mol. The computed results were in agreement with the major product observed in experiments. It can be noted that there

exist several earlier mechanistic studies on Pd-catalyzed CO_2 insertion into allylic bonds [48], for a detailed discussion of these see Ref. [19].

Copper: In 2016, Popp and co-workers reported a regioselective copper-catalyzed boracarboxylation of styrenes with CO_2 and B_2pin_2 [49]. The details of the reaction and the effect of the ligands were investigated by Lv et al. in 2017 [50] (Fig. 30). The calculations were performed on full molecular systems with B3LYP in vacuum. Single point energies were acquired with M06 and a SMD model (THF solvent). Icy-Cu-Bpin was suggested as the active species, and the results show a clear preference for the addition of Cu at the α-carbon (barrier of 11.1 kcal/mol vs 22.1 kcal/mol for the β-carbon). The rate-limiting step is the insertion of the CO_2 (barrier of 20.1 kcal/mol), which occurs through a three-membered cyclic TS involving Cu and the two reacting carbon atoms (Fig. 31). Additionally, the authors compared several ligands and concluded that for NHC and biphosphine ligands, the reactivity is determined by the bulkiness and the electronic effects, while for monophosphine ligands, the electron donation ability is dominant.

3. Trends

From the discussed computational studies on C-CO_2 bond formation, some trends can be noted. It should be remembered, however, that due to the medium number of systems included here (18, Table 1) it is not possible to identify such trends with certainty.

Metal-CO_2 interactions and TS geometries: CO_2 is an inert molecule, and it may be expected that its participation in C-C bond formation requires activation of CO_2 by the involved metal catalysts. Such an activation would be expected to occur through direct interactions of CO_2 and the metal. However, the examples discussed here display a variety of different scenarios, ranging from strong metal-CO_2 interactions to no interactions at all. For most of the systems, the overall geometric configuration of the TS is fairly similar, showing three-membered cyclic arrangements involving the metal, and the two reacting carbon atoms (Fig. 32A), where CO_2 interacts with the metal through the C atom (Figs. 8, 14, 16, 19, 25 and 27) or through both C and O (Figs. 10, 12, 20 and 22). At the TS, the CO_2 molecule is typically bend, with angles of 148° down to 117° and exhibits elongated C-O bond lengths (1.20—1.30 Å, Table 1), compared to a free CO_2 molecule (O-C-O 180°, C-O 1.16 Å) [51]. Some trends in interactions and geometries can be observed for the different metals:

- For copper catalysts, CO_2 interacts strongly with the metal and forms three-membered cyclic TSs during bond formation to C_{sp3}
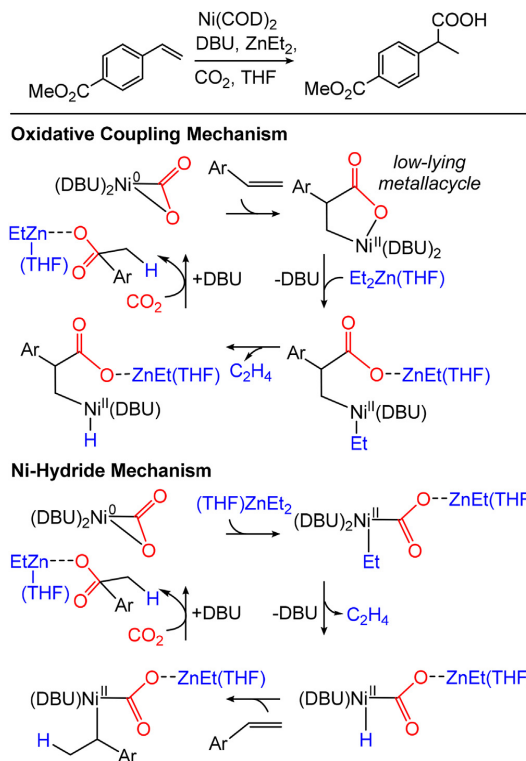
Fig. 26. Ni-catalyzed hydrocarboxylation of styrenes [44] and studied mechanisms [45] (drawn with carboxylation of the α-carbon).
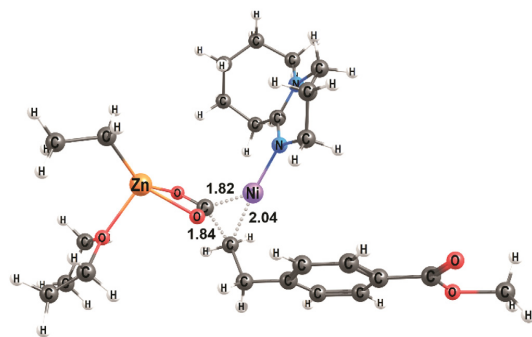

Fig. 28. Pd-catalyzed hydrocarboxylation of an allene with CO_2 and proposed metallo-ene mechanism [46].

Fig. 27. TS geometry for Ni/Zn-mediated carboxylation of a styrene (distances in Å, coordinates from Ref. [45]).
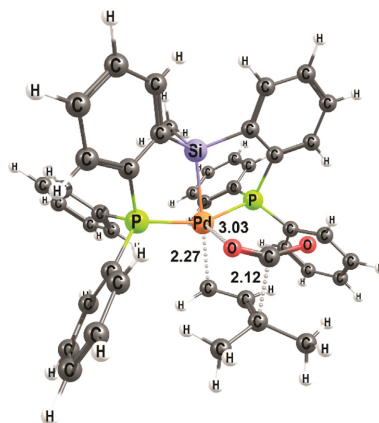
Fig. 29. TS geometry for Pd-catalyzed carboxylation of an allene (distances in Å, coordinates in Ref. [46]).

and C_{sp2} atoms [19,36,41,50], but not for reaction with C_{sp}, where no CO_2-metal interaction is seen [22,25,28] (Figs. 4, 6, 8), resulting in an acyclic TS (Fig. 32B). Based on the Cu-CO_2 bond lengths at the TS (Table 1), it is concluded that the strength of the interaction of CO_2 with Cu depends on the type of nucleophile and has the order $C_{sp3} > C_{sp2} \gg C_{sp}$.

• For nickel-based systems, CO_2 coordination to the metal prior to the carboxylation step may be observed (Figs. 10, 20 and 26)
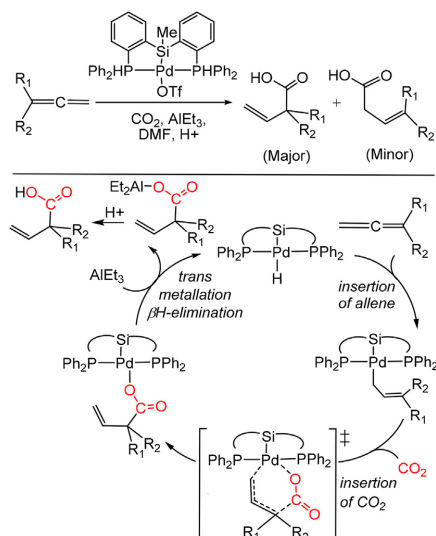
[30,39,45]. The C–C bond formation involves three-membered cyclic TSs, with binding of CO_2 to the metal through both C and O (Figs. 8, 10 and 20) [22,28,30]. If another metal additive interacts with O, only the C-atom may interact with nickel (Fig. 27) [39]. It can be noted that at least one exception has been reported, proposing no interaction of CO_2 with nickel [52].

• For rhodium, CO_2 interaction with the metal may occur prior to the C–C bond formation TS, however, the strength of such an interaction does not correlate with subsequent barriers [37]. Based on the limited data for rhodium, insertion of CO_2 into a Rh-C_{sp} bond involves no Rh-CO_2 interaction (Fig. 8) [28], as also observed for Cu. Insertion into Rh-C_{sp2} bonds occurs in a η^2-fashion, where both C and O atoms coordinate to the metal
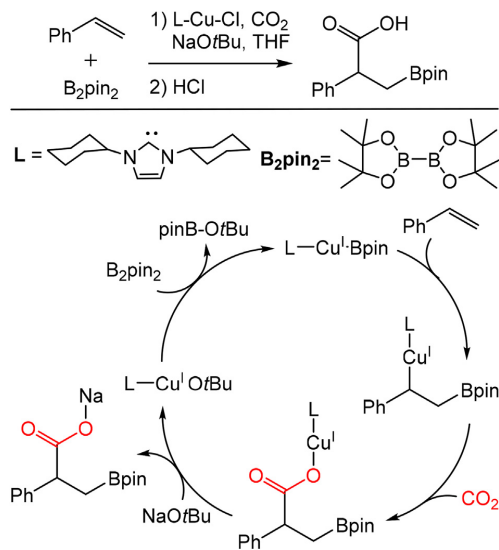
Fig. 30. Mechanism for the copper-catalyzed boracarboxylation of a styrene (adapted from Ref. [50]).

Fig. 31. CO_2 insertion TS in the Cu-catalyzed boracarboxylation of styrene (distances in Å, coordinates from Ref. [50]).

Fig. 32. Trends in TS geometries for C-CO_2 bond formation (references in brackets). Most studies report **A**, except for bonding to C_{sp}, where **B** is reported. **C** has been proposed a few times and should be tested more widely.

(Fig. 12) [32]. Insertion into a Rh-C_{sp3} bond takes place through a three-membered cyclic TS, where CO_2 interacts with Rh only via the carbon atom [37,43] (Figs. 19 and 25). However, it can be noted that in a recent investigation of Rh-catalyzed hydro-carboxylation with CO_2, we showed that during C_{sp3}-CO_2 bond formation, CO_2 interacts neither with rhodium nor with a zinc additive, but prefers to remain unbound and to perform a back-attack on the substrate [53] (Fig. 32C). Given that a cyclic TS conformation as shown in Fig. 32A generally may be expected, it is not certain that all computational studies evaluated acyclic conformations such as Fig. 32C. We recommend to always evaluate multiple TS geometries for C-CO_2 bond formation to ensure that the preferred interaction mode is identified. It is also interesting to note that the acyclic conformation indicates that the metal plays no role in the activation of CO_2, but only in the activation of the nucleophile.

Energetic considerations: In the discussed examples, the CO_2 insertion is generally rate-limiting [28,30,32,34,36,41]. It is not possible to conclude that one metal provides lowest barriers, however, it appears that Cu(I) generally gives feasible barriers, whereas Ni(II) may not be good for C-C bond formation with CO_2 [28,30,39]. All of the presented Cu-complexes use NHC ligands but as Lv et al. indicated, other ligands, like e.g. phosphine, can also yield low activation barriers [50]. Despite the good performance of NHC ligands, the interaction of CO_2 with free carbenes can lead to energetically low-lying off-cycle intermediates [45]. For rhodium, bidentate phosphine ligands appear to give lower barriers than COD [32], and anionic pincer ligands appear better than neutral ligands [43].

Several studies suggest that Lewis acid additives (e.g. Al, Mg) through interaction with CO_2 may reduce the barrier for C-C bond formation (Figs. 14 and 20) [34,39]. An interaction with Zn may also occur [35,45], but this may not be beneficial [35].

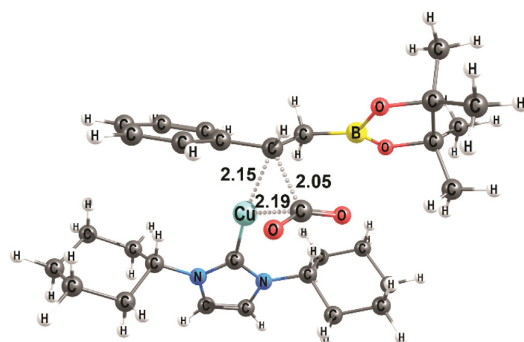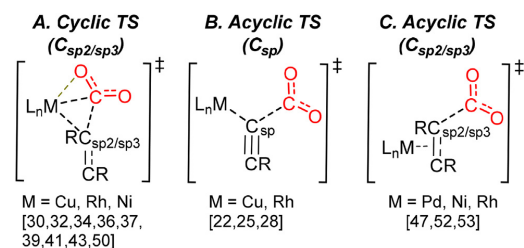**Computational protocols:** All studies reviewed here employed DFT, which provides a good compromise between speed and accuracy, when computing organometallic species. The feasibility of DFT is reflected by the fact that the majority of studies reported calculations on full molecular systems, i.e. without truncating the catalyst or substrate [22,25,26,30,45,50]. However, surprisingly often, geometry optimizations were done in vacuum, and solvent corrections were only included to the energy [25,27,28,30,36,39,41,42,50]. Most studies added dispersion corrections (via a Grimme correction [23] or via a functional that is parametrized to reproduce dispersion, e.g. M06 [54]) [26,28,30,39,43,50], but it can be noted that two studies concluded that dispersion corrections gave results that are in disagreement with experiment [22,45]. This is not in line with the general experience in the field, which shows that dispersion corrections provide more accurate reaction energies [55]. We suggest that if agreement with experiment is poor, it may point to that the mechanism occurs in a different manner than what was computed. For example, if computations predict a stable off-cycle species, then rather than ascribing this to incorrect predictions by the computational protocol [45], it should be considered if an alternative mechanism may be able to incorporate this state [56].

4. Conclusions

We have reviewed computational studies that investigated transition metal-catalyzed C-C bond formation with CO_2. Although the overall mechanisms are dependent on the substrate at hand, the reported TS geometries for the CO_2 insertion steps show similar features, mostly displaying three-membered cyclic rings.

Table 1
Geometrical parameters of reported transition states for C-CO_2 bond formation.

	Metal-complex at TS	Reaction with	C-O_A Å	C-O_B Å	O-C-O °	C_{Alkyl}-CO_2 Å	M-C_{Alkyl} Å	M-C_{CO2} Å	M-O_{CO2} Å	Ref.
Cu	Cu(I)-NHC	C_{sp}	1.20	1.20	145	1.93	1.89	2.94	3.41	[22]
	Cu(I)-NHC(2 carbenes)	C_{sp}	1.20	1.21	145	1.93	2.01	2.84	3.26	[25]
	Cu(I)-NHC-COD	C_{sp}	1.22	1.23	140	1.76	2.02	2.75	3.05	[28]
	Cu(I)-NHC-SO₃/Cs	C_{sp}	NA[a]	NA	NA	1.83	1.93	NA	NA	[26]
	Cu(I)-NHC	C_{sp2}	1.19	1.21	146	2.08	1.96	2.43	2.57	[19]
	Cu(I)-NHC	C_{sp2}	1.20	1.22	142	1.95	1.97	2.34	2.56	[41]
	Cu(I)-NHC	C_{sp2}	1.21	1.22	142	1.96	1.97	2.26	2.66	[36]
	Cu(I)-NHC	C_{sp3}	1.22	1.22	140	2.05	2.15	2.19	2.57	[50]
Ni	Ni(II)-NHC-COD	C_{sp}	1.22	1.27[b]	134	1.62	2.04	2.59	2.27	[28]
	Ni(I)-(PPh₃)₂	C_{sp2}	1.20	1.24	143	2.32	1.98	2.04	2.13	[30]
	Ni(I)-(PCp₃)₂/MgCl₂	C_{sp3}	1.24	1.25[b]	133	2.15	2.13	1.96	2.21 (Ni-O) 1.94 (Mg-O)	[39]
	Ni(II)-DBU/Zn(Et)(THF)	C_{sp3}	1.30[b]	1.31[b]	117[c]	1.84	2.04	1.82	2.67 (Ni-O) 2.08 (Zn-O)	[45]
Rh	Rh(I)-NHC-COD	C_{sp}	1.24	1.26	133	1.58	2.21	2.87	2.89	[28]
	Rh(I)-dppp	C_{sp2}	1.20	1.25	141	2.03	2.14	2.17	2.20	[32]
	Rh(I)-PMes₃/AlMe₂OMe	C_{sp2}	1.21	1.27[b]	134	1.90	2.14	2.29	2.86 (Rh-O) 1.91 (Al-O)	[34]
	Rh(I)-pincer (-)	C_{sp3}	1.22	1.22	141	2.22	2.30	2.62	3.18	[43]
	Rh(I)-pincer (-)	C_{sp3}	1.23	1.23	134	2.16	2.41	2.48	3.06	[37]
Pd	Pd(II)-PSiP	C_{sp2}	1.20	1.20	148	2.12	3.15	3.73	3.03	[47]

[a] NA = not available.
[b] Elongated due to M-O-C_{CO2} interaction, where M = Zn, Mg, Al or Ni.
[c] Both O of CO_2 coordinated to Zn.

Exceptions are reactions with C_{sp} atoms, where acyclic TS geometries are reported, where no metal-CO_2 interactions are observed. We propose that also for reaction with $C_{sp2/sp3}$ atoms, acyclic TS geometries should be evaluated more widely. The insights discussed here deepen the understanding of C-CO_2 bond formation and may be relevant for designing novel CO_2-incorporation reactions.

Competing interests

The authors declare no competing interests.

Acknowledgements

References

[1] Q.-W. Song, Z.-H. Zhou, L.-N. He, Green Chem. 19 (2017) 3707—3728.
[2] X.-F. Wu, F. Zheng, Top. Curr. Chem. (Z) 375 (2017) 4.
[3] L. Zhang, Z. Hou, Curr. Opin. Green Sustain. Chem. 3 (2017) 17—21.
[4] J. Vaitla, Y. Guttormsen, J. Mannisto, A. Nova, T. Repo, A. Bayer, K.H. Hopmann, ACS Catal. 7 (2017) 7231—7244.
[5] M. Börjesson, T. Moragas, D. Gallego, R. Martin, ACS Catal. 6 (2016) 6739—6749.
[6] R. Hua, S. Roy, in: I. Karamé (Ed.), Recent Advances in Organocatalysis, InTech, 2016, https://doi.org/10.5772/63096.
[7] E. Kirillov, J.-F. Carpentier, E. Bunel, Dalton Trans. 44 (2015) 16212—16223.
[8] Q. Liu, L. Wu, R. Jackstell, M. Beller, Nat. Commun. 6 (2015) 5933.
[9] D. Yu, S.P. Teong, Y. Zhang, Coord. Chem. Rev. 293 (2015) 279—291.
[10] A.-H. Liu, B. Yu, L.-N. He, Greenhouse gases, Sci. Technol. 5 (2015) 17—33.
[11] M. Ian Childers, J.M. Longo, N.J. Van Zee, A.M. LaPointe, G.W. Coates, Chem. Rev. 114 (2014) 8129—8152.
[12] S. Pulla, C.M. Felton, P. Ramidi, Y. Gartia, N. Ali, U.B. Nasini, A. Ghosh, J. CO₂ Util. 2 (2013) 49—57.
[13] N. Kielland, C.J. Whiteoak, A.W. Kleij, Adv. Synth. Catal. 355 (2013) 2115—2138.
[14] X.-B. Lu, D.J. Darensbourg, Chem. Soc. Rev. 41 (2012) 1462—1484.
[15] Y. Tsuji, F. Fujihara, Chem. Commun. 48 (2012) 9956—9964.
[16] K. Huang, C.-L. Sun, Z.-J. Shi, Chem. Soc. Rev. 40 (2011) 2435—2452.
[17] M. North, R. Pasquale, C. Young, Green Chem. 12 (2010) 1514—1539.
[18] A. Correa, R. Martin, Angew. Chem. Int. Ed. 48 (2009) 6201—6204.
[19] T. Fan, X. Chen, Z. Lin, Chem. Commun. 48 (2012) 10808—10828.
[20] M. Drees, M. Cokoja, F.E. Kühn, ChemCatChem 4 (2012) 1703—1712.
[21] W.Z. Zhang, W.J. Li, X. Zhang, H. Zhou, X.B. Lu, Org. Lett. 12 (2010) 4748—4751.
[22] R. Yuan, Z. Lin, ACS Catal. 4 (2014) 4466—4473.
[23] S. Grimme, J. Comput. Chem. 27 (2006) 1787—1799.
[24] D. Yu, Y. Zhang, Proc. Nat. Acad. Sci. 107 (2010) 20184—20189.
[25] L. Yang, Y. Yuan, H. Wang, N. Zhang, S. Hing, RSC Adv. 4 (2014) 32457—32466.
[26] H.D. Velázquez, Z.-H. Wu, M. Vandichel, F. Verpoort, Catal. Lett. 147 (2017) 463—471.
[27] S. Grimme, J. Antony, S. Ehrlich, H.J. Krieg, Chem. Phys. 132 (2010) 154104.
[28] S.V.C. Vummaleti, G. Talarico, S.P. Nolan, L. Cavallo, A. Poater, Org. Chem. Front 3 (2016) 19—23.
[29] T. Fujihara, K. Nogi, T. Xu, J. Terao, Y. Tsuji, J. Am. Chem. Soc. 134 (2012) 9106—9109.
[30] F.B. Sayyed, Y. Tsuji, S. Sakaki, Chem. Commun. 49 (2013) 10715—10717.
[31] K. Ukai, M. Aoki, J. Takaya, N. Iwasawa, J. Am. Chem. Soc. 128 (2006) 8706—8707.
[32] H. Qin, J. Han, J. Hao, E.B. Kantchev, Green Chem. 16 (2014) 3224—3229.
[33] H. Mizuno, J. Takaya, N. Iwasawa, J. Am. Chem. Soc. 133 (2011) 1251—1253.
[34] X. Lv, L. Zhang, B. Sun, Z. Li, Y.-B. Wu, G. Lu, Catal. Sci. Technol. 7 (2017) 3539—3545.
[35] T. Ohishi, M. Nishiura, Z. Hou, Angew. Chem. Int. Ed. 47 (2008) 5792—5795.
[36] L. Dang, Z. Lin, T.B. Marder, Organometallics 29 (2010) 917—927.
[37] T.G. Ostapowicz, M. Hölscher, W. Leitner, Chem. Eur J. 17 (2011) 10329—10338.
[38] J. León, A. Correa, R. Martin, J. Am. Chem. Soc. 135 (2013) 1221—1224.
[39] F.B. Sayyed, S. Sakaki, Chem. Commun. 50 (2014) 13026—13029.
[40] T. Fujihara, T. Xu, K. Semba, J. Terao, Y. Tsuji, Angew. Chem. Int. Ed. 50 (2011) 523—527.
[41] J.-F. Wang, J.-F. Jia, C.H. Guo, H.S. Wu, J. Organomet. Chem. (2013) 84—88.
[42] T.M. Fan, F.K. Sheong, Z. Lin, Organometallics 32 (2013) 5224—5230.
[43] T.G. Ostapowicz, M. Hölscher, W. Leitner, Eur. J. Inorg. Chem. (2012) 5632—5641.
[44] C.M. Williams, J.B. Johnson, T. Rovis, J. Am. Chem. Soc. 130 (2008) 14936—14937.
[45] R. Yuan, Z. Lin, Organometallics 33 (2014) 7147—7156.
[46] Q. Wang, C.H. Guo, Y. Ren, H.-S. Wu, J. Mol. Model. 21 (2015) 122.
[47] J. Takaya, N. Iwasawa, J. Am. Chem. Soc. 130 (2008) 15254—15255.
[48] a) M.T. Johnson, R. Johansson, M.V. Kondrashov, G. Steyl, M.S.G. Ahlquist, A. Roodt, O.F. Wendt, Organometallics 29 (2010) 3521—3529; b) J. Wu, J.C. Green, N. Hazari, D.P. Hruszkewycz, C.D. Incarvito, T.J. Schmeier, Organometallics 29 (2010) 6369—6376; c) M. Wang, T. Fan, Z. Lin, Polyhedron 32 (2012) 35—40.
[49] T.W. Butcher, E.J. McClain, T.G. Hamilton, T.M. Perrone, K.M. Kroner,

G.C. Donohoe, N.G. Akhmedov, J.L. Petersen, B.V. Popp, Org. Lett. 18 (2016) 6428—6431.

[50] X. Lv, Y.-B. Wu, G. Lu, Catal. Sci. Technol. 7 (2017) 5049—5054.
[51] G. Herzberg, Electronic Spectra and Electronic Structure of Polyatomic Molecules, Van Nostrand, New York, 1966.
[52] T.J. Schmeier, N. Hazari, C.D. Incarvito, J.A. Raskatov, Chem. Commun. 47 (2011) 1824—1826.
[53] Lj. Pavlovic, J. Vaitla, A. Bayer, K.H. Hopmann, Rhodium-catalyzed hydro-carboxylation: mechanistic analysis reveals unusual transition state for C-C bond formation (submitted for publication).
[54] C. Cramer, D.G. Truhlar, Phys. Chem. Chem. Phys. 11 (2009) 10757—10816.
[55] K.H. Hopmann, Organometallics 35 (2016) 3795—3807.
[56] G. Morello, K.H. Hopmann, ACS Catal. 7 (2017) 5847—5855.